



A COMPREHENSIVE STUDY OF DILUTE  
MAGNETIC SEMICONDUCTOR RESONANT  
TUNNELING DIODES

Dissertation

zur Erlangung des  
naturwissenschaftlichen Doktorgrades  
der Julius-Maximilians-Universität Würzburg

vorgelegt von  
Michael RÜth  
aus Würzburg / Bayern

Würzburg 2011

Eingereicht am:

bei der Fakultät für Physik und Astronomie

Gutachter der Dissertation:

1. Gutachter: Prof. Dr. Laurens W. Molenkamp
2. Gutachter: Prof. Dr. Matthias Bode
3. Gutachter:

Prüfer im Promotionskolloquium:

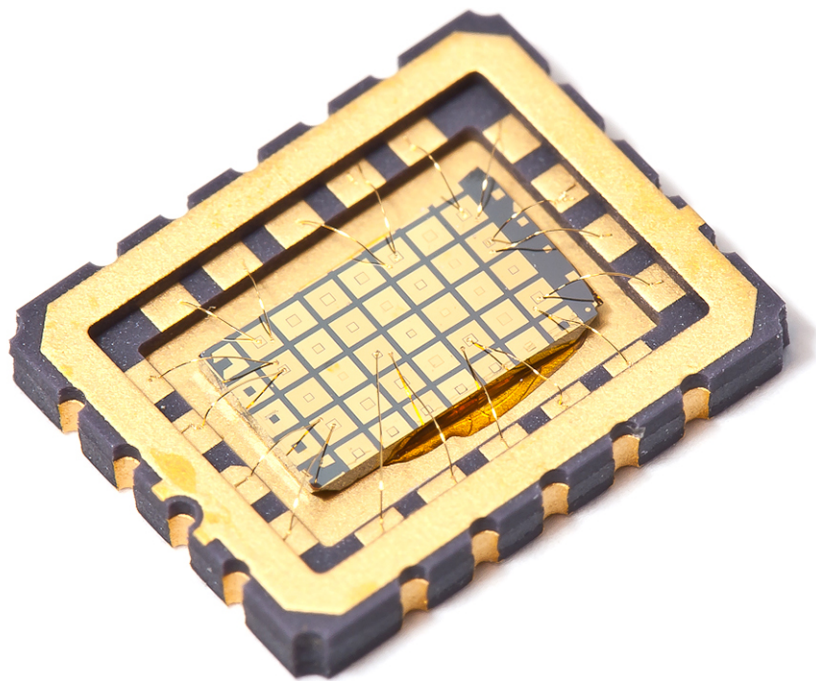
1. Prüfer Prof. Dr. Laurens W. Molenkamp
2. Prüfer: Prof. Dr. Matthias Bode
3. Prüfer:

Tag des Promotionskolloquiums:

Doktorurkunde ausgehändigt am:

*To My Wife*





Resonant tunneling diodes mounted in a standardized chip carrier



# Publications

Parts of this thesis have been published elsewhere. More manuscripts are in preparation

- M. R uth, T. Slobodskyy, C. Gould, G. Schmidt, L.W. Molenkamp, *Fermi edge singularity in II-VI semiconductor resonant tunneling structures*, Applied Physics Letters, **93**, 182104, 2008
- A. Frey, M. R uth, R.G. Dengel, C. Schumacher, C. Gould, G. Schmidt, K. Brunner and L.W. Molenkamp, *Semimagnetic II-VI semiconductor resonant tunneling diodes characterized by high-resolution X-ray diffraction*, Journal of Crystal Growth, **312**, 1036, 2010
- M. R uth, C. Gould and L.W. Molenkamp, *Zero field spin polarization in a two-dimensional paramagnetic resonant tunneling diode*, Phys. Rev. B, **83**, 155408, 2011
- M. R uth, D. Supp, T. Borzenko, T. Slobodskyy, A. Slobodskyy, G. Schmidt, C. Gould and L.W. Molenkamp *A voltage controlled spin valve*, submitted to Physical Review Letters, 2011

## In preparation

- P. Hartmann, M. R uth, S. Bieker, A. Frey, C. Gould, T. Kiesling, K. Brunner, L.W. Molenkamp *Epitaxial liftoff of pre-patterned all II-VI heterostructure transport devices*, in preparation, 2011
- M. R uth, A. Frey, C. Gould and L.W. Molenkamp *Simultaneous strong coupling of a quantum dot to a Fermionic and a Bosonic bath*, in preparation, 2011





# Contents

<b>Zusammenfassung</b>	<b>1</b>
<b>Summary</b>	<b>5</b>
<b>1 Introduction</b>	<b>9</b>
<b>2 Resonant tunneling in all II-VI semiconductor devices</b>	<b>13</b>
2.1 The (Zn,Be,Mn,Cd)Se material system . . . . .	14
2.2 The transfer matrix method . . . . .	16
2.2.1 Implementation of disorder in the idealized coherent picture . . . . .	19
2.2.2 A study of various double barrier systems with TMM . . . . .	20
2.3 Tilted conduction band profiles . . . . .	23
2.4 Implications of contact resistances . . . . .	25
2.5 Comparison to experiment . . . . .	27
2.6 Empirical modeling of resonant tunneling conductance . . . . .	29
2.7 The non-resonant background current . . . . .	34
2.8 The DMS RTD as a voltage controlled spin-filter . . . . .	37
<b>3 Zero field spin polarization in a 2D paramagnetic resonant tunneling diode</b>	<b>41</b>
<b>4 0D interface states in a DMS resonant tunneling diode</b>	<b>53</b>
<b>5 A voltage controlled spin-valve</b>	<b>59</b>
5.1 Measurement and single channel analysis . . . . .	60
5.2 The two channel model . . . . .	64
5.3 Zero magnetic field operation . . . . .	70
<b>6 Fermi-edge singularity in a non-magnetic self-assembled quantum dot resonant tunneling diode</b>	<b>75</b>
6.1 The Fermi-edge Singularity . . . . .	75
6.2 Measurement and analysis . . . . .	77

---

<b>7</b>	<b>Simultaneous strong coupling of a self-assembled quantum dot to a Fermionic and a Bosonic bath</b>	<b>83</b>
7.1	Quantum dot coupled to its Mn doped environment . . . . .	83
7.2	Quantum dot coupled to both baths . . . . .	84
7.3	A comparison of various magnetic dots . . . . .	93
<b>8</b>	<b>Resonant tunneling through a dilute magnetic self-assembled quantum dot near zero bias voltage</b>	<b>95</b>
<b>9</b>	<b>Conclusion and outlook</b>	<b>101</b>
<b>A</b>	<b>Numerical solution of a double RTD circuit</b>	<b>105</b>
A.1	A homotopy Newton method . . . . .	105
A.2	Computing the path along a spin-resonance . . . . .	106
<b>B</b>	<b>Scientific publishing with Mathematica</b>	<b>109</b>
	<b>Bibliography</b>	<b>120</b>

# Zusammenfassung

Diese Doktorarbeit befasst sich mit Transportmessungen an resonanten Tunneldioden (engl. resonant tunneling diode, RTD), welche vollständig aus II-VI Halbleitermaterial bestehen. Das verdünnt magnetische (engl. dilute magnetic semiconductor, DMS) Halbleitermaterialsystem (Zn,Be,Mn,Cd)Se ist sehr vielseitig und eignet sich hervorragend als Testsystem für diverse Spintronik Bauelemente, denn magnetische und elektrische Eigenschaften lassen sich getrennt voneinander einstellen. Im Gegensatz zum ferromagnetischen Halbleiter (Ga,Mn)As verändert das Dotieren von ZnSe mit Mn nicht die elektrischen Eigenschaften des Halbleiters.

Im ersten Teil dieser Arbeit stellen wir ein neues Modell vor, das sowohl die qualitative als auch die quantitative Analyse zweidimensionaler (Zn,Mn)Se Quantentrog RTDs ermöglicht. Eine vollständige theoretische Beschreibung zeigt lediglich ansatzweise Übereinstimmung mit dem Experiment [Havu 05]. Anstatt die Beschreibung der I-V Kennlinie aus grundlegenden quantenmechanischen Prinzipien aufzubauen, verwendet das hier vorgestellte Modell eine empirische Beschreibung der Resonanzen in den I-V Kennlinien der RTDs. Wir zeigen, dass die nicht resonanten Beiträge zum Tunnelstrom maßgeblich von der durch die angelegte Spannung verkippten Doppelbarriere abhängen und dass dies durch eine Transfermatrix modelliert werden kann. Angesichts dieser Erkenntnisse diskutieren wir die Anwendbarkeit idealisierter Modelle für die Beschreibung der Charakteristika von II-VI Halbleiter RTDs und zeigen warum diese nicht in der Lage sind ihre wichtigste Transporteigenschaft, die Resonanz, richtig wiederzugeben.

Wie bereits von Slobodskyy et. al gezeigt wurde, lassen sich diese DMS RTDs als spannungsgesteuerte Spinfilter nutzen. In ihrem intuitiven Modell zur Beschreibung der Spinfilter Eigenschaften ist die gemessene I-V Kennlinie bei  $B=0$  T der Startpunkt für die weitere Modellierung der Magnetfeldabhängigkeit. Dieses Modell zeigt gute Übereinstimmung mit den Messungen bis einschließlich  $B=6$  T. Es wird jedoch weder versucht das Zustandekommen dieser Nullfeld I-V Kennlinie herzuleiten, noch den Wirkungsgrad des untersuchten Spinfilters zu bestimmen. Das hier vorgestellte Modell beinhaltet eine vollständige, konsistente Beschreibung des erweiterten Messbereichs bis  $B=14$  T einschließlich der Nullfeldkennlinie. Des weiteren ermöglicht es uns den Wirkungsgrad des Spinfilters aus den Messdaten zu bestimmen. Zusätzlich werden die Auswirkungen von Emitterzuständen und Probenunregelmäßigkeiten auf die Transporteigenschaften der DMS RTDs aufge-

zeigt. Während es für selbstorganisierte Quantenpunkt RTDs bekannt war, dass sich in der Nähe von lokalisierten Zuständen eine mikroskopische magnetische Ordnung bildet, zeigt unser Modell dass diese so genannten gebundenen magnetischen Polaronen (engl. bound magnetic polaron, BMP) auch für den Transport in DMS Quantentrog RTDs eine Rolle spielen. Trotz des paramagnetischen Quantentrogmaterials zeigen auch die zweidimensionalen RTDs eine remanente Nullfeldaufspaltung, da sich BMP-artige Zustände an der Grenzfläche des Quantentrogs bilden.

Um die Annahme, dass diese Unregelmäßigkeiten an der Quantentrogrenzfläche die Transporteigenschaften der RTDs beeinflussen zu überprüfen, untersuchen wir die Zugverformung der II-VI Heterostrukturen, welche sich durch den Gitterunterschied zum GaAs Substrat während des Wachstums ausbildet. Wir entfernen das GaAs Substrat von einer RTD, welche die zuvor erwähnte Nullfeldaufspaltung der Spin-up und Spin-down Zustände im Quantentrog aufweist. Die Verspannung die sich während des Wachstums aufgebaut hat löst sich durch das Entfernen des Substrates. Durch die resultierende Glättung der Grenzflächen wird die Bindungsenergie der BMP artigen Zustände geschwächt. Vergleicht man nun Fits der I-V Kennlinien vor und nach dem Entfernen des Substrats, zeigen sich geänderte Probeneigenschaften wie man sie innerhalb unseres Modells für glattere Grenzflächen erwarten würde. Während die Finesse der Resonanz sich deutlich verbessert, nimmt die beobachtete Nullfeldaufspaltung ab, sowie die Qualität der Tunnelbarrieren zu.

Nachdem wir ein vollständiges Modell zur Beschreibung der Transporteigenschaften einer II-VI DMS RTD eingeführt haben, ist der folgerichtige Schritt die Vereinigung zweier solcher DMS RTDs in einem Bauteil. Während die erste RTD als Injektor benutzt wird, dient die zweite in Serie geschaltete RTD als Detektor des spinpolarisierten Stroms. Wir untersuchen ein solches Spin-Ventil (engl. spin valve) und zeigen warum es zu keiner Abschneidung des Stroms kommt, selbst wenn die beiden RTDs so eingestellt werden, dass sie nur entgegengesetzte Spins durchlassen. Der Kontakt zwischen den RTDs ist nicht nur notwendig um die einzelnen Bestandteile des Spin-Ventils unabhängig voneinander zu steuern, er schränkt auch gleichzeitig dessen Funktion ein, da er die Region zwischen den RTDs mit einem unpolarisierten Reservoir verbindet. Das zuvor für eine einzelne DMS RTD entwickelte Modell wird für das Spin-Ventil erweitert und zeigt erneut qualitative sowie quantitative Übereinstimmung mit dem Experiment. Wir zeigen, dass die Spininformation während des Transfers vom Injektor zum Detektor größtenteils erhalten bleibt und extrahieren den Wirkungsgrad des Spin-Ventils. Da beide DMS RTDs Nullfeldaufspaltung aufweisen, diskutieren wir anschließend die Verwendung des Spin-Ventils ohne angelegtes externes Magnetfeld.

Messungen an Quantentrog RTDs mit Nullfeldaufspaltung zeigen den simultanen Transport durch das Ensemble der niederdimensionalen Grenzflächenzuständen in der Probe. RTDs mit selbstorganisierten Quantenpunkten erlauben es hingegen den Transport durch einen einzelnen nulldimensionalen Zustand zu beobachten. Die reduzierte Dimensionalität der resonanten Zustände kann des weiteren Vielteilcheneffekte wie die Singularität der Transmissionsrate an der Fermi-Kante (engl. Fermi-edge singularity, FES) zur Folge

haben.

Zunächst betrachten wir eine Quantenpunkt RTD ohne magnetische Dotierung. Durch eine FES entsteht eine Singularität in der I-V Charakteristik sobald der Zustand im Quantenpunkt auf Höhe der Fermienergie im Emitter liegt. Vorhergehende Studien dieses Vielteilcheneffekts in RTDs beschränkten sich auf das III-V Materialsystem und wurden meist bei hohen Magnetfeldstärken durchgeführt. Die hier gezeigten I-V Kennlinien einer II-VI Quantenpunkt RTD zeigen den Effekt bereits deutlich ohne angelegtes Magnetfeld. Weiterhin ist er bei Temperaturen bis 45 K sichtbar und zeigt eine Magnetfeldabhängigkeit die für einen zweidimensionalen Charakter der Injektorzustände spricht.

Ein weiterer Vielteilcheneffekt in solchen nulldimensionalen Systemen kann nach magnetischer Dotierung der Tunnelbarrieren beobachtet werden. Resonantes Tunneln durch einen magnetischen Quantenpunkt ermöglicht es uns, den Transport durch ein einzelnes, gebundenes magnetisches Polaron zu beobachten. Gould et al. zeigten bereits die Spinaufspaltung, die aus der Kopplung des Quantenpunktzustands mit seiner magnetischen Umgebung resultiert [Goul 06]. In dieser Arbeit zeigen wir, dass es möglich ist, den Quantenpunktzustand gleichzeitig an das magnetische (BMP) sowie an das fermionische (FES) Reservoir anzukoppeln. Die durch die FES erhöhten Tunnelraten an der Fermi-Kante ermöglichen es bei  $T=20$  mK eine zusätzliche Feinstruktur der Resonanzen zu beobachten. Diese Feinstruktur entspricht wahrscheinlich dem Anregungsspektrum des Polaronenzustands. Des Weiteren stellen wir ein vorläufiges Modell vor, welches bereits qualitative Übereinstimmung mit der Nullfeld I-V Kennlinie, sowie deren Temperatureverhalten liefert. Auf Grund der Ankopplung des Quantenpunktzustandes an beide Reservoirs, können an solchen Systemen erhobenen Daten zur Überprüfung moderner Bose-Fermi Theorien genutzt werden.

Zur genaueren Untersuchung solcher Vielteilcheneffekte betrachten wir eine weitere RTD die eine Ankopplung an beide Reservoirs vorweist. Diese zweite Probe zeigt sowohl charakteristisches FES Verhalten, als auch die BMP typische Nullfeldaufspaltung, jedoch schon bei sehr kleinen Vorspannungen von 2 mV. Durch die ausgeprägte Asymmetrie der Quantenpunkt RTDs zeigen die meisten untersuchten Proben die Singularitäten in der I-V Kennlinie nur beim Laden des Quantenpunkts durch die dickere der beiden Barrieren. Zudem wird der Einfluß des Fermisees im Kollektor meist vernachlässigt, da bei den Spannungen, bei denen die Resonanzen üblicherweise auftreten, die Fermikante des Kollektors bereits weit unterhalb der Emitterzustände liegt. Dies trifft hier jedoch nicht zu, da die für die Resonanz benötigten Vorspannungen kleiner sind als die Bandbreite der Emitterzustände. Wir vergleichen Transportmessungen für negative und positive Vorspannungen, bei denen die FES Charakteristik jeweils von der dünneren bzw. dickeren Barriere bestimmt wird.

Letztendlich hat die Untersuchung der Auswirkungen von Kontaktwiderständen, Abweichungen vom idealisierten Bild der Probe, sowie der angelegten Spannung zu einem einfachen vereinenden Modell geführt. Dieses beschreibt nicht nur einzelne DMS RTDs, sondern auch komplexere, aus mehreren RTDs zusammengesetzte Bauteile.



# Summary

We investigate transport measurements on all II-VI semiconductor resonant tunneling diodes (RTDs). Being very versatile, the dilute magnetic semiconductor (DMS) system (Zn,Be,Mn,Cd)Se is a perfect testbed for various spintronic device designs, as it allows for separate control of electrical and magnetic properties. In contrast to the ferromagnetic semiconductor (Ga,Mn)As, doping ZnSe with Mn impurities does not alter the electrical properties of the semiconductor, as the magnetic dopant is isoelectric in the ZnSe host.

In the first part of this thesis, a new modeling scheme is presented which allows for qualitative and quantitative analysis of two dimensional (Zn,Mn)Se quantum well RTDs. A full theoretical modeling scheme only shows rough qualitative agreement to the experiment [Havu 05]. Instead of relying on such a bottom-up description of the transport characteristics, the model presented in this thesis is based on an empirical description of the apparent resonances in the I-V characteristics of our RTDs. We show that the non-resonant contributions to the current are dominated by the tilt of the double barrier region due to the applied bias voltage and can be modeled with a transfer matrix method (TMM). In light of these findings, we show to what limited extent the usual idealized pictures are useful tools to describe the nature of the II-VI RTDs, and give explanations to why they fail to reproduce the most important characteristic of such an RTD, its resonance.

As shown by Slobodskyy et al. [Slob 03], these DMS RTDs act as voltage controlled spin filters. In their intuitive model of the spin-filter properties, the zero magnetic field I-V characteristic was used as a starting point for the fits to the magnetic field measurements. While this model shows good agreement to the experiment for magnetic fields up to 6 T, no effort was made to discuss the fundamental transport properties at zero magnetic field or to extract the spin-filter efficiencies of the device. The detailed model presented in this thesis provides this description of the zero magnetic field I-V characteristic, shows good agreement to the experimental data in an extended magnetic field range up to 14 T and also allows for the extraction of the current spin polarization of the device. Additionally, the implications of emitter effects and device imperfections on the transport properties are shown. While it was known for self-assembled quantum dot states that localized impurity states form a microscopic order in their vicinity [Goul 06], the modeling revealed that these so called bound magnetic polarons (BMPs) also play a role in the transport characteristics

of DMS quantum well RTDs. Counterintuitively, a remanent zero field splitting is also observed for two dimensional RTDs, as BMP states form at the interface of the (Zn,Mn)Se quantum well.

To further test the assumption that imperfections at the quantum well interface significantly alter the transport properties of an RTD, we investigate the tensile strain that builds up in our II-VI heterostructures due to the lattice mismatch to the GaAs substrate. We remove the GaAs substrate from an RTD which shows the aforementioned splitting of the spin-up and down channels without an applied external magnetic field. The tensile strain built up during growth relaxes as the substrate is removed and the interface is flattened, weakening the BMP states. By comparing fits to the I-V characteristics of the device before and after removing the substrate, the device properties are altered according to what is expected within our model for a smoother interface. The sharpening of the resonance, the reduction of the zero field splitting as well as an increase in tunnel barrier quality are clearly observed.

Equipped with a complete picture of the transport physics of a II-VI DMS RTD, the next logical step is to combine two such spin sensitive RTDs in an injector-detector scheme. We investigate such a spin-valve device and discuss why no clear off-state is observed when the two RTDs are set to transmit opposite spin species. While the middle contact between the two RTDs is necessary to independently operate the building blocks of the spin-valve, it also hinders spin-valve operation as it connects the region between the two RTDs to an unpolarized reservoir. The model developed for the single DMS RTDs is extended for the compound device and is again in full qualitative and quantitative agreement with the experiment. We show that spin is mostly conserved as it is transferred from the injector to the detector and extract the spin valve efficiencies. As each of the DMS RTDs exhibit remanent zero field splitting, the possibility of using the spin-valve at  $B=0$  T is subsequently assessed.

Measurements on RTDs showing remanent zero field splitting reflect simultaneous transport through the ensemble of low dimensional interface states in the device. RTDs employing self assembled CdSe quantum dots as resonant tunneling states however allow for the observation of resonant transport through a single zero dimensional state. The reduced dimensionality of the resonant tunneling state also gives rise to many particle effects such as the Fermi-edge singularity (FES).

First we investigate an RTD containing self-assembled CdSe quantum dots without magnetic doping. A singularity in the I-V characteristic arises due to a FES when the quantum dot state is aligned with the emitter Fermi energy. Previous experimental studies of FES have been limited to III-V devices, often at high magnetic fields. The feature we report here is already clearly observed in the absence of external magnetic field for temperatures up to 45 K, and shows magnetic field dependence reflective of two dimensional character in the injector.

A second many particle effect is observed in these zero dimensional RTDs as we add magnetic dopants to the tunnel barriers. Resonant tunneling transport through a single



self-assembled quantum dot embedded in a magnetic environment enables us to observe the transport through a single bound magnetic polaron. Gould et al. previously observed the spin splitting of a single quantum dot state due to the coupling to its magnetic vicinity [Goul 06]. Here we show that it is possible to achieve the simultaneous coupling of the quantum dot state to its Mn doped vicinity and the emitter Fermi sea. Due to the FES enhancement of the tunneling rate, we observe an additional fine structure of the resonance peaks at  $T=20$  mK, which probably stems from the excitation spectrum of the BMP state. Furthermore we present a preliminary model that is able to qualitatively reproduce the I-V characteristics at zero magnetic field as well as the temperature dependence thereof. As the localized state is clearly coupled to both baths, transport measurements on such systems provide data against which modern theories of Bose-Fermi systems can be tested.

To further investigate the many body correlation effects in these systems, we study a second RTD that shows a Bose-Fermi coupling. While we again observe both BMP and FES like behavior, in this device the zero field split resonance is observed at bias voltages as low as 2 mV. Due to a pronounced asymmetry, most quantum dot RTDs showing FES enhancement of the tunneling rate only exhibit the enhancement while tunneling into the quantum dot through the thicker of the two barriers. Furthermore the influence of the collector Fermi sea is usually neglected, as it is already lowered far below the emitter states at the bias voltage where the resonances occur. Here we demonstrate that this assumption breaks down for resonant tunneling at bias voltages smaller than the bandwidth of the emitter. We compare transport measurements through the same dot for negative and positive bias voltages, where the FES enhancement is governed by the thinner and thicker tunnel barrier, respectively.

Ultimately, an impact study on contact resistances, device imperfections as well as the applied bias voltage, has led us to a simple unifying model, descriptive of both single DMS RTDs and more complex compound devices.



# Chapter 1

## Introduction

The hope for a new information processing scheme has pushed scientists in the field of spintronics (neologism for spin based electronics) over the past decades to advance their understanding of spin related phenomena in the solid state. Information processing has become a constituent of our workaday life, and still mainly relies on electrical charge to write, store and read information at high processing speeds. Spin as a quantum mechanical property is also a promising candidate to encode information. A prominent example thereof is giant magnetoresistance, the fundamental building block for today's cheap non-volatile storage of data in hard drives.

It is thus fundamentally important to research methods to reliably create, store and read spin in order to establish a spin-based semiconductor technology scheme. Early experiments on direct spin injection from ferromagnetic metals into semiconductors have at best yielded inconclusive signs of very low efficiencies. Schmidt et al. revealed the fundamental obstacle for this method of spin injection, namely the conductance mismatch between the metal and the semiconductor [Schm 00].

This mismatch can be overcome by either using a dilute magnetic semiconductor (DMS) as a spin-injector [Fied 99] or by separating the magnetic metal injection layer by a tunnel barrier from the semiconductor [Rash 00, Jans 07, Pate 09]. Both of these options however mainly inject majority spins and a magnetic field is needed to switch the injector magnetization. Rather than switching the contact, Slobodskyy et al. use a DMS resonant tunneling diode (RTD) as voltage-controlled spin-filter [Slob 03]. At different bias voltages this device is able to selectively transport either of the two spin species from the emitter to the collector, without the need for a pre-polarized injector layer.

As the DMS (Zn,Mn)Se is paramagnetic, an external magnetic field is necessary to lift the degeneracy of the spin-up and spin-down states. A localized level is however able to stabilize a microscopic magnetic order in its vicinity by forming a bound magnetic polaron (BMP) [Diet 82]. Gould et al. show that such an ordering mechanism can also lift the degeneracy of the resonant tunneling state in a DMS RTD [Goul 06]. Using CdSe quantum dots embedded in DMS (Zn,Be,Mn)Se tunnel barriers instead of a (Zn,Mn)Se quantum well enables the DMS RTD to act as a voltage controlled spin-filter without the

need for an external magnetic field.

In addition to inducing a magnetic order, zero dimensional RTDs have also proven a useful testbed for many body correlation effects. Matveev and Larkin predicted that an effect similar to the Fermi edge singularity (FES) seen in the X-ray absorption spectrum of metals [Ohta 90] can also be seen while tunneling into zero dimensional (0D) states [Matv 92]. This is confirmed by Geim et al. for a quantum well (Al,Ga)As-GaAs RTD, where resonant tunneling through a localized impurity shows such a characteristic enhancement of the tunneling rate when the impurity is aligned with the emitter Fermi energy by an applied bias voltage [Geim 94]. Subsequent observations of the FES in RTDs have been limited to III-V devices and often required high magnetic fields to be observed, as the FES is most prominent for 2D-0D tunneling and the quantization by the magnetic field reduces the dimensionality of the emitter states.

In this thesis we present a comprehensive study of resonant tunneling in 0D and two dimensional (2D) II-VI semiconductor heterostructures. The thesis is organized as follows. Chapter 2 gives a brief introduction to the ZnSe material system and discusses why it was chosen for this study. A new empirical modeling scheme is presented, which is used for the analysis of all II-VI DMS quantum well RTDs. The model is also used to briefly review the application of a DMS RTD as a voltage controlled spin filter. In chapter 3 we show evidence for remanent zero field splitting in these devices, despite the paramagnetic nature of the (Zn,Mn)Se quantum well material. As our detailed model shows, a high spin polarization is achieved without the need for an external magnetic field. To further investigate this magnetic ordering at the interface, in chapter 4 we remove the substrate on such a device to release the tensile strain in the heterostructure, smoothing the layers of the device.

A logical extension of the voltage controlled spin-filter is to couple two spin selective RTDs into a spin injector and detector pair. In chapter 5, we show how such a structure can be operated as a voltage controlled spin valve. An extended model based on the findings of chapters 2 and 3 is used to extract the spin-valve efficiencies.

In chapter 6 we investigate many body correlation effects on the resonant tunneling transport through a single self-assembled CdSe quantum dot (SAD). We demonstrate an FES in an all II-VI semiconductor RTD containing self-assembled CdSe quantum dots, where the enhancement to the tunneling rate is already observed at zero magnetic field. Additional enhancement is observed at low temperatures which is suggestive of backscattering associated with local effects near the dot and cannot be explained within conventional FES theory. While the many particle modifications to the resonant tunneling characteristics through a single CdSe quantum dot from the electron gas (FES) and its magnetic vicinity (BMP) have previously been observed independently, we demonstrate an optimized DMS SAD RTD in chapter 7, where both effects can be observed simultaneously. Systems coupled to two baths are promising prospects for the observation of quantum critical points [Kirc 09]. Chapter 8 presents findings on a similar device with an apparent

---

resonance at very low bias voltages in the order of the emitter bandwidth. The impact of the coupling of the quantum dot state to the emitter electrons can be assessed, as we see resonant tunneling through the same localized level from two different Fermi seas for positive and negative bias voltages, thus inverting the symmetry of the problem.



## Chapter 2

# Resonant tunneling in all II-VI semiconductor devices

After the development of molecular beam epitaxy (MBE) in the 60's, by means of heteroepitaxy it was henceforth possible to design man-made crystals of specific vertical conduction/valence band profiles. As the crystal quality grew with further development, resonant tunneling was observed in GaAs-Ga<sub>1-x</sub>Al<sub>x</sub>As heterostructures in the pioneering work of Esaki, Chang and Tsu [Chan 74]. In analogy to the Fabry-Pérot étalon, where the system parameters can be chosen such that light of a certain wavelength is transmitted resonantly, a double barrier semiconductor heterostructure of a certain barrier height, barrier thickness and quantum well width is used to achieve resonant transmission of incident electrons. The most important criterion for the realization of the latter is the quality of the epitaxial growth of the heterostructure. As the quality of resonant tunneling diodes (RTD) drastically improved over the last decades, fabrication of such devices was extended from the well controlled GaAs-Ga<sub>1-x</sub>Al<sub>x</sub>As system to material systems such as ZnSe-Zn<sub>1-x</sub>Be<sub>x</sub>Se, which is utilized for all devices discussed in this thesis.

In this chapter, the theoretical framework used for the modeling of II-VI quantum well RTDs is established. After a brief introduction to the theoretical description of resonant tunneling via a transfer matrix method (TMM), several sets of device parameters and their implications for the device characteristics are discussed within this rudimentary model. Then it is shown how the bias voltage applied across the double barrier heterostructure is influencing the transmittance of the structure and that it has to be considered in the device designing process. Finally, the application of these concepts for an empirical transport model are discussed. Instead of employing idealized and yet complex theoretical calculations, this model is based on empirical observations and a thorough discussion of the device circuitry including all leads and contacts, which play an important role in both experimental and theoretical data.

## 2.1 The (Zn,Be,Mn,Cd)Se material system

The face centered cubic ZnSe crystal is the starting point for all our devices. All devices discussed in this thesis are MBE grown samples on GaAs substrates by T. Slobodskyy and A. Frey, and were patterned with standard lithography techniques. For recipes thereof and a more detailed description of the sample processing procedures, the reader is referred to reference [Ruth 08a].

An important first step for every transport experiment is the realization of a proper contacting scheme. The impact of contacts can be severe and their presence is too often neglected both in device design and data analysis. For the II-VI material system contacts are either evaporated metal Ti/Au pads [Rich 03, Lehm 05] or Indium droplets, interdiffused into the semiconductor surface [Wang 92]. Contacts should be of ohmic character, as while their presence is not to be neglected, their description within the equivalent circuit of a device is by far less challenging if they exhibit a constant resistance. Since metals form Schottky barriers at n-ZnSe interfaces [Tyag 75], the ohmic character in this contacting scheme is achieved by a very thin interface tunnel barrier, which in general is a result of high (up to  $10^{19} \text{ cm}^{-3}$  in Iodine doped ZnSe) carrier concentrations [Sze 81].

The next step towards a vertical RTD are the tunnel barriers which form due to the incorporation of Be atoms in the ZnSe host. Intermixing with Be increases the bandgap  $E_g$  at the  $\Gamma$  point and is described by [Asta 02]

$$E_g(\text{Zn}_{1-x}\text{Be}_x\text{Se}) = E_g(\text{ZnSe}) + 1.77x + 1.1x^2 \quad (2.1)$$

Reference [Chau 00] gives a similar result of  $E_g(\text{Zn}_{1-x}\text{Be}_x\text{Se}) = 2.80 + 1.83x + 0.97x^2$  for low temperatures. For the ternary (Zn,Be)Se the larger part of the increase in  $E_g$  due to the incorporation of Be results in a conduction band offset [Kim 00] with respect to the ZnSe crystal. This conduction band offset is the equivalent of the barrier height for tunneling electrons in II-VI semiconductor RTDs.

Once we have two tunnel barriers with a quantum well spacer layer (usually between 5 to 10 nm), quantized states form in the well between those barriers due to the quantum confinement in growth direction. For a spin selective RTD we also need to adjust the magnetic properties of the heterostructure. The intrinsic g factor of ZnSe conduction band electrons is only 1.1 [Land 99] which is mainly due to the wide band gap of the material. Doping the crystal with Manganese impurities will however result in an interaction of the s-type conduction band electrons with the 5/2 spin of the Mn d-shell. The strength of this magnetic interaction exceeds by far the intrinsic Zeeman splitting of undoped ZnSe.

A description of the magnetic properties of the dilute magnetic semiconductor (DMS) (Zn,Mn)Se is given by the well established modified Brillouin function [Gaj 79]. The concentration  $x_{Mn}$  of the Mn impurities is well below the percolation limit, and to a first order approximation a Mn state will not directly couple to another Mn state in its vicinity. As the direct Mn-Mn interaction is antiferromagnetic, a small fraction of the



Mn impurities form clusters with zero net magnetic moment. Those clusters essentially do not participate in the macroscopic magnetic order and effectively reduce the density of active Mn impurities [Shap 84]. This fact is treated within the Brillouin picture by an effective spin  $s_{eff} < 5/2$ . Introducing a second empirical parameter, the effective Temperature  $T_{eff}$ , which adds to the temperature of the electron system, the modified Brillouin function can be utilized to describe the magnetization of bulk (Zn,Mn)Se. Both  $T_{eff}$  and  $s_{eff}$  depend on the amount of Mn in the crystal, and have to be determined experimentally [Gaj 79, Twar 84]. The splitting  $\Delta E$  of the spin levels due to the s-d interaction reads

$$\Delta E = N_0 \alpha x_{Mn} s_{eff} B_{5/2} \left( \frac{5/2 g \mu_B B}{k_B (T + T_{eff})} \right) \quad (2.2)$$

where  $N_0 \alpha$  is the s-d exchange integral,  $g$  is the electron g-factor and  $\mu_B$  the Bohr magneton.

As long as the interaction between one Mn 5/2 spin and the external field is weaker than the binding energy of an antiferromagnetic cluster, the cluster does not contribute to the macroscopic magnetization. If the strength of the magnetic field however exceeds this binding energy, all Mn spins of the cluster start to align with the external magnetic field and suddenly contribute to the macroscopic magnetization of the material. This breakup of antiferromagnetic pairs is evidenced by steps in measurements that reflect the macroscopic magnetization within the crystal [Shap 84].

For further fine-tuning of the conduction band profile, Cd incorporation is used to reduce the bandgap of the ZnSe crystal. Lowering the conduction band edge in the quantum well material increases the confinement of the quantized states as the tunnel barriers are effectively increased and reduces their energetic offset with respect to the emitter states. As a result, a lower bias voltage is needed to align the quantum well states with the emitter to achieve resonant transmission through the double barrier heterostructure.

Furthermore, Cd can be used for the growth of self-assembled quantum dots incorporated in the all II-VI RTDs. Substituting the quantum well with self assembled quantum dots results in a tunneling state of reduced dimensionality which, as is shown in the chapters 6,7 and 8 of this thesis, enriches the resonant tunneling process with many body correlation effects. The lattice mismatch between CdSe and the tunnel barrier material results in the strain induced self-assembly of the quantum dots. Their shape, composition and thus the electronic properties vastly depend on the growth procedure and a comparative study thereof can be found in [Maha 06, Maha 07]. Changing the Be concentration as well as adding Mn to the tunnel barriers influences the properties of the self-assembled quantum dots [Mock 01, Tito 02, Zhou 05, Lee 07] and have to be considered for the device design.

While the GaAs/(Al,Ga)As system offers a great deal of growth control due to the extensive growth development on this material system (e.g. for high mobility 2DEG

systems), it has one major caveat for magnetic RTDs. Tuning the magnetic properties by incorporation of Mn atoms results at the same time in p-doping of the material, as Mn acts as an acceptor in the GaAs crystal. The charge profile of an RTD is however a delicate aspect of RTD device design. In our II-VI RTDs, the active region of the RTD is not doped with charge carriers for two reasons. Charging the active region would lower the conduction band profile of the quantum well with respect to the Fermi level, which is pinned by the metallic contacts. The bandwidth of the emitter states thus increases massively, which additionally broadens the resonance in the I-V characteristic. Furthermore, some of the quantum well states might be lowered below the Fermi energy at zero bias voltage, making it impossible to tune them in and out of resonance with the applied bias voltage.

The presence of a large number of charges/impurities will furthermore reduce the coherence time for a tunneling electron due to increased probability of scattering events. It is shown in this chapter how a loss of coherence will result in the breakdown of the resonant tunneling process. Our devices are n-doped with iodine in a specific way to achieve an optimum conduction band profile resulting in a narrow emitter bandwidth and reduced impurity scattering in the active region. A big advantage of the (Zn,Mn)Se material system is that adding Mn to the quantum well or the tunnel barriers does *not* result in electrical doping of the crystal. We are therefore able to optimize both magnetic and electrical properties *separately*. On the downside, one loses the carrier mediated, macroscopic ferromagnetic order present in (Ga,Mn)As.

The (Zn,Be,Mn,Cd)Se material system is thus a perfect testbed for the research of spin related phenomena in resonant tunneling transport as well as RTDs of low dimensionality. A theoretical description of these devices helps not only to unravel the apparent new physics in such devices, but also provides a tool to speed up the development of possible spintronic applications based on this material system. In the following a new empirical modeling scheme is presented, that enabled us to shed some light on the physics of the all II-VI resonant tunneling diodes.

## 2.2 The transfer matrix method

For a resonant tunneling heterostructure the potential landscape is in general assumed to be invariant under lateral translation. Separating the total electron energy into the energy  $E_z$  with respect to the growth direction  $z$  and the lateral component  $E_{\parallel} = E_x + E_y$ , it is sufficient for the description of the transmittance of the double barrier structure to look at the one dimensional problem in  $z$  direction as it is schematically shown in fig. 2.1a. The resulting picture of two rectangular barriers under flat band conditions however implies further simplifications, e.g. omission of contacts, scattering, band bending effects or tilted potentials due to an applied bias voltage. Nevertheless, this poor mans approach to resonant tunneling can be used as a tool to make first estimates for the quantization

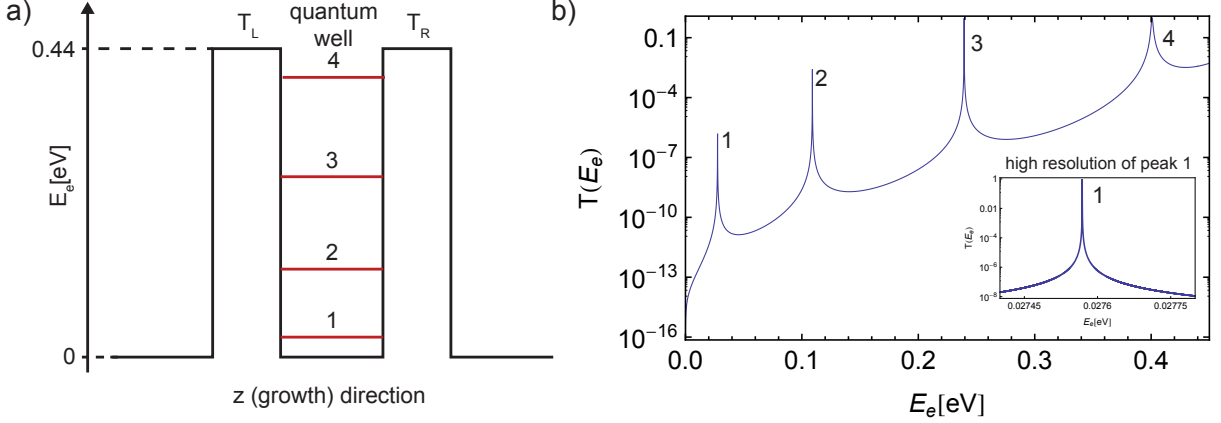


**Figure 2.1:** a) 1D Schematic of the conduction band profile under flat band conditions. Two tunnel barriers form a quantum well with confined states in  $z$  direction. These states result in peaks in the transmission probability as a function of the incident electron energy. b) Transmission probability for an RTD with (Zn,Be)Se tunnel barriers of 5 nm thickness, an 8 nm ZnSe quantum well and a barrier height of 440 meV, as approximated for a Be content of 30%

energies in the quantum well for a specific set of device parameters such as quantum well and tunnel barrier thickness.

As will be shown in this chapter the eigenenergies  $E_n$  of an infinite quantum well as given by

$$E_n = \frac{n^2 \hbar^2}{8m_0 m_{eff} d_{qw}^2} \quad (2.3)$$

are only to be used as rough estimates for the devices under consideration. The perfect confinement of such a particle in a box model is used in section 2.2.2 to validate the results of the transfer matrix (TM) modeling in the limit of very high barriers.

Fig. 2.1a shows a quantum well with four quantized states which form in  $z$  direction between the two barriers, if the coherence time in the respective states is sufficient. In plane electrons are treated as plane waves and do not influence the transmittance  $T(E_z = E_z)$  of the double barrier structure, but still can play an important role for the resulting I-V characteristic as will be shown in section 2.6.

The transfer matrix method assumes that within the WKB-approximation (see e.g. [Schw 02]), the wavelength of the electron is small compared to the characteristic length scale on which the potential is significantly altered. In this case a constant wave number  $k_i$  can be assigned to this area of quasi-constant potential  $V_i$ . An arbitrary potential of length  $l$  can now be divided into steps  $dl$ , while fulfilling this condition. For each  $dl$  the stationary solution for the Schrödinger equation in general reads

$$\Psi_i(x) = Ae^{Ik_i x} + Be^{-Ik_i x} \quad (2.4)$$

where A and B are the amplitudes for the left and right moving part of the wave, respectively. At each interface  $\Psi(x_i)$  and  $1/m_i \Psi'(x_i)$  have to be continuous [Schw 02, p. 58].

Given an initial condition, solutions can be found for the amplitudes A (amplitude of incoming wave) and B (amplitude of reflected wave at interface) for all boundary conditions. As shown in [Mizu 95], the transfer matrix  $T_i$  can be defined for each interface  $i \rightarrow i + 1$

$$\text{TM}_i = \begin{pmatrix} a_i^+ P_i & a_i^- / Q_i \\ a_i^- Q_i & a_i^+ / P_i \end{pmatrix} \quad (2.5)$$

with the electron wavenumber

$$k_i(E_e) = \sqrt{2m_0 m_i (E_e - V_i) e / \hbar} \quad (2.6)$$

and the substitutions

$$\begin{aligned} a_i^+ &= \frac{k_{i+1} m_i + k_i m_{i+1}}{2k_{i+1} m_i} \\ a_i^- &= \frac{k_{i+1} m_i - k_i m_{i+1}}{2k_{i+1} m_i} \\ P_i &= \exp [I(k_i - k_{i+1}) z_i] \\ Q_i &= \exp [I(k_i + k_{i+1}) z_i] \end{aligned} \quad (2.7)$$

where  $m_i$  is the effective masse in the region of quasi-constant potential  $V_i$  and  $z_i$  is the position in z direction.

The total transfer matrix is then given by  $\text{TM}_{tot} = \text{TM}_1 \cdot \dots \cdot \text{TM}_i \cdot \dots \cdot \text{TM}_{N-1}$  for a potential landscape divided into N parts. For equivalent effective masses in the emitter and collector layers ( $m_1 = m_N$ ), the probability T for an electron of energy  $E_e$  is then evaluated from the (11)-element of the matrix  $\text{TM}_{tot}$ .

$$T(E_e) = \frac{k_N}{k_1} * 1 / |\text{TM}_{tot}^{11}|^2 \quad (2.8)$$

For the simplistic case of fig. 2.1a, the problem reduces to 5 areas of constant potential. Figure 2.1b shows the transmittance  $T(E_e)$  for tunnel barriers of 5 nm thickness, 0.44 eV height and a quantum well of 8 nm thickness, assuming a constant effective mass of  $0.15 m_0$  for all layers [Land 99]. For finite barrier height and barrier thickness the symmetric case ( $T_L = T_R$ ) will always lead to a transmission of unity (peaks in fig. 2.1b) when the energy of the incident electron is aligned with a quantum well state (red lines in fig. 2.1a) of the double barrier structure. This idealized one dimensional fully coherent system produces very narrow line-widths especially for strongly confined quantum well states.

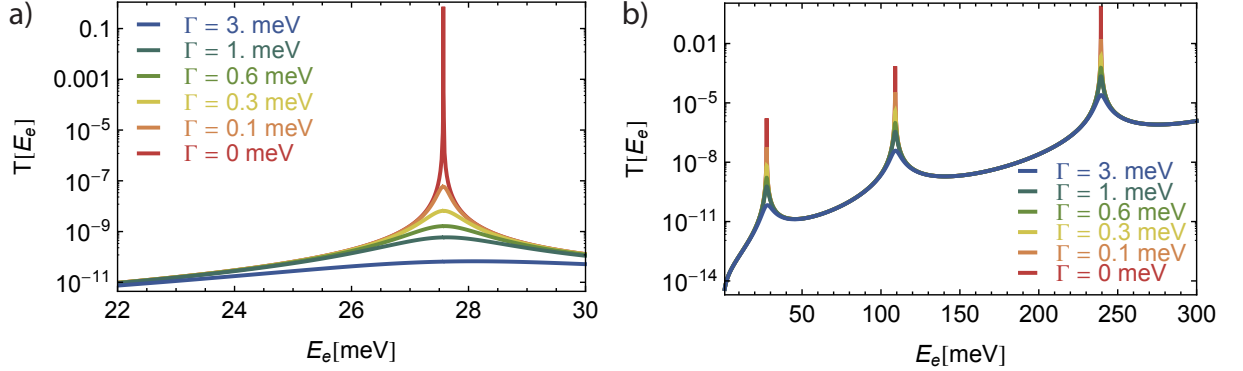


**Figure 2.2:** Transmission probability for a 8 nm ZnSe quantum well with a barrier thickness of 5 nm and a barrier height of 440 meV. As the imaginary potential  $\Gamma$  is increased, the resonant feature broadens and the probability for the electron to tunnel resonantly is reduced. a) Detail of the first resonant feature. b) Overview of the first three resonances. The impact on the resonances are severe, while changes to the non-resonant parts of the spectrum due to the imaginary potential are minor.

### 2.2.1 Implementation of disorder in the idealized coherent picture

However, perfect resonances as discussed above will never be accomplished in any device, even though molecular beam epitaxy (MBE) nowadays provides the means to grow very high quality layer stacks for example in the AlAs/GaAs material system. Not only is the assumption of fully coherent transport with a transmission of unity and the underlying narrow line width unrealistic for a ZnSe heterostructure, it also may result in numerical errors while integrating the transmission probability as a function of the electron energy if the numerical summation is too coarse. In fig. 2.1b a resolution of  $10^4$  data points only fully resolves the fourth resonance. Since the lower resonances (1-3) are sharpening due to the increase in confinement, the resolution was increased by a factor of 4400 in order to fully resolve the unitary transmission of the first resonance (see inset of fig. 2.1b).

An easy way to implement disorder in these type of calculations is to add a small imaginary potential for the quantum well layer which hosts the quantized states. An imaginary potential will damp part of the wave function, which results in a loss of probability and the breakdown of unitarity on resonance [Ston 85]. One can think of this imaginary potential as a scattering mechanism, removing (on average) electrons from the coherent picture by phase breaking events.

The imaginary potential slightly shifts the energetic position of the resonance and broadens the peak as well as reduces its absolute amplitude. Figure 2.2 shows the transmittance of a double barrier system with 5 nm barrier thickness, an 8 nm quantum well layer and 440 meV barrier height at its first resonance for various imaginary potentials  $\Gamma$ . In the following a small imaginary potential will be used in all transfer matrix analysis, not only to gain more realistic transmission curves, but also to prevent numerical errors

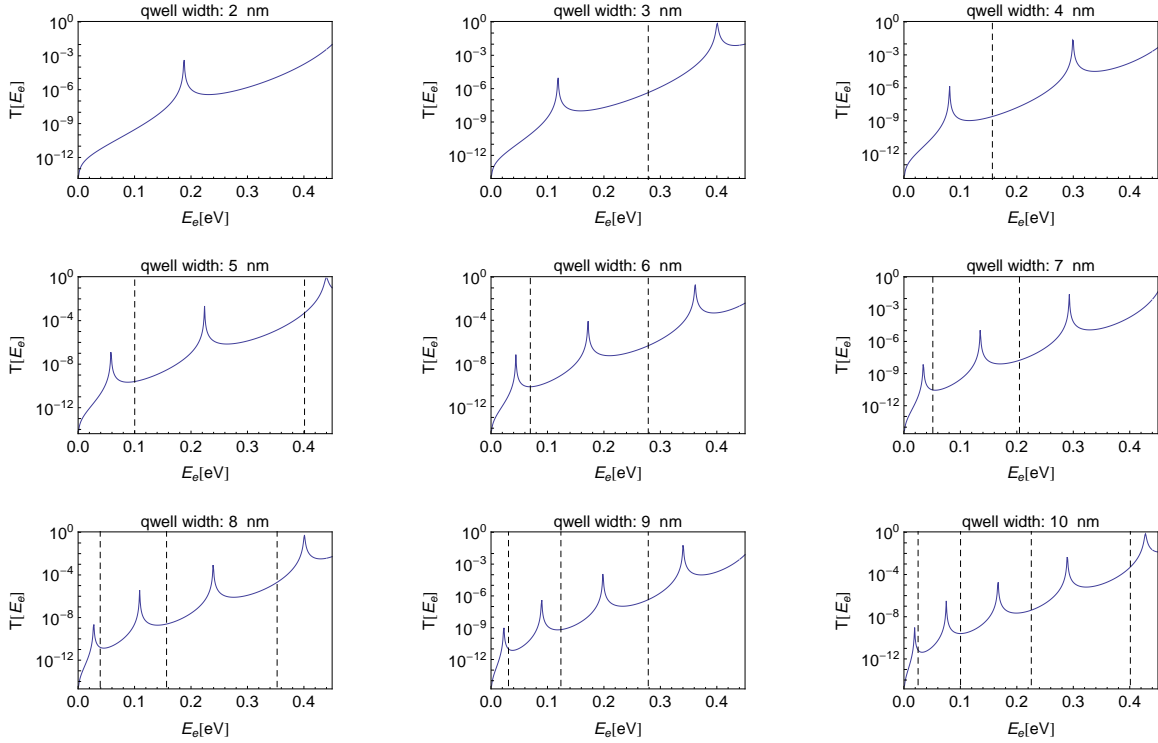


**Figure 2.3:** Transmission probability for various quantum well thicknesses (blue lines) and tunnel barriers of 5 nm thickness and 440 meV height. The dashed lines represent the energetic positions as given by an infinite quantum well model (eq. (2.3)).

in the calculations.

### 2.2.2 A study of various double barrier systems with TMM

Semiconductor devices are usually designed to meet certain criteria of the planned experiment. In order to get a trend on how the eigenstates of the quantum well and thus the I-V characteristics of the device are altered while changing certain sample parameters, one can look at the transmission probabilities of the double barrier region in the simple picture of a flat band with two tunneling barriers in series. The parameters of relevance are quantum well thickness, barrier thickness and barrier height. A typical DMS quantum well RTD is comprised of a 8 nm ( $\text{Zn}_{0.92}\text{Mn}_{0.08}\text{Se}$ ) quantum well and two ( $\text{Zn}_{0.7}\text{Be}_{0.3}\text{Se}$ ) tunnel barriers of 5 nm thickness, which results in a barrier height of approximately 440 meV.

Figure 2.3 shows the transmission probability as a function of the kinetic energy of the tunneling electron for various quantum well widths  $d_{qw}$  from 2 nm to 10 nm for a ( $\text{Zn,Be}$ )Se double barrier system of 5 nm barrier thickness, 440 meV barrier height and an additional imaginary quantum well potential of  $\Gamma = 0.3$  meV. Strong confinement for a quantum well layer of  $d_{qw}=2$  nm thickness only allows for one bound state in the quantum well. Each transmission peak in the plots of fig. 2.3 is descriptive of an eigenstate of the

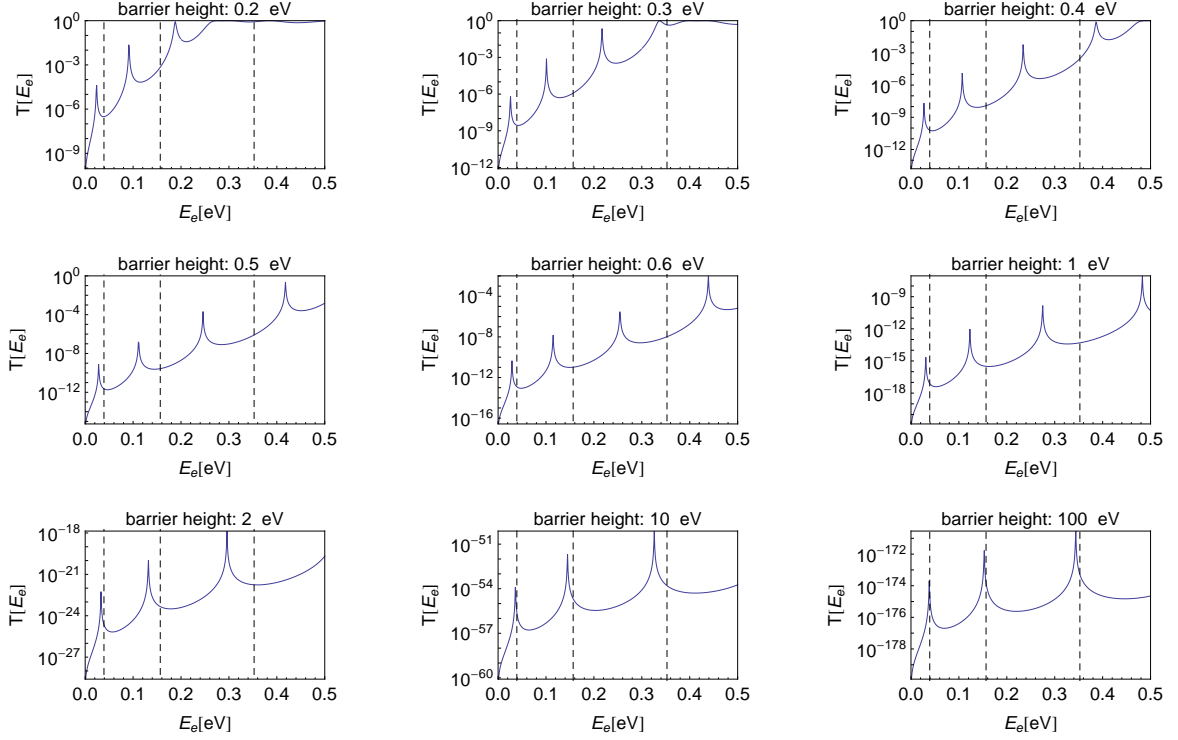


**Figure 2.4:** Transmission probability for various barrier heights (blue lines), tunnel barriers of 5 nm thickness and a quantum well layer thickness of 8 nm. The dashed lines represent the energetic positions as given by an infinite quantum well model (eq. (2.3)).

quantum well and will potentially result in a resonance in the I-V characteristic of such an RTD.

Comparison of the results from 2 nm to 10 nm in fig. 2.3 shows that increasing the thickness of the quantum well layer results not only in the lowering of the eigenstate energy of the confined states, but also in sharpening of the respective transmission peaks as well as a reduction of the energetic distance between the levels. As evidenced by the dashed lines, which show the energetic positions of the confined states as given by an infinite quantum well model in equation (2.3), the exact TMM calculations deviate from the energetic positions predicted by the harsh assumption of an infinite quantum well. Increasing the quantum well width lowers the quantum well states, strengthening the confinement (while still assuming the same level of coherence). The discrepancy between the TMM model and the infinite quantum well model is thus reduced for wider quantum wells, especially for the lowest eigenstate.

Instead of increasing the quantum well width one can also increase the barrier height to allow for more confined states in the quantum well. An increase in barrier height will also increase the confinement of the bound states, since the leaking of the wave function into the barriers is reduced. Figure 2.4 shows calculations for various barrier heights from 200 meV to up to 100 eV for a barrier thickness of 5nm, a quantum well width of 8

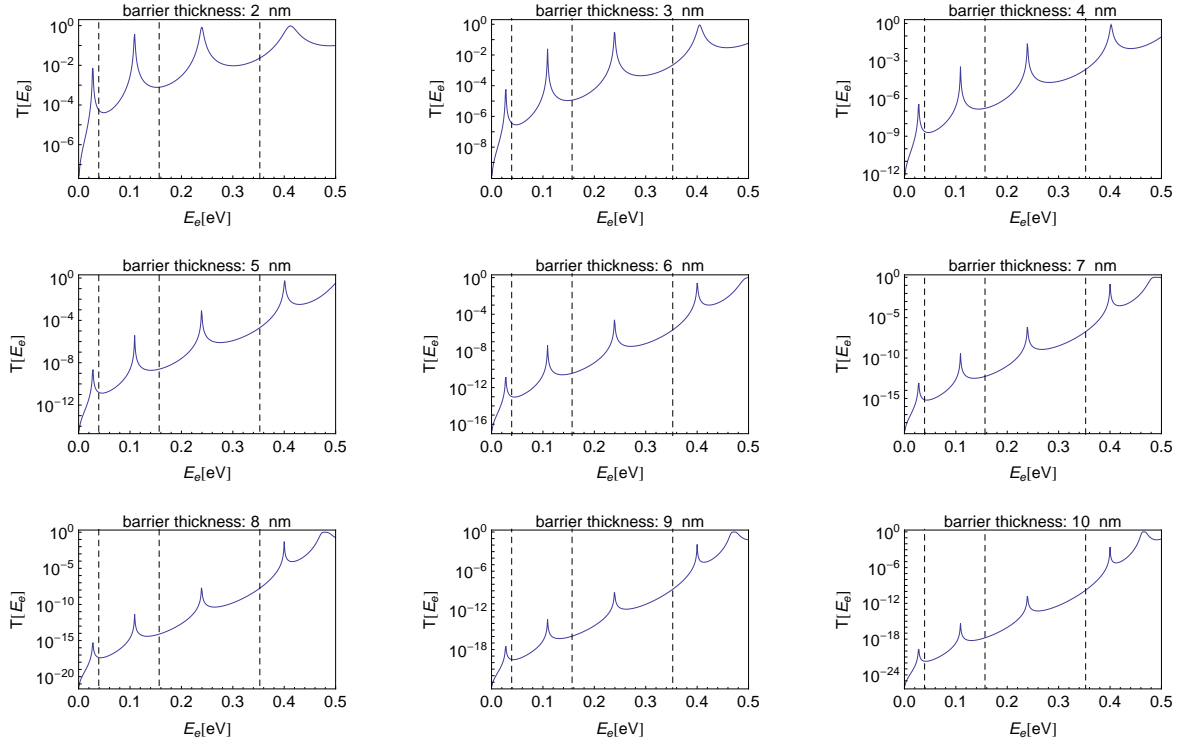


**Figure 2.5:** Transmission probability for various barrier thicknesses (blue lines), a barrier height of 440 meV and a quantum well layer thickness of 8 nm. The dashed lines represent the energetic positions as given by an infinite quantum well model (eq. (2.3)).

nm and an additional imaginary quantum well potential of  $\Gamma = 0.3$  meV. As the barrier height is increased and more and more confined states manifest in the quantum well, the transmission peaks sharpen and their amplitudes are reduced (since the scattering potential is kept constant). While the last four plots of fig. 2.4 (1,2,10 and 100 eV barrier height) are not realistic (Zn,Be)Se barrier heights (the Be content is limited due to the BeSe lattice mismatch to ZnSe), they are plotted to clarify the impact of the barrier height and test the TM model in the limit of the infinite quantum well. The peaks slightly change their eigenstate energy with barrier height due to the increase in confinement. As is shown in the last picture of fig. 2.4, in the limit of very large barriers, the energetic positions of the quantum well eigenstates calculated by a TMM are nearly identical to the ones extracted from the infinite quantum well model given by equation (2.3).

One more way to increase the confinement is to increase the thickness of the tunneling barriers. Figure 2.5 shows TM calculations for barrier thicknesses from 2 nm to 10 nm for a quantum well width of 8 nm, a barrier height of 440 meV and an additional imaginary quantum well potential of  $\Gamma = 0.3$  meV. The increase in confinement results again in a reduction of both the non resonant contributions and the amplitudes of the resonant features.

All these findings are only valid as long as no voltage drops across the layer stack



and tilts the conduction band profile. Since a bias voltage is however needed to align the resonant states with the electrons in the emitter, this simplified model obviously brakes down. A theoretical description for a tilted conduction band profile is possible within the framework of the TMM discussed above, as it can be used for arbitrary potential landscapes. However, a strong tilt requires the steps dl to be small to gain regions of quasi constant potentials. For each applied bias voltage (that is every data point of the measurement), the potential profile and the  $T(E_e)$  spectrum thereof needs to be calculated since the potential landscape is altered.

## 2.3 Tilted conduction band profiles

In our DMS RTDs, resonance conditions are reached by applying a bias across the resonant tunneling diode. As the voltage drop over the first barrier and the quantum well is needed to align the quantum well state with the emitter electrons, the resulting conduction band profile is continuously altered during the measurement. In this section we examine the transmission probability through a double barrier structure as a function of the applied bias voltage.

Figure 2.6 shows a self-consistent conduction band profile of a (Zn,Be)Se heterostructure with an applied bias voltage of 200 meV, computed with the Wingreen simulation package [Indl 04]. As boundary conditions, we assume a pinned Fermi energy to account for the band bending at the metal contact interfaces. High doped ZnSe ( $n \approx 10^{19} \text{ cm}^{-3}$ ) layers at these semiconductor-metal interfaces are needed for a proper contacting scheme. The shaded gray area highlights the active region of the RTD. An applied bias voltage drops mainly across the intrinsic (not iodine doped) active region and the contacts. As is clear from fig. 2.6, the shaded part of the conduction band profile can be approximated by a uniform electrical field.

This shaded region is now divided into five regions, as shown by the labels 1 through 5. The voltage drop  $V_{AR}$  across the active region (regions 2-4) is only a fraction of the applied bias voltage in a real device.  $V_{AR}$  however dominates the device properties, as it responsible for the actual resonant tunneling process (therefore it is often referred to as the "active region"). Following the horizontal black line, depicting the Fermi level in the emitter, it is clear that due to the applied bias voltage, the emitter electrons incident to the barriers will find a double barrier system of reduced symmetry and effective barrier height (compared to the flat band case of fig. 2.1a). As a guide to the eye, the latter is indicated by the black arrows inside the tunnel barriers in fig. 2.6.

The solution to the Schrödinger equation for a uniform electrical field (linear potential) is given by the Airy functions and the transmittance of such a tiled double barrier system can be solved [Alle 94, Alle 96, Miya 98] analytically. Numerically inverting parts of the total transfer matrix with the Airy functions however results in ill-conditioned matrices especially for low bias voltages and low electron energies.

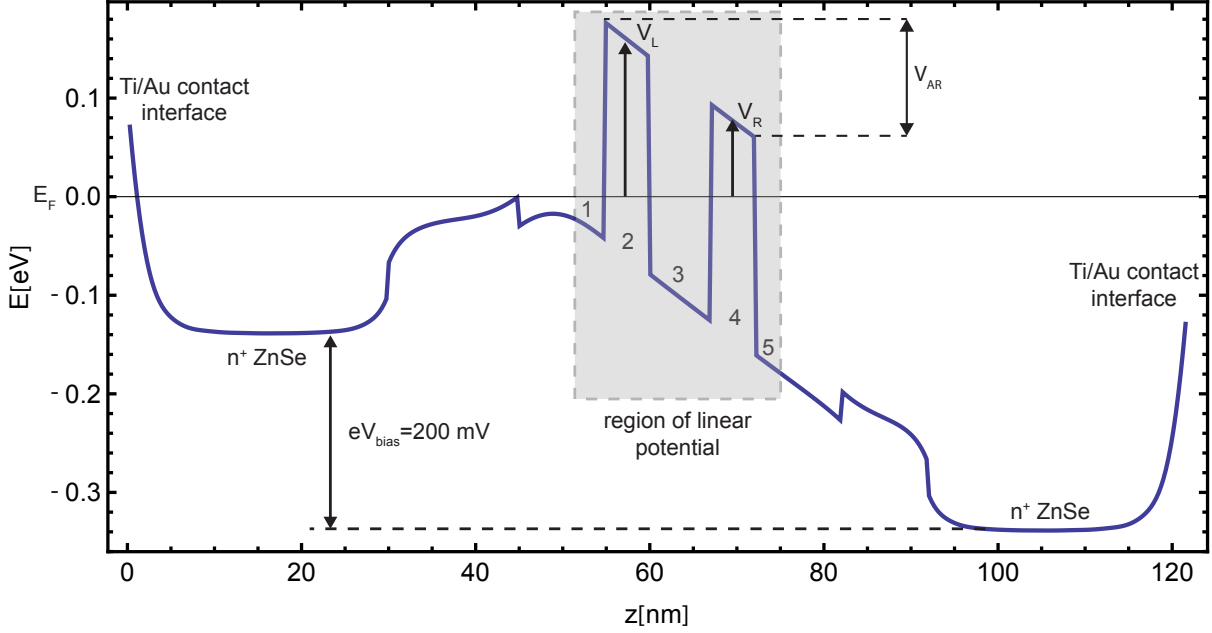


**Figure 2.6:** Self consistent conduction band profile for a (Zn,Be)Se heterostructure at an bias voltage of 200 mV applied across the layer stack. Fermi levels are pinned at the metal contacts to account for the strong band bending at the metal-semiconductor interface.

A tilted potential landscape as in the shaded area of fig. 2.6 can also be calculated with the TMM approach given in section 2.2 if the potential landscape is divided into sufficiently small parts  $dz$ . This can be tested easily by decreasing  $dz$  until the resulting transmission spectrum stops changing. The model was also tested in the limit of  $V_{AR} \rightarrow 0$  V and yields, in contrast to the Airy function approach, identical results for the flat band case.

While the potential landscape is symmetric under flat band conditions, the asymmetry induced by an applied bias voltage will not lead to a transmittance of unity since the latter can only be achieved for the case of two barriers with identical transmittances  $T_L$  and  $T_R$  [Ricc 84, Butt 88, Lury 89]. For a device with two identical tunnel barriers, the second barrier will always be lower than the first one with respect to the kinetic energy of the incident electron. The symmetry of the conduction band profile is thus more and more reduced as the applied bias voltage is increased. This effect could be compensated by a higher and/or thicker second barrier. The optimization of the latter is very difficult in reality, as one can only optimize for a single bias voltage and the underlying tilt of the conduction band profile. The result does however not necessarily yield a resonance in the I-V characteristics as is discussed in detail in reference [Ricc 84].

Figure 2.7a shows the transmittance  $T(E_e, V_{AR})$  as a function of the voltage drop  $V_{AR}$  across the active region for a constant incident electron energy of  $E_e = 8.5$  meV. The two apparent transmission peaks look alike on a logarithmic scale and show comparable peak heights of one order of magnitude with respect to the background current. Figure 2.7b

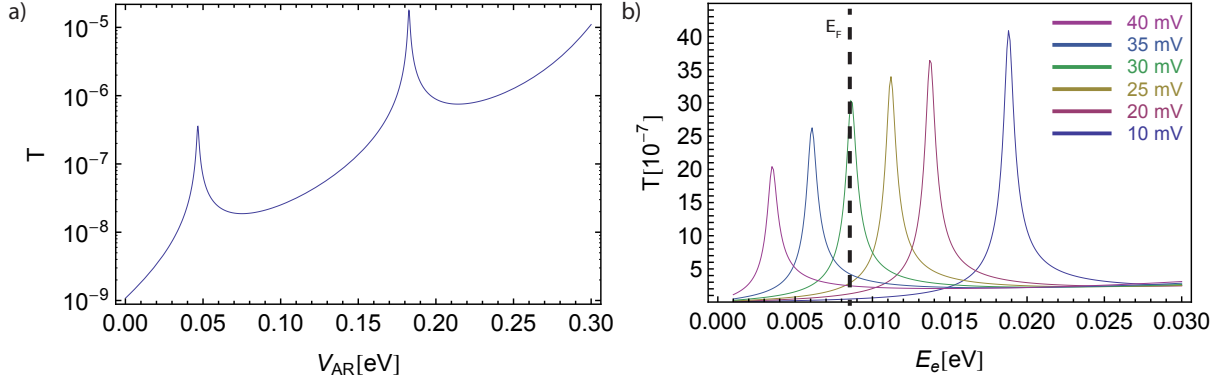


**Figure 2.7:** a) The transmission probability  $T$  at a constant electron energy at the conduction band edge as a function of the voltage drop  $V_{AR}$  across the active region b) The transmission probability as a function of electron energy for various  $V_{AR}$  in the vicinity of the Fermi energy. While the resonant level is lowered with respect to the electronic states of the emitter, the change in the potential landscape due to the increase in bias voltage alters the transmission spectrum of the bound state.

however shows that increasing the bias voltage will reduce the transmission on resonance. The loss of transmittance stems from the reduced symmetry, since an increase in  $V_{AR}$  also increases the tilt of the conduction potential profile. Therefore as one sweeps the RTD through a resonance via the applied bias voltage, even for an idealized clear cut picture as shown in fig. 2.6 the shape of the resonant peak will slightly be deformed as the underlying potential is continuously altered. We note that if the fidelity of the resonance is already limited by a phase breaking process as discussed above, such optimization will most likely yield no gain in fidelity.

The blue and black peaks in fig. 2.7b depict the transmission for  $V_{AR}$  settings of 40 and 10 mV, respectively. Comparing to the energy scale of the plot, the resonance is however only moved by approximately 15 meV. Considering only the active region of an RTD, a ratio of  $l=V/E$  of 2 is a reasonable approximation to link the voltage drop across the active region to energy scale of the problem. This ratio is often referred to as the lever arm of the device. In literature, this value is mostly comparing the total applied bias voltage  $V_{app}$  to the energy scale of the problem, and thus deviates from the value 2. This discrepancy can arise from an asymmetry of the active region, as well as all effects that reduce the ratio of  $V_{AR}/V_{app}$ , such as contact resistances.

## 2.4 Implications of contact resistances

Figure 2.8a shows the simple equivalent circuit for a typical transport measurement on a DMS RTD. We apply a DC bias voltage  $V_{DC}$  to the device in series with a resistor  $R_S$ . The voltage drop across  $R_S$  is used to measure the current through the RTD. Such an I-V characteristic of a DMS RTD (8% Mn, 7 nm quantum well) is shown in fig. 2.8b for both

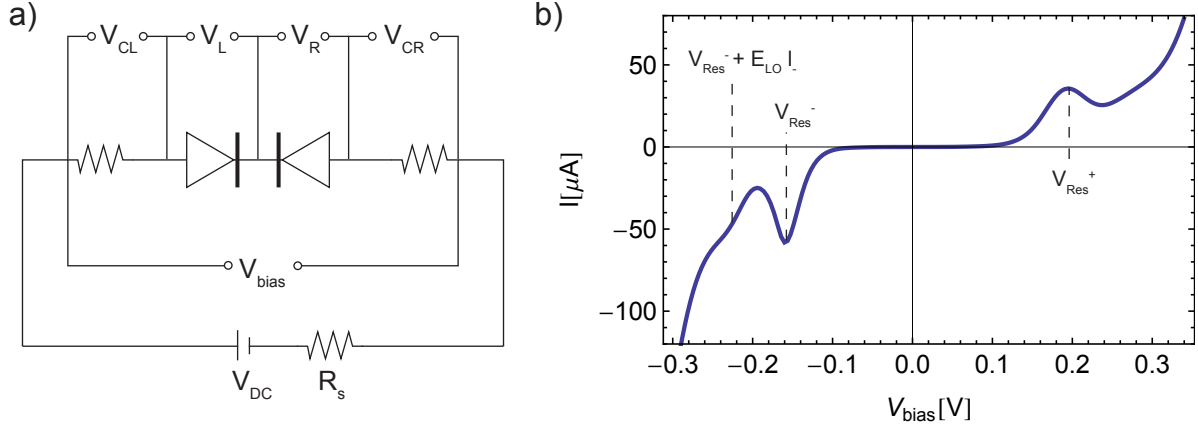


**Figure 2.8:** a) Equivalent circuit of a standard I-V measurement. A series resistor  $R_s$  is used to measure the current traversing the RTD. b) I-V characteristic of such a measurement for both negative and positive bias voltages. The apparent asymmetry of the device results in different peak positions, shapes and amplitudes for bias voltages of opposite sign.

negative and positive bias voltages at  $B=0$  T. The voltage drop  $V_{bias}$  across the device includes the voltage drops at the contact resistances  $V_{CL}$  and  $V_{CR}$  on both ends of the RTD as well as the voltage drop  $V_{AR} = V_L + V_R$  across its active region. For simplicity we here redistribute any voltage drop across the quantum well layer  $V_{qw}$  equally among the voltage drops  $V_L$  and  $V_R$  across the left and right tunnel barrier, respectively.

Figure 2.8b shows a second peak of reduced amplitude and increased width with respect to the first resonance at  $V_{LO}^- = -228$  mV. While the first quantum well level is already lowered below the conduction band of the emitter, resonant tunneling is still possible while exciting a longitudinal optical (LO) phonon [Gold 87a]. A second peak thus arises when the energetic distance between the emitter electrons and the quantum well state is exactly the LO phonon energy of the crystal. This replica peak is often used to make an estimate for the lever arm of the device as the energy for the LO phonon in ZnSe is known [Land 99] and the difference in voltage can be determined from the I-V characteristics. The replica peak at positive bias voltages is hardly visible in the I-V characteristic, and its position  $V_{LO}^+ = 299$  mV is therefore determined via the first derivative  $dI/dV$  (not shown).

As  $l_-$  and  $l_+$  are related to the voltage axis of our measurements, we can determine them from characteristic features in the I-V characteristics, such as the LO replica peak (see fig. 2.8b). Using  $l_{\pm} = (V_{LO}^{\pm} - V_{Res}^{\pm})/E_{LO}$ , we find lever arms of 2.2 and 2.4 for negative and positive bias voltages, respectively. We however have no direct access to  $l_L$  and  $l_R$ , which are the lever arms related to the voltage drop across the left and right tunnel barrier. They thus are descriptive of the symmetry of the active region of the

RTD. From fig. 2.8a it is clear that they relate via

$$\frac{1}{l_L} + \frac{1}{l_R} = \frac{V_L}{V_{AR}} + \frac{V_R}{V_{AR}} = 1 \quad (2.9)$$

The device lever  $l_-$  and  $l_+$  include the voltage drops across the contacts. Using the equivalent circuit of fig. 2.8a, they read

$$l_- = \frac{V_{bias}}{V_L} = \frac{V_{AR}}{V_L} + \frac{V_C}{V_L} = l_L + \frac{V_C}{V_L} \quad (2.10)$$

$$l_+ = \frac{V_{bias}}{V_R} = \frac{V_{AR}}{V_R} + \frac{V_C}{V_R} = l_R + \frac{V_C}{V_R} \quad (2.11)$$

where  $V_C = V_{CL} + V_{CR}$  is the total voltage drop across all contact resistances. Using the same approach as in equation (2.9) for  $l_-$  and  $l_+$  yields

$$\begin{aligned} \frac{1}{l_-} + \frac{1}{l_+} &= \frac{V_L}{V_{bias}} + \frac{V_R}{V_{bias}} = \frac{V_L + V_R}{V_{bias}} = \frac{V_{bias} - V_C}{V_{bias}} \\ &= 1 - \frac{V_C}{V_{bias}} \end{aligned} \quad (2.12)$$

By simply comparing the sum of the inverse lever arms to unity, we thus have a tool to estimate the internal (contact) resistance in our devices. As RTDs are highly non-ohmic resistors, we approximate the device resistance by using the on-resonance resistance at negative bias voltage  $R_{Res}^-$  to approximate  $V_C/V_{bias} \approx R_C/R_{Res}^-$ . Using equation (2.12) we thus find a total contact resistance of approximately 320  $\Omega$  for the device shown in fig 2.8b. Two similar DMS RTD using the same contacts as the device considered here are presented in chapter 3. Fits to the I-V characteristics for these devices yields series resistances of 250 and 400  $\Omega$ , in good agreement with the estimate from this simple lever arm model.

## 2.5 Comparison to experiment

In order to test our findings, we plot the eigenenergies of the first two resonant quantum well states as a function of the quantum well width in fig. 2.9. For a comparison with experiment, the voltages at which the resonances occur (negative bias voltage applied to the top of the layer stack given in fig 2.9b) are converted to an energy scale by dividing  $V_{Res}$  by a lever arm of 2.4, in good agreement to the ones determined from the experimental data. The result yields an offset of 30 meV between theory and experiment, which is subtracted in fig. 2.9a. The offset is likely stemming from simplifying assumptions in the model, such as using an equal mass for the emitter, collector, quantum well and tunnel

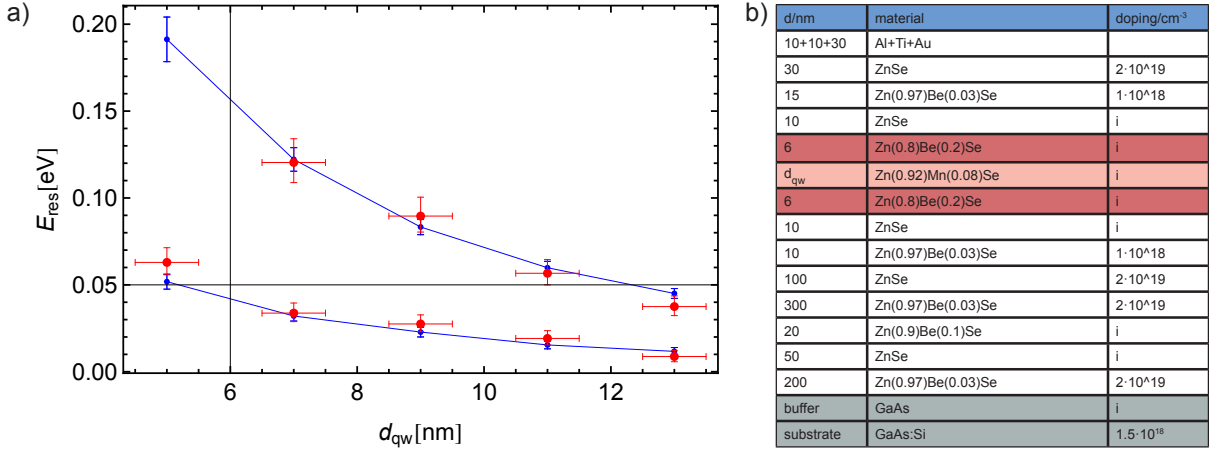


**Figure 2.9:** a) Comparison of the peak positions (blue dots) determined by a flat band TM model to experimentally observed peak positions (red dots) for DMS RTDs of various quantum well widths. For a description of the error bars, see text. b) layer stack of the DMS RTDs

barrier materials [Ohno 90]. Moreover, we did not account for changes to the conduction band offset in the quantum well layer by the incorporation of the magnetic impurities [Dai 94]. Any deviations from the assumed digital iodine doping profile will also result in a bending of the conduction band profile, shifting the quantum well state with respect to the emitter.

The error bars for the of the calculated level positions in fig.2.9 (blue dots) are generated by running calculations for worst case combinations of the individual parameter variations. We assume an error of  $\pm 40$  meV for the barrier height, as well as a variation of the barrier thickness of  $\pm 0.5$  nm. Both effects the confinement of the state and thus changes its eigenenergy. As is clear from the vertical error bars, errors due to a change in the confinement are most prominent for levels located at the top of the quantum well, where the confinement is already weak.

We furthermore assume an uncertainty of  $\pm 0.5$  nm for the actual width of the quantum well layers used in the measurements, which results in the horizontal error bar of the red dots. There will also be a small variation in the symmetry of the device as well as in the contact resistances. This is all captured within the lever arm of the device. From experience, we assume a variation for the lever arm of  $\pm 0.2$ . The vertical error bars of the red dots are dependent on the energy of the quantum well state, as  $dE = V_{Res}/l - V_{Res}/(l + dl)$ .

Additionally, also the aforementioned shift of 30 meV of the quantum well conduction band could very well also show a weak dependence on the quantum well width, we however assume that this error is smaller than the one stemming from the variation of the quantum well layer thickness.

## 2.6 Empirical modeling of resonant tunneling conductance

Having established the transmission spectra of a double barrier heterostructure both as a function of the incident electron energy and the applied bias voltage, this section will now discuss if the latter is applicable for the modeling of the I-V characteristics of all II-VI semiconductor RTDs.

Assuming that the transmission through the double barrier region of the RTD is described by running a TMM on a self-consistent conduction band profile, the calculated line width for the resonance is very sharp (sub meV). Near the resonance this transmission line shape is described by a Lorentzian [Lury 89] and thus reads

$$T(E_e) = \frac{4T_L T_R}{(T_L + T_R)^2} \frac{\gamma^2}{(E - E_e)^2 + \gamma^2} \quad (2.13)$$

where  $\gamma$  is the intrinsic width of the resonant state and  $T_L$  and  $T_R$  are the transmittances of the left and right barrier, respectively.

The transmission spectra is however only a measure for the probability of an electron of energy  $E_e$  to traverse the underlying potential landscape. It does not yet fully describe the current through the RTD. An intuitive picture for the 3D-2D tunneling current is given by [Lury 85] and is briefly reviewed in the following.

Assuming conservation of the lateral momentum, only emitter electrons of a certain  $k_z$  value are able to tunnel into the quantum well state. The selection of a single  $k_z$  value is a result of the afore discussed narrow intrinsic width of the resonant transmission through the quantum well state. Which  $k_z$  values are selected depends on the energetic position of the resonant state with respect to these emitter states. As soon as there is an overlap with occupied states in the emitter, the resonant level in the quantum well, as well as unoccupied states in the collector, the resonant current sets in. This overlap of the density of states in the emitter and the density of states in the quantum well is schematically shown for three bias voltages  $V_1, V_2$  and  $V_{max}$  by the gray discs in fig. 2.10b. We omit the collector states, as for bias voltages much greater than the bandwidth of the emitter, there will always be empty states available in the collector. At  $V_{max}$  and  $k_z = 0$  the maximum overlap of the density of states is reached and a further increase in bias voltage will produce a sharp cutoff in the I-V characteristic (assuming a sufficiently sharp transmission spectrum). For a specific  $k_z$ , the area where the density of states in the emitter and the quantum well overlap is given by

$$I \propto A_I(k_z) = \oint \int_0^\infty \frac{1}{1 + \exp\left[\frac{\hbar^2}{2m_{eff}} \left(\frac{k_r^2 + k_z^2 - k_F^2}{k_B T}\right)\right]} k_r dk_r d\phi \quad (2.14)$$

Figure 2.10 depicts this finite temperature extension to Luryi's picture for resonant

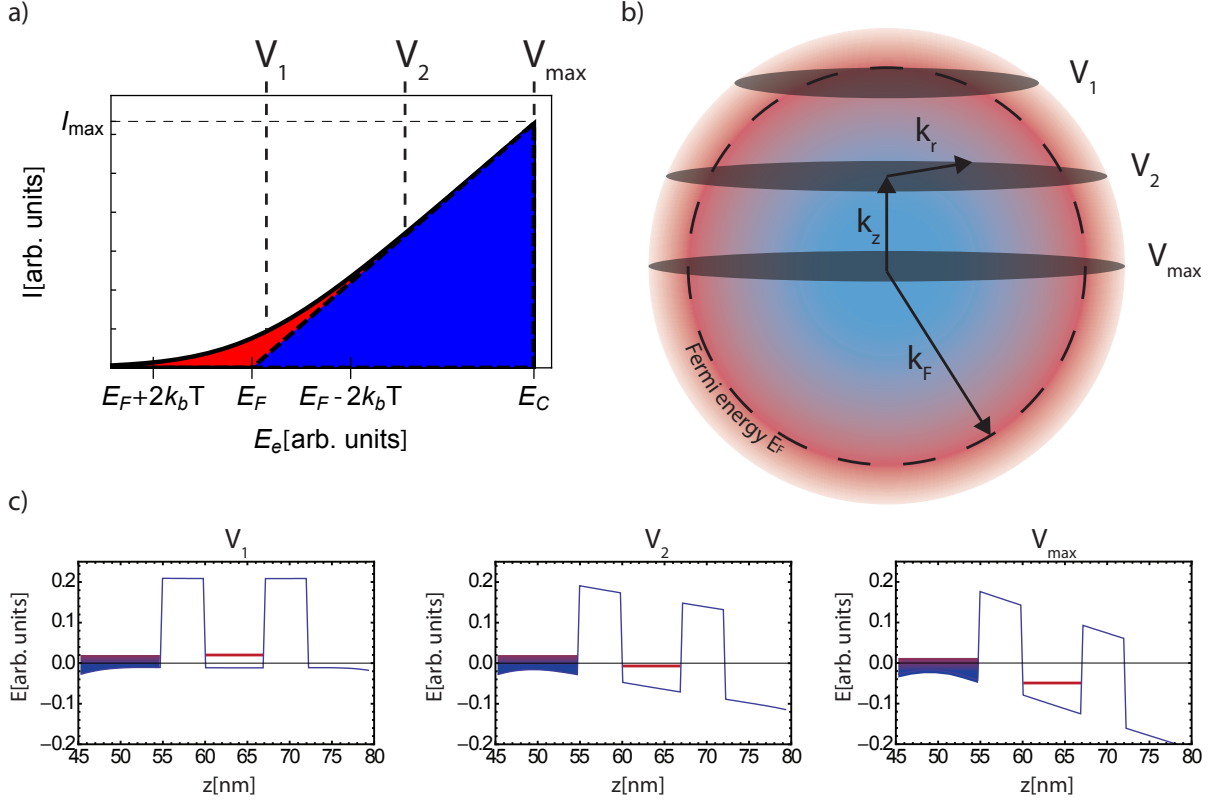


**Figure 2.10:** The Luryi picture for resonant tunneling extended for finite temperatures. a) Schematic of the resulting I-V characteristics without a non-resonant background current contribution. b) The emitter Fermi sphere for finite temperature. The red color illustrates the smearing of the Fermi distribution at the Fermi energy. The three gray disks depict the intersection of the Fermi sphere with the density of states of the resonant level in the quantum well for the onset voltage  $V_1$ , an intermediate voltage  $V_2$  and the bias voltage  $V_{max}$  where the resonant level is aligned with the conduction band edge and the resonant current reaches its maximum. For a given voltage  $V_i$  the current  $I(V_i)$  is proportional to this gray area. c) Conduction band profiles for the applied bias voltages in a) and b). The position of the resonant level (red line) with respect to the emitter Fermi sea (blue) is lowered by increasing the bias voltage. The effects of the band bending visible in these conduction band profiles are *not* included in the Luryi picture

tunneling and shows how the Fermi smearing alters the onset of the resulting I-V characteristics, but not the sharp end of the peak at higher voltages. While equation (2.14) is calculated in  $k$ -space, fig. 2.10a plots the dependence of the tunneling current as a function of the applied bias voltage. The energy separation  $\Delta E$  between the quantum well level and the conduction band edge in the emitter is linked to the applied bias voltage  $V_{app}$  and reads

$$\Delta E = E_0 - V_{app}/l = (\hbar k_z)^2 / (2m_{eff}) \quad (2.15)$$

where  $E_0$  is the energetic distance of the quantum well state to the conduction band edge



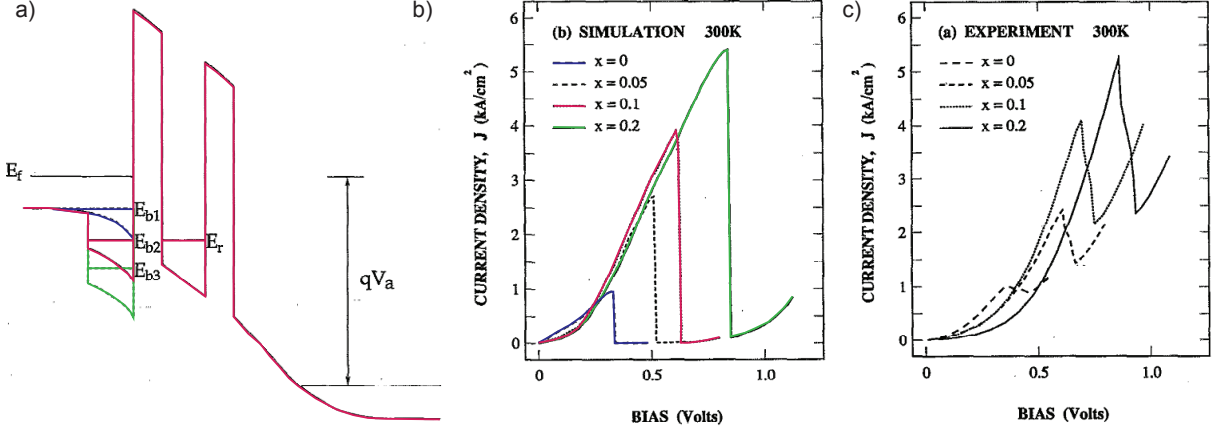


**Figure 2.11:** Pictures from [Choi 92], color added as a guide to the eye. a) Conduction band profile of a III-VI RTD for emitter n-doping concentrations of 0 (blue), 10 (red) and 20% (green). b) calculated I-V characteristics for the various doping concentrations at room temperature. c) Measurements corresponding to a)+b)

at  $V_{app}=0$ .

In order to be able to compare this model to a device I-V characteristic, equation 2.14 is thus plotted as a function of  $k_z^2$  in fig. 2.10a. As is clear from fig. 2.10a, for an ideal 3D-2D resonant tunneling process, the width of the resulting resonance-peak in the I-V characteristic is governed by the bandwidth of the emitter Fermi sea, since it is large (tens of meV) compared to the transmission line width (sub meV).

An example of such emitter dominated resonant tunneling transport at room temperature is shown in [Choi 92]. Figure 2.11 shows the findings of Choi et. al for various 3D emitters of different bandwidth. Increasing the Fermi energy of the emitter Fermi sea clearly results in an increased width of the resonance-peak in the I-V characteristics of the respective sample, in good agreement to Luryi's picture of 3D-2D resonant tunneling. Also the aforementioned thermal broadening is clearly observed in the onset of the I-V characteristics at 300 K.

For a sharp cutoff of the I-V characteristic at the conduction band edge, broadening on the onset of the resonant peak can be allocated to temperature smearing of the emitter Fermi sea. In case of broadening at the high bias voltage side of the peak, the line width of the resonant state is however no longer negligible.

Most II-VI resonant tunneling devices examined in Würzburg so far, neither represent the shape expected from the Luryi picture nor resemble a Lorentzian line shape. The best fits to the I-V characteristics while accounting for the background current and the contact resistances are achieved by assuming a Gaussian shaped conductance peak to model the apparent resonances. As will be shown later in this thesis, this Gaussian broadening of the resonance-peaks is persistent to cooling of the electron system and thus cannot be of thermodynamic nature.

Figure 2.12a shows a schematic of the afore discussed ideal 3D-2D tunneling density of

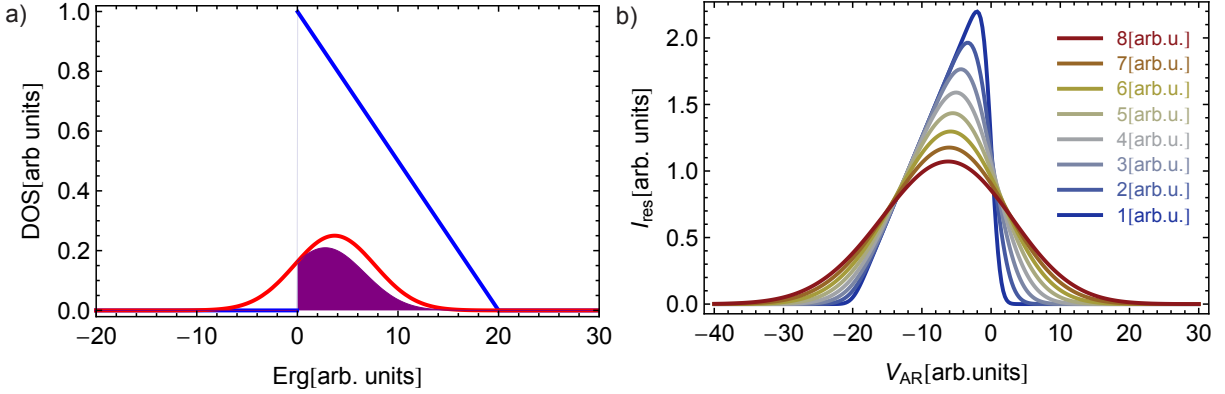


**Figure 2.12:** a) Overlap (purple shaded area) of the tunneling density of states (blue line) with the density of states of the intrinsic quantum well state (red line) for a given bias voltage where the quantum well state is almost aligned with the conduction band edge. b) I-V characteristic for various intrinsic line widths of the quantum well state. As the variance of the quantum well state is increase and becomes comparable to the band width of the emitter electrons, the line shape of the quantum well state dominates the resulting G-V characteristic which then more and more deviates from the expected result given by the Luryi picture of resonant tunneling.

states (blue curve) at  $T=0$  K as a function of the energetic distance from the conduction band edge. We now introduce an additional broadening mechanism (red curve), which is attributed to the quantum well state. At a bias voltage  $V_{AR}$  which levels the quantum well state near the conduction band edge of the emitter, the overlap (purple shaded area) of these curves is proportional to the resonant current at  $V_{AR}$ . The latter is plotted for various intrinsic (Gaussian) line widths as a function of  $V_{AR}$  in fig. 2.12b (lever arms and replica peaks from LO-phonon assisted tunneling processes are omitted for simplicity).

As long as the intrinsic width  $\Gamma_i$  is much smaller than the emitter bandwidth, the resulting I-V characteristic will resemble what is predicted by the Luryi picture. Such an I-V characteristic is to be expected for high quality material systems like GaAs/(Al,Ga)As where the line width of the quantum well state is much smaller than the emitter bandwidth [Lead 89, fig. 1]. For  $\Gamma_i \gtrsim E_F$  however, the resulting I-V characteristics will to a good approximation only resemble the intrinsic line shape of the 2D quantum well state. Figure 2.12b also shows that due to the broadened intrinsic line width, the maximum current does not occur at the conduction band edge as predicted by the Luryi picture, but shifts towards a smaller  $V_{AR}$ .

A likely broadening mechanism for a II-VI quantum well RTD are quantum well width fluctuations. All transfer matrix calculations as well as the self-consistent conduction band profile calculations in this thesis are done in 1D. The layer stack of the heterostructure, even though grown by MBE, will however not be perfectly flat. For an ideal resonant tunneling diode, the transmission does not depend on the x and y coordinates and the problem reduces to one dimension, where the x-y distribution of the electronic states only enter as described in the Luryi picture shown in fig. 2.10. For a device exhibiting thickness

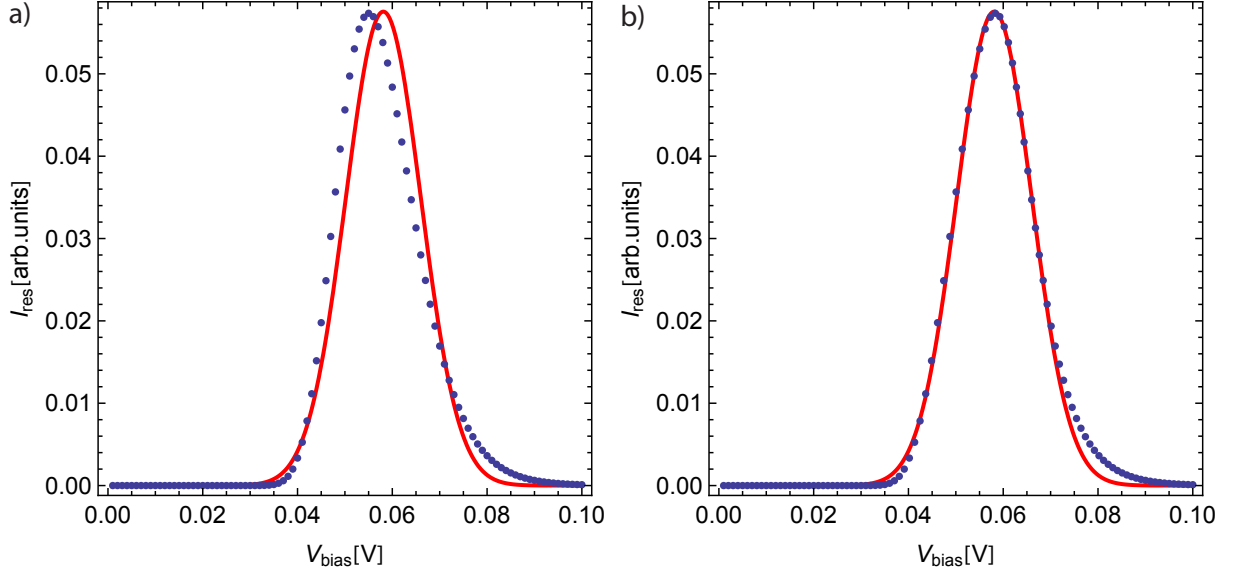


**Figure 2.13:** a) resonant currents for a pure Gaussian conductance (red line) and for a energy distribution calculated from a Gaussian quantum well thickness distribution (blue dots) with a variance of 0.5 nm b) the I-V characteristic calculated from the thickness fluctuations (blue dots) subjected to small series resistance. The red curve again depicts an I-V characteristics from a pure Gaussian conductance peak.

fluctuations of the quantum well layer, one can think of the RTD pillar as a large number of 0D RTDs, each with its own quantum well width. These subspaces conduct in parallel and show resonances occurring at different bias voltages due to their slightly different eigenstate energies.

The thickness fluctuations can be described by a Gaussian distribution of  $d_{qw}$  as the relevant length scale is likely to be in the order of tens of nm and the mesa is thus comprised of a large number of subspaces. Using the simple picture of an infinite quantum well ( $E_{qw} \propto 1/d_{qw}^2$ ), the resulting distribution of eigenstate energies is however not exactly bell shaped. Figure 2.13a shows an I-V characteristic assuming a single Gaussian conductance peak (red line) while omitting the non-resonant background current. The I-V characteristic that result from a Gaussian distribution of the quantum well width (blue dots) is slightly tilted towards lower bias voltages compared to I-V characteristics calculated from a bell shaped conductance. In fig. 2.13b it is however shown that adding a small intrinsic series resistance  $R_S$  converts the dotted curve to the bias axis of the red line via  $V_{\text{bias}} = V_{\text{bias}}^* + R_S I$  and compensates for this asymmetry.

Using a Gaussian conductance peak therefore still is a good approximation. The analysis in [Ruth 11] focusses on the changes in amplitudes and the energetic positions of the resonant peaks. While using a Gaussian conductance adds no error to the determination of the peak position and height, it will only result in slightly overestimating the intrinsic series resistance of the device, since as shown in fig. 2.13b, an additional series resistance will compensate the deviations between the two distributions. While there are still small

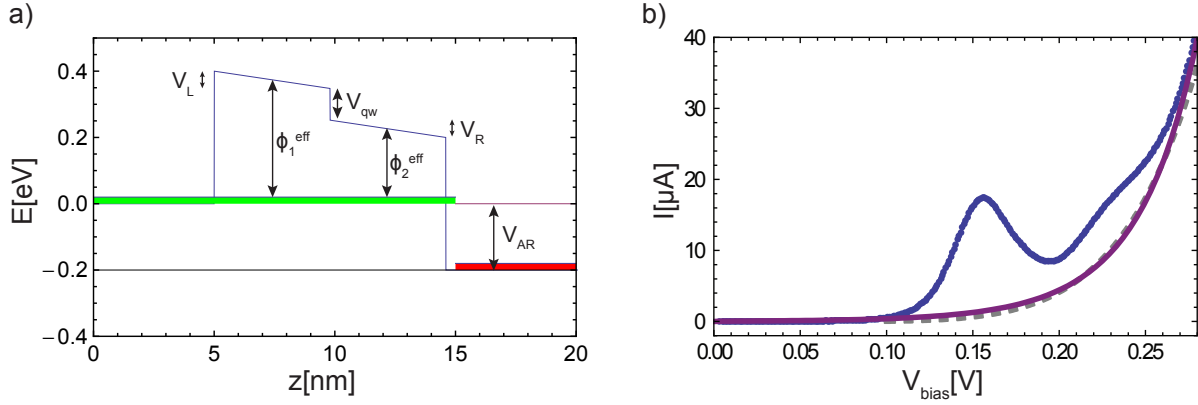


**Figure 2.14:** a) Schematic conduction band profile used for the TMM calculation at  $V_{AR}=200$  mV. The quantum well layer is omitted to hinder the formation of resonances. The voltage is assumed to only drop at the barrier regions of the device. b) I-V characteristic of a DMS RTD with two 5nm (Zn,Be)Se barriers (blue circles) and the calculated background current (purple line). The gray dashed line represents a fit to the background current with  $I_{bg} = c_1(c_2 V_{bias})^{c_3}$

discrepancies remain in both onset and tail of the resonant peak, the resulting error is very likely to be negligible since fits are usually optimized for the peak maxima.

## 2.7 The non-resonant background current

Assuming a Gaussian line shape to fit the resonance-peaks in the I-V characteristics of the RTDs still lacks the description of all electrons that tunnel through the two series barriers off resonance. We know from experiment that this background current is highly dependent on the applied bias voltage. The transmission probability  $T_{bg} \approx T_L T_R$  for an electron at small bias voltages is very low, since it has to essentially tunnel through a potential step comprised of the left barrier with the transmittance  $T_L$  and the right barrier with the transmittance  $T_R$  [Ricc 84]. Both tunnel barriers are several hundred meV higher than the electron's kinetic energy and approximately 5 nm wide. As is shown in fig. 2.14a, for a voltage drop  $V_{AR} = V_L + V_{qw} + V_R$  across the active region of the device, the second barrier is however already lowered by the voltage drop  $V_L$  across the first barrier and the voltage drop  $V_{qw}$  across the quantum well. At bias voltages comparable to the barrier height the background current increases massively, since tilting the tunnel barriers via  $V_{AR}$  reduces the effective barrier heights  $\phi_1^{eff}$  and  $\phi_2^{eff}$  for the incident electrons.

Even though the quantum well layer is not doped, charge will be present in this layer as soon as the resonant steady state is established [Ricc 84]. Self consistent calculations of the conduction band profile suggest a bias voltage drop at the quantum well which is of the same order as the potential drop at the barriers. An example of such a calculation is shown in fig. 2.6 for an RTD with 5 nm tunnel barriers and a 8 nm quantum well. Charging of the quantum well will of course depend on the tunnel barrier and quantum

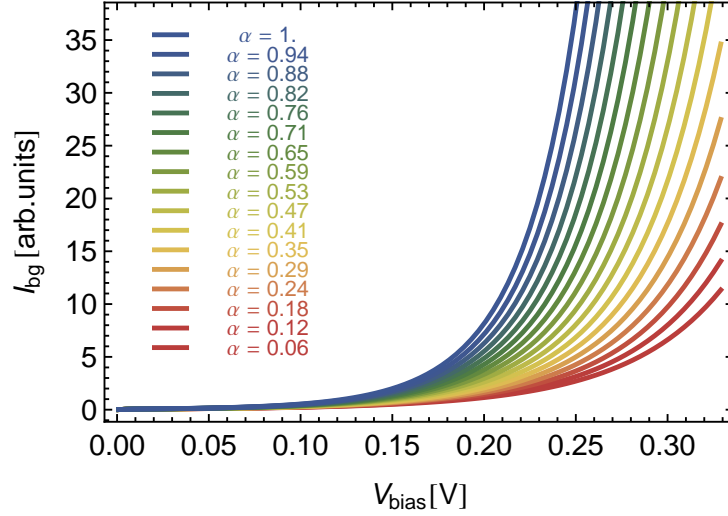


**Figure 2.15:**  $I_{bg}$  for various voltage drops at the quantum well layer.  $\alpha$  denotes the ratio of the electric fields  $\varepsilon_{qw}/\varepsilon_{barriers}$

well properties of the device and should not categorically be neglected, especially for asymmetric devices where the collector barrier is limiting the transport.

Charge build up in resonant tunneling double barrier structures is possible [Shea 88, Buot 00], and was demonstrated in optimized asymmetric structures [Zasl 88]. The charging leads to bistabilities and hysteresis in the I-V characteristics. In our II-VI RTDs, this intrinsic bistability is however not observed which is most likely due to chosen symmetric layout paired with the broadened resonances observed in these devices. In the theoretical discussion of the intrinsic bistabilities due to charging of reference [Shea 88], it is stated that "[...] the intrinsic bistability could be reduced or removed by a large inhomogeneous broadening of the bound state". In the light of this, we assume that while a fraction of the applied bias voltage drops across the quantum well layer, the magnitude of  $V_{qw}$  is partially reduced due to the presence of charges.

As we are interested in a description of the background current, we omit the quantum well layer as shown in fig. 2.14a. Without a quasi bound state between the tunnel barriers, no resonance occurs in the calculated transmission spectrum. The  $k_z$  selection rules discussed in fig. 2.10b do therefore not play a role for electrons tunneling off-resonance through the double barrier region. Omitting the quantum well region for the calculation of  $I_{bg}$  does however *not* imply that the voltage drop across this layer is to be neglected. Tilting only the barrier potentials or dividing the voltage drop among barriers and quantum well layer with regard to their layer thickness, dielectric constants and charging makes a huge difference for the resulting transmission probability at a given energy of the incident electron. Hence we can test our assumption that a non negligible portion of the applied bias voltage drops across the quantum well by comparing calculations for the various cases against a measured I-V characteristic of an RTD where the barrier and quantum well thicknesses are known from XRD measurements of the layer stack [Frey 10].

Assuming a constant emitter Fermi energy,  $I_{bg}$  is given by [Tsu 73]

$$I_{bg} = c_{bg} \int_{E_c}^{\mu+2k_B T} T(E_e, V_{bias}) \cdot dF(E_e, V_{AR}) dE_e \quad (2.16)$$

with the transfer function

$$dF = \ln \left[ \frac{1 + \exp \left[ \frac{\mu - E_e}{k_B T} \right]}{1 + \exp \left[ \frac{\mu - E_e - eV_{bias}}{k_B T} \right]} \right] \quad (2.17)$$

which weighs occupied emitter states against unoccupied collector states and results in a linear slope for bias voltages  $V_{bias} < lE_F$ . In this bias range transport is not only governed by  $T(E_e)$  but also by the small number of unoccupied electron states in the collector. The transfer function saturates for bias voltages in the order of the Fermi energy and above. For  $V_{bias} \gg lE_F$  it plays a minor role in the shape of the discussed  $I_{bg}$ -V characteristic. The Fermi statistics however play an important role in chapter 8, where their implications for the resonant tunneling transport at  $V_{bias} < lE_F$  will be discussed.

Figure 2.15 plots equation (2.16) for one  $c_{bg}$  and various voltage drops at the quantum well layer.  $\alpha = \mathcal{E}_{qw}/\mathcal{E}_{barriers}$  denotes the ratio between the electric fields in the quantum well and the barrier regions. As we increase  $\alpha$  and thus the voltage drop across the quantum well layer, the model yields an increase in the background current. A large voltage drop across the quantum well layer thus results in a strong contribution from the non-resonant background current. This should be considered in the sample design while planning RTDs with wider quantum well layers, as  $V_{qw}$  is also likely related to the width of the quantum well.

In fig. 2.16 we plot equation (2.16) (purple curve) for various  $\alpha$  from 0.06 to 1 and use  $c_{bg}$  to fit each curve to the experimental data (black curve). The best result is achieved by assuming an electric field in the quantum well layer which is approximately 20% lower ( $\alpha=0.76$ ) than in the barriers. This analysis is best done by subtracting the calculated background current from the experimental I-V characteristic and comparing the resulting curve (blue line) to the shape of the resonant contribution in fig. 2.13

As shown in fig. 2.14b, this calculated background current  $I_{bg}$  (purple curve) can furthermore be fitted (gray dashed line) by a power law

$$I_{bg} = c_1 (c_2 V_{bias})^{c_3} \quad (2.18)$$

Our model thus shows that the voltage dependence of the background current in an RTD can be explained by the dependence of the non resonant transmission probability through the two barriers in series. It should be noted that in this section only the voltage drop  $V_{AR}$  across the double barriers and the quantum well are considered. As the I-V characteristics of experimental data include effects from both intrinsic (contacts) and

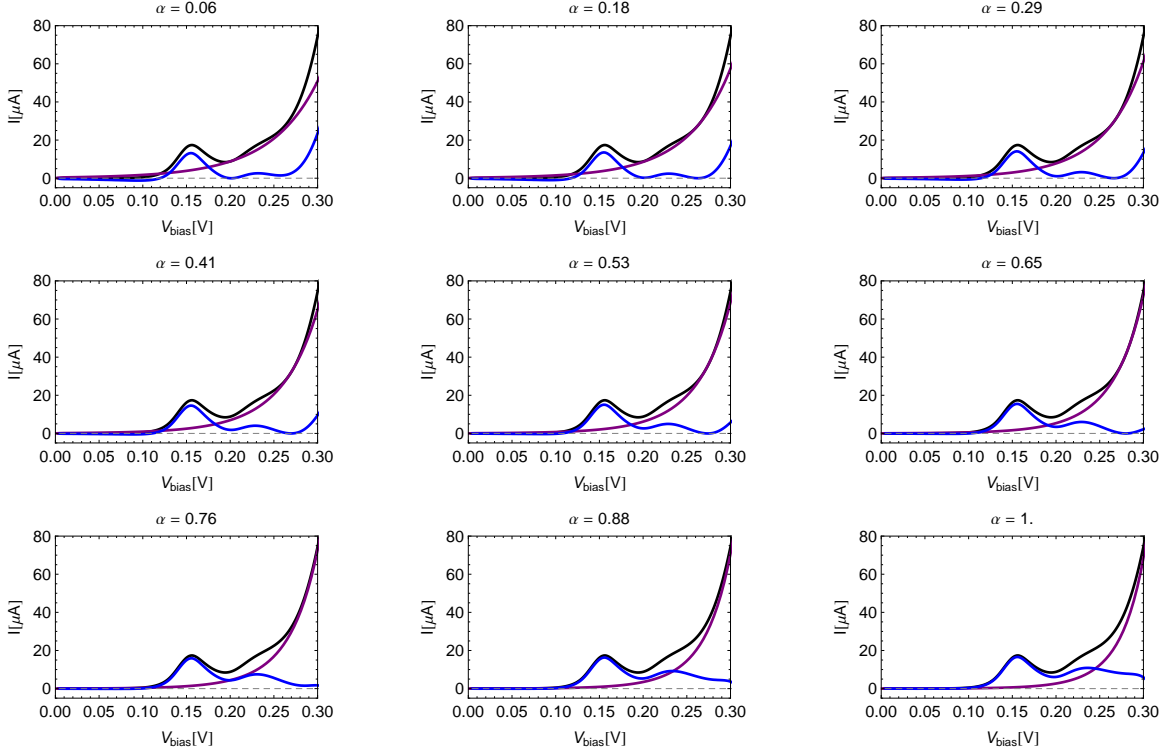


**Figure 2.16:** the difference (blue line) between the I-V characteristic of the real device (black line) and the modeled background current  $I_{bg}$  (purple line)

external series resistances, fitting equation 2.16 directly to experimental data in fig. 2.14b still is an approximation.

In chapters 3,4 and 5 this model for the background current is used as a building block in the equivalent circuit of an RTD. In combination with other circuit elements such as the afore discussed resonant contributions and contact resistances it is able to capture the essence of a DMS RTD. The parameters of equation (2.18) for the fits in the following chapters are fine-tuned within the full model and do not make the same approximations as the fit in fig. 2.14b.

## 2.8 The DMS RTD as a voltage controlled spin-filter

In the previous sections we established an empirical model that allows for the description of the I-V characteristics of a II-VI RTD. In this section we now use this model to briefly review the basic principles a voltage controlled spin filter based on a DMS RTD [Slob 03].

Let us consider a (Zn,Mn)Se quantum well RTD showing a magnetization according to the modified Brillouin function of reference [Gaj 79] and only the first confined state thereof. Applying an external magnetic field, the two fold degeneracy of the quantum well state is lifted. The spin splitting of the quantum well states given by equation 2.2 is plotted in fig. 2.17a. Each spin-split state in the quantum well results in a resonance-peak

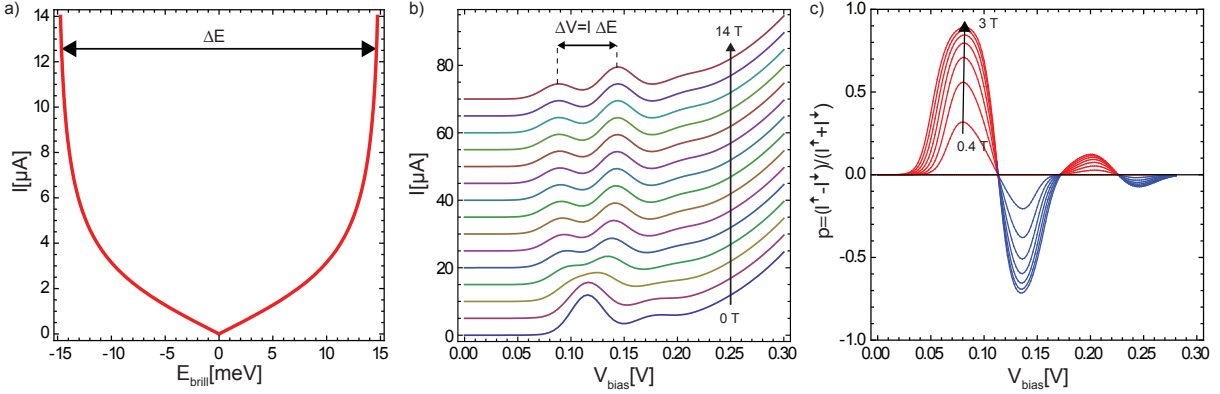


**Figure 2.17:** a) Plot of the modified Brillouin function used to simulate the splitting for the curves shown in b). b) Model I-V characteristics for magnetic fields from 0 to 14 T. The curves are offset by  $5\mu\text{A}$  for clarity. c) Current spin polarization for magnetic fields from 400 mT to 3 T. The two additional features at the higher bias voltages stem from the LO phonon replica peaks.

in the I-V characteristic of the DMS RTD. The resulting I-V characteristics for magnetic fields from 0 to 14 T are shown in fig. 2.17a, where an y-axis offset of  $5\mu\text{A}$  is used for clarity. At zero magnetic field, in the absence of splitting, the resulting I-V characteristic is shown as the bottom curve in fig. 2.17b. The second peak at approximately 180 mV and  $B=0$  T is a phonon replica due to the resonant tunneling process through the same quantum well state involving the excitation of a longitudinal optical (LO) phonon. As the degeneracy is lifted we thus see four resonance-peaks in total, two for each spin species. Each peak represents a current comprised of only one spin species and a sufficient splitting of the resonances will thus result in a spin polarized current through the RTD. The resulting spin polarization  $(I^\uparrow - I^\downarrow)/(I^\uparrow + I^\downarrow)$  is plotted as a function of the applied bias voltage in fig. 2.17c for various magnetic fields from 400 mT to 3 T. The filtering mechanism improves as the splitting of the spin states increases and the overlap of the spin-signals is reduced. The polarization however saturates for magnetic fields above 3 T due to the saturation of the spin-splitting in fig. 2.17a.

The maximum spin-down polarization (blue lines in fig. 2.17c) is lower than the maximum spin-up polarization (red lines), although the conductances for the two spin channels are assumed to be identical in this simple model. This is due to the increased contribution of the background current, which is not spin polarized and effectively reduces the overall spin polarization of the current traversing the RTD. The polarization at the second resonance is furthermore reduced by an overlap with the spin-up replica peak. Especially for samples containing 8% Mn, where the splitting is in the order of the LO replica energy, the spin-down resonance-peak and the spin-up replica-peak occur at comparable bias voltages at  $B \approx 6$  T. These two transport channels in parallel thus inject electrons of opposite spin types into the collector, further reducing the spin-filter efficiency for the spin-down operation mode.



---

In summary, given a sufficient splitting of the quantum well spin states, the latter act as two independent resonant transport channels, each occurring at a different bias voltage. One thus is able to switch from a spin-up polarized current to a spin-down polarized current by changing the voltage drop across the RTD to the respective setting. In the following chapter we present evidence that this picture however oversimplifies the transport properties of such a device and that some of the above made assumptions break down.



## Chapter 3

# Zero field spin polarization in a 2D paramagnetic resonant tunneling diode

In chapter 2 we established the theoretical framework for the description of the active region of an all II-VI semiconductor RTD. In this chapter this empirical model will be used to fit the I-V characteristics of a DMS RTD which acts as a voltage controlled spin filter [Slob 03]. Parts of this chapter are published in [Ruth 11].

The implementation of device components based on RTDs is one route towards the elaboration of a full semiconductor spintronics based technology scheme. While a ferromagnet/tunnel barrier spin injector [Croo 05, Jans 07, Pate 09] produces a fixed spin polarization for each given magnetization state, DMS can be used in II-VI semiconductor RTDs to implement spin selective tunneling at different bias voltages [Slob 03]. A caveat to this approach has been the paramagnetic nature of bulk (Zn,Mn)Se, which makes the application of an external magnetic field necessary for spin filter operation. This can be overcome by using the 0D states of self assembled quantum dots embedded in a DMS host material, since the microscopic magnetic environment of a dot allows for the formation of BMP-like states which lift the spin degeneracy for the tunneling electrons [Diet 82, Goul 06]. Such self assembled quantum dot structures have a rich resonance spectrum which typically occur over a broad range of bias voltages, limiting the controllability of device characteristics. Here we show that similar zero field splitting can be achieved in the much more reliable quantum well geometry. RTDs containing self-assembled quantum dots will be further discussed in chapters 6, 7 and 8.

We investigate an all-II-VI RTD grown on a GaAs substrate. The active RTD region contains a 9 nm  $\text{Zn}_{0.96}\text{Mn}_{0.04}\text{Se}$  quantum well layer sandwiched between two 5 nm  $\text{Zn}_{0.7}\text{Be}_{0.3}\text{Se}$  tunnel barriers (device A). Proper contact layers are applied on each side of this structure to allow for measurements of transport through the layer stack (fig. 3.1). The quantum well layer is made from a DMS that exhibits giant Zeeman splitting in an external magnetic field, which is described by a modified Brillouin function

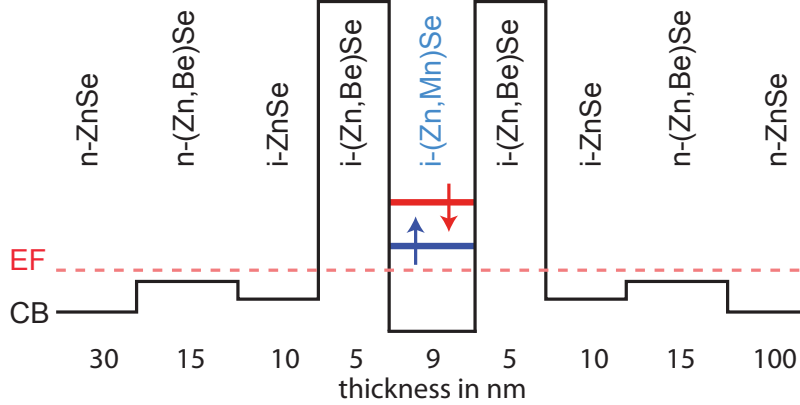


**Figure 3.1:** Schematic conduction band profile of the resonant tunneling diode at zero bias, with lifted spin degeneracy in the quantum well.

[Twar 84, Slob 03] with a pair breaking contribution at high magnetic fields [Shap 84]. Lifting the degeneracy of the quantum well spin states with an external magnetic field allows the RTD to be used as a voltage controlled spin filter [Slob 03]. The I-V characteristic shows current peaks at two different bias voltages as long as the splitting is large enough to resolve the separate spin up and down resonances.

The black lines in fig. 3.2 (device A) show I-V characteristics for measurements at 1.3 K from 0 to 14 T. Figure 3.3 shows experimental data for a second type of sample (device B) with 8% Mn and layers that are 6% thinner than for device A. Due to the high Mn content of device B, the spin down resonance is merged with the spin up replica peak at high magnetic fields. Thus the polarization analysis shown in fig. 3.9 will focus on device A.

Similar results for fields up to 6 T have previously been successfully described [Slob 03] using a model based on taking the conductance of a single spin channel to be one half of the  $B=0$  T curve, applying Brillouin splitting to the quantum well levels and recombining the contribution of the two spin channels into a total I-V curve by using Kirchhoff's laws. Such a model implicitly assumes spin degeneracy at  $B=0$  T, and obviously breaks down if that condition is not fulfilled. The data presented here, which includes higher magnetic fields than available previously, suggests that a modified picture of the zero-field tunneling process is necessary.

As shown by the blue lines in fig. 3.2 the data is suggestive of the peak splitting not vanishing at  $B=0$  T. More importantly, the peak in the zero field I-V characteristic is also less symmetric than each of the split peaks at high magnetic fields, and the resonance in the zero field curve is much broader than that of the individual resonances in the 14 T curve. Both the asymmetry and the increased width of the peak in the  $B=0$  T curve may be a consequence of this peak actually being comprised of two resonances occurring at somewhat different bias voltages. These considerations indicate the need for a different modeling scheme.

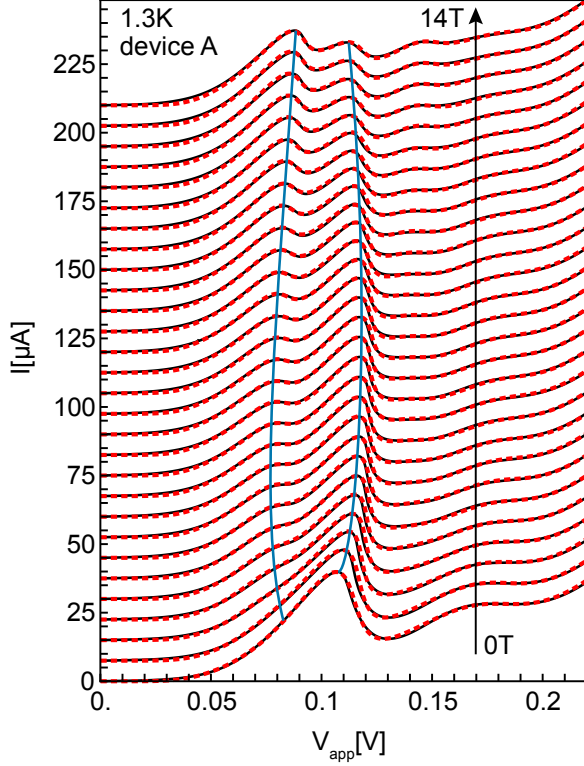


**Figure 3.2:** (Device A) Fits (red dashed curves) to the I-V characteristics (black) at 1.3 K and at magnetic fields from 0 to 14 T, applied perpendicular to the layer stack. Each curve is offset by  $14 \mu\text{A}$  on the current axis for clarity. The blue lines are a guide to the eye to emphasize the apparent peak splitting at  $B=0$  T.

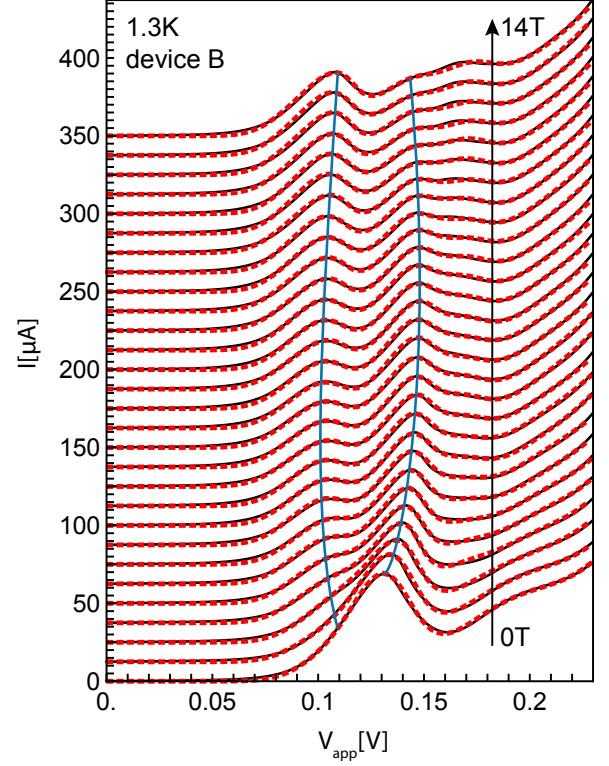


**Figure 3.3:** (Device B) I-V characteristics (black lines) and fits (red dots) of a sample with 8% Mn and 6% thinner layers at magnetic fields from 0 to 14 T (in steps of 0.5 T) and  $T=1.3$  K. Each curve is offset by  $14 \mu\text{A}$  on the current axis for clarity.

Bottom-up approaches to modeling such data have been reported [Egue 98, Havu 05, Saff 05, Bele 05, Li 06, Rado 06, Qiu 08, Saff 09, Wang 09], but these typically treat an idealized system ignoring considerations such as contact resistances. In fig. 3.4 we show that such considerations are important. Figure 3.4a gives the equivalent circuit of our real device in the two channel model, and includes magnetic field dependent contact resistances  $R_s^{\uparrow,\downarrow}$ , an interface scattering term  $R_{scat}$  and a non resonant contribution to the tunneling current,  $R_{bg}$ . The active region of the RTD is represented by the two diodes, one for each spin channel, and each with a voltage and magnetic field dependent resistance  $R_{bg}$  in parallel. While the diode carries the resonant part of the current including the LO-phonon replica contributions, the background current through  $R_{bg}$  accounts for electrons tunneling off resonance through the double barrier region.

To obtain an expression for the highly non-linear resistance resulting from the resonant tunneling transport, one normally assumes a Lorentzian shaped transmission at the

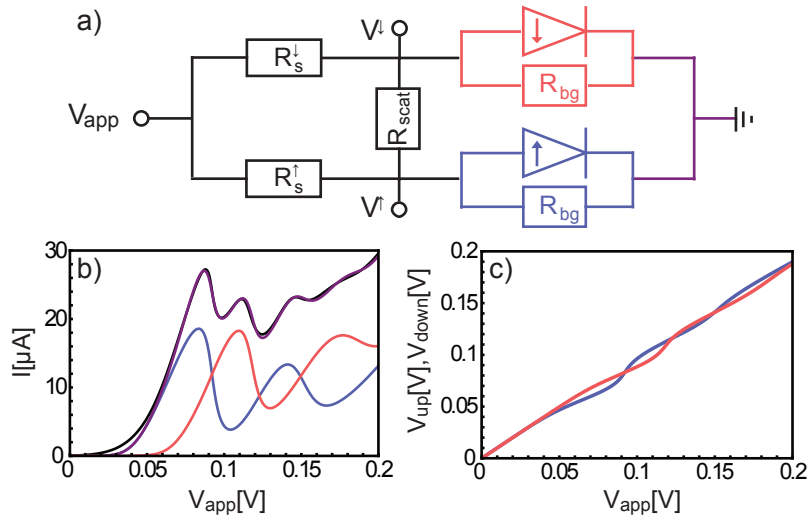


**Figure 3.4:** a) Resistor model for the two spin RTDs in parallel. b) Measurement and fit for the 14 T I-V characteristic (device A). The blue and red curves represent the current carried by the spin up and down species, adding up to the purple curve which is the fit to the measurement (black curve). c) Plot of the potentials  $V^\uparrow$  and  $V^\downarrow$  at each spin diode as a function of the applied bias voltage.

resonance condition. As discussed in chapter 2 of this thesis, the peaks in our experiment show a Gaussian line shape with a bandwidth much broader than the expected injector Fermi energy (multiplied by the lever arm). Thus an additional broadening mechanism dominates the resonance width.

In fig. 3.5 we plot the  $B=0$  T I-V characteristics of 40 mK (black line), 1.3 K (blue dots) and 15 K (red dots), showing that in the absence of magnetic field, temperature does not have any influence on the I-V characteristic. This indicates that a much stronger broadening mechanism is at work in the device, probably stemming from imperfect interfaces at the active RTD region. Local potential fluctuations, caused by well width fluctuations [Zren 94] or inhomogeneous alloy or doping concentrations [Maka 10], impose an additional in-plane confinement for tunneling electrons thus creating 0D type tunneling states, so called interface quantum dots [Gamm 96, Cate 92, Sale 93]. Since our device is  $100^2 \mu\text{m}^2$  and these fluctuations are typically on a nm scale, we sample over an ensemble of these states in our vertical transport measurements. One can view this configuration as a large number of 0D resonant tunneling diodes in parallel, each with its own resonance condition. This results in a broadened Gaussian line shape [Zren 94] for the overall resonant conductance feature.

The LO-phonon replica are described by additionally broadened Gaussian conductance peaks with reduced amplitudes and an energetic separation from their respective spin-split resonance peaks of 31.7 meV, the LO phonon energy of bulk ZnSe [Land 99].

For the non-resonant background current we use the transfer matrix model discussed in section 2.7 consisting of two tilted barriers where the quantum well was omitted in

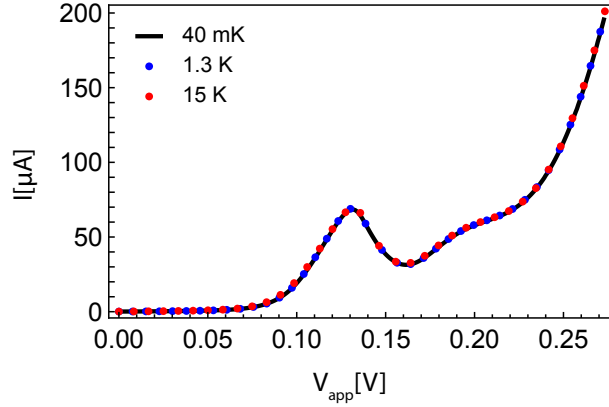


**Figure 3.5:** (Device B) Comparison of I-V characteristics at  $T = 40$  mK, 1.3 K and 15 K. The resonance does not sharpen at low temperatures.

order to remove resonant contributions. The potential drop over the quantum well region, which effectively lowers the second barrier, plays an important role, and is explicitly taken into account. The resulting transmission is proportional to the non-resonant tunneling of emitter electrons and fits well to the measurement at high bias voltage, where the contribution of resonant tunneling is small.

Due to the contact resistances  $R_s^{\uparrow,\downarrow}$ , the two voltage nodes  $V_{\uparrow}$  and  $V_{\downarrow}$  in fig. 3.4a are not necessarily at equipotential for a given applied bias voltage  $V_{app}$ . Figure 3.4c shows the potential at the points  $V_{\uparrow}$  and  $V_{\downarrow}$  as a function of  $V_{app}$ . When a resonance condition is reached for either of the spin diodes, the resistance of that spin diode drops and the potentials across each of the diodes is altered accordingly. While we have experimental access to  $V_{app}$ , the transport theory for resonant tunneling only describes the active region of the device. Thus considering the contact resistances is vital for fitting any RTD model to actual experiments. As an example, the resulting fits for a magnetic field of 14 T are presented in fig. 3.4b where contributions from both the spin up and down channels are shown as well as how they add up to produce a fit (purple curve) to the observed measurement (black curve). While the conductance of a resonant channel is perfectly symmetric on an energy scale, fig. 3.4 and 3.6 show how in a real device, the contact resistances influence the shape of the resulting  $I$ - $V_{app}$  characteristics.

As is clear from the circuit diagram in fig. 3.4a, the total current traversing the device is given by

$$I(V_{app}) = V^{\uparrow} \left( \sigma^{\uparrow}(V^{\uparrow}) + \sigma_{LO}^{\uparrow}(V^{\uparrow}) + \sigma_{bg}^{\uparrow}(V^{\uparrow}) \right) + V^{\downarrow} \left( \sigma^{\downarrow}(V^{\downarrow}) + \sigma_{LO}^{\downarrow}(V^{\downarrow}) + \sigma_{bg}^{\downarrow}(V^{\downarrow}) \right) \quad (3.1)$$

$$\text{with } \sigma^{\uparrow,\downarrow}(V^{\uparrow,\downarrow}) \propto p^{\uparrow,\downarrow} \cdot \exp \left( \frac{(l(E - E_0^{\uparrow,\downarrow}))^2}{2\Gamma^{\uparrow,\downarrow 2}} \right) \quad (3.2)$$

where  $\sigma^{\uparrow,\downarrow}$ ,  $\sigma_{bg}^{\uparrow,\downarrow}$  and  $\sigma_{LO}^{\uparrow,\downarrow}$  are the conductances for the spin channels, the background contributions and the LO-phonon replica peaks respectively.  $l$  is the lever arm linking the energy scale in the quantum well to the diode bias voltages  $V^{\uparrow,\downarrow}$ ,  $E_0^{\uparrow,\downarrow}$  is the energy between the spin levels and the conduction band edge,  $p^{\uparrow,\downarrow}$  are fitting parameters for the amplitudes of the spin conductances (and thus yield the spin polarization) and  $\Gamma^{\uparrow,\downarrow}$  are the variances of the Gaussians describing the energy level distribution for the spin channels. Equation 3.2 is also used for  $\sigma_{LO}^{\uparrow,\downarrow}$  but with different variances  $\Gamma_{LO}^{\uparrow,\downarrow}$ , amplitudes  $p_{LO}^{\uparrow,\downarrow}$  and  $E_{0,LO}^{\uparrow,\downarrow} = E_0^{\uparrow,\downarrow} + 31.7$  meV.

Our detailed model therefore consists of solving the equivalent circuit of fig. 3.4a for an RTD with a spin split resonance and the associate LO-phonon replica. For each applied bias voltage, we use a Newton Method to solve the following set of equations

$$V_s^\uparrow + V^\uparrow = V_{app} \quad (3.3a)$$

$$V_s^\downarrow + V^\downarrow = V_{app} \quad (3.3b)$$

$$V_s^\uparrow/R_s^\uparrow + V_s^\downarrow/R_s^\downarrow = V^\uparrow/R^\uparrow[V^\uparrow] + V^\downarrow/R^\downarrow[V^\downarrow] \quad (3.3c)$$

$$(V_s^\uparrow/R_s^\uparrow - V^\uparrow/R^\uparrow[V^\uparrow])R_{scat} = V_s^\downarrow - V_s^\uparrow \quad (3.3d)$$

with the boundary condition that the set of  $V_s^\uparrow$ ,  $V_s^\downarrow$ ,  $V^\uparrow$ ,  $V^\downarrow$  and  $V_{scat}$  be consistent with the applied bias voltage.

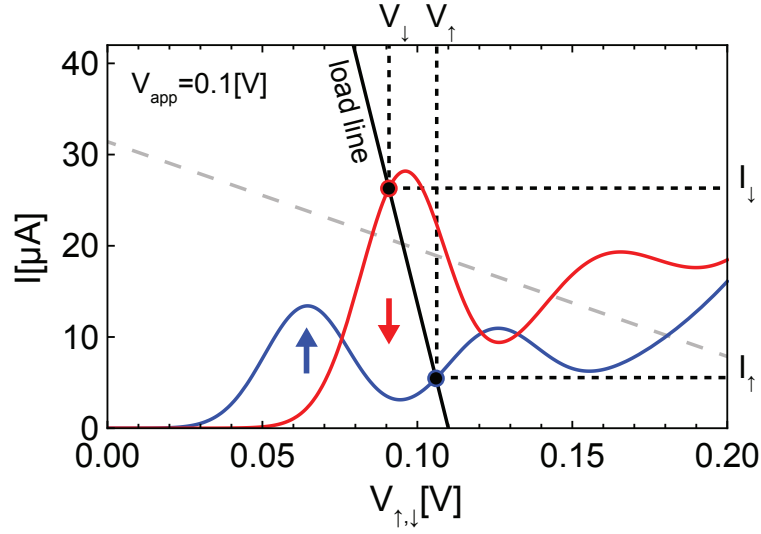
This equation set does not yield an analytical solution for our non-linear circuit components as the resistance of both RTDs are a function of the voltages  $V^\uparrow$  and  $V^\downarrow$  dropping over these RTDs.

Figure 3.6 shows a graphical representation of this problem in a load line analysis. The load line indicates the current flowing through the contact resistance as a function of the RTD bias voltages and under the simplifying assumption of infinite scattering resistance  $R_{scat}$  the intersection points of this load line with the spin-up and spin-down I-V curves yields the solution to equations (3.3).

To evaluate the impact of assuming  $R_{scat} \rightarrow \infty$  the markers indicating the intersection points in fig. 3.6 are solved for numerically allowing for finite  $R_{scat}$ . As is readily apparent from the figure the agreement is quite good allowing fig. 3.6 to be used as a useful intuitive guide at intermediate to high fields. The discrepancy between the simplified picture and the exact numerical solution becomes worse at low fields. Throughout this chapter the full numerical solution is used in all analysis.

This intuitive picture clearly illustrates the importance of contact resistance in such a device. A large contact resistance (compared to the internal device resistance) would significantly reduce the slope of the load line (dashed gray line in fig. 3.6). Then due to the negative differential resistance of the RTDs, the circuit has multiple possible operation points, and is thus unstable making it impossible to access all regions of the diode  $I^{\uparrow,\downarrow}$ - $V^{\uparrow,\downarrow}$  characteristics within the measurement of  $(I^\uparrow + I^\downarrow)$ - $V_{app}$ . Furthermore since the measurement of the device necessarily includes a contact resistance, the recorded signal is stretched and deformed compared to the intrinsic diode characteristics.





**Figure 3.6:** Example for an applied bias of 0.1 V and  $B=6.5$  T. Due to the contact resistance in the model, both spin channels are able to operate at different diode bias voltages. A load line analysis depicts the current flowing through the contact resistance is plotted on the axis of the diode voltage. The gray dashed line represents an increased series resistance that would result in an unstable circuit.

For an RTD that does not discriminate between spin-up and spin-down electrons, one can simply convert the measurement back to the intrinsic scale using

$$V_d = V_m - I_d R_s \quad (3.4)$$

where  $V_m$  is the measured voltage across the device,  $I_d$  is the current flowing through the diode and  $R_s$  is the contact resistance. This procedure is not valid for an RTD with separated transport channels as depicted in fig. 3.4 because there is no experimental access to the voltage of each separate spin channel excluding contacts. The effect of the contact resistance combined with the non-linearity of the channels means that the operating voltage of the two channels is different, an effect which is especially important in the regions near the resonances. A more thorough analysis is therefore needed as the line shape of the individual channels cannot be directly inferred from the measurements.

Since the zero field I-V characteristic is a superposition of two strongly overlapping peaks, the best starting point for the fits is the high magnetic field data, where one easily can find the proper variances  $\Gamma^{\uparrow,\downarrow}$  and  $\Gamma_{LO}^{\uparrow,\downarrow}$  of the resonant peaks and LO-phonon replicas. Starting at 14 T, the I-V characteristic for each magnetic field is fitted by adjusting  $p^{\uparrow,\downarrow}$ ,  $p_{LO}^{\uparrow,\downarrow}$  and  $E_0^{\uparrow,\downarrow}$ . We also allow for a magneto-resistance effect in the contacts  $R_s^{\uparrow,\downarrow}$  and in the scattering channel  $R_{scat}$ . By including a magnetic field dependence of  $\Gamma_{LO}^{\uparrow,\downarrow}$ , we account for the small, experimentally observed field dependent broadening of the replica peaks.

The resulting fits are shown as red dashed lines on top of the I-V characteristics in fig.

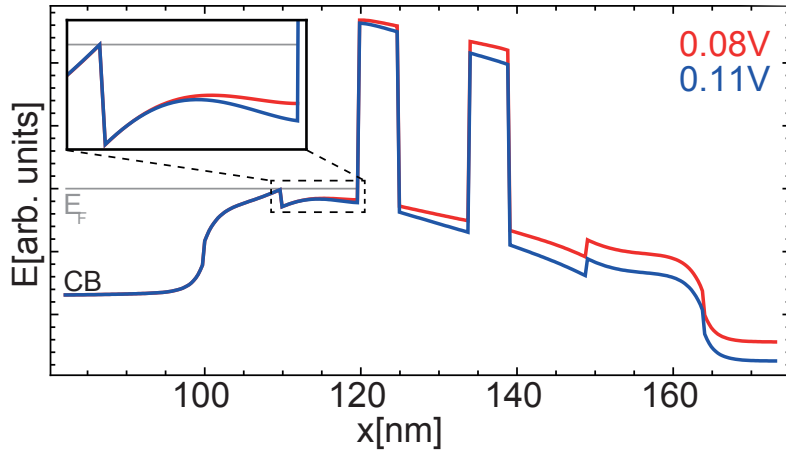


**Figure 3.7:** Self consistent conduction band profile of the resonant tunneling diode at the approximate resonance biases (device A). The inset shows the increase of tunneling states due to the applied bias voltage.

3.2, while in fig. 3.4b the contributions of spin-up and spin-down electrons to the 14 T I-V characteristic are illustrated. One would a priori expect a Brillouin function to describe the magnetic field dependence of the splitting [Slob 03]. The measurements shown in fig. 3.2 (device A) and 3.3 (device B) exhibit a very different behavior. At low magnetic fields we observe that instead of a spin degeneracy, the  $I-V_{app}$  characteristic is properly fit only by allowing for finite splitting even at zero magnetic field. We have previously observed such a remanent zero field splitting in the zero dimensional resonant tunneling states of self assembled CdSe quantum dots [Goul 06]. Here the quantum well is nominally a two dimensional object. As previously discussed, however, various inhomogeneities cause the current transport to be effectively mediated by a large ensemble of parallel paths each flowing in a local environment. The relatively low number of magnetic atoms influenced by each of these regions means that each will statistically have, on average, a net magnetization at zero field [Diet 82, Diet 86]. This effect is further enhanced by the presence of the spin of the tunneling electron [Diet 83].

The energy separation between spin-up and spin-down peaks is 15 meV at  $B=0$  T as determined by the fit. This energy is not necessarily the same as the splitting of the two spin states. As the measurement is always referred to the conduction band of the emitter, this energy difference is influenced by the different bias conditions needed to align each spin state to the emitter. Figure 3.7 shows self-consistent calculations of the conduction band profile at the resonance conditions for device B. As the inset shows, the Fermi energies differ by approximately 20% for the two resonance conditions. Since the maximum current flows when the quantum well level is aligned with the conduction band edge and is proportional to the cross-sectional plane  $A = \pi k_F^2$  of the emitter Fermi sphere at constant  $E_z$  this would result in a  $\approx 44\%$  change of the peak amplitudes.

The first peak at lower bias voltage is suppressed while the second peak is enhanced

in the B=0 T I- $V_{app}$  characteristic. For a small energetic splitting in the resonant state, one would expect similar conductances for the two transport channels. A change in the confinement caused by the splitting will influence the amount of leakage of the quantum well wave function into the emitter, while for each  $V_{app}$  the resulting change in symmetry of the double barrier will affect the transmission [Ricc 84, Butt 88, Lury 89, Alle 94, Miya 98]. A higher bias voltage will also drive more current at the same conductance. From transfer matrix calculations for the transmission probabilities of the double barrier we however conclude that different biasing conditions alone cannot explain the magnitude of the effect on the amplitudes of the B=0 T spin currents.

While the peak positions stay constant at intermediate fields because the Brillouin function saturates, above 8 T there is a clear reduction in the splitting of the peaks on the bias voltage axis. A reason for this reduction is likely the Zeeman splitting of the emitter electrons, since both ZnSe and (Zn,Mn)Se have a positive g-factor and the resulting splitting  $\Delta V_{res}$  on the voltage axis is given by  $\Delta V_{res} = l(g_{QW} - g_E)\mu_B$ , where  $l$  is the lever arm of the device and  $g_{QW}$  and  $g_E$  are the effective g-factors of the ZnSe emitter and the quantum well electron states respectively. From the fits we obtain a slope of 0.24 meV/T (-0.17 meV/T) for the spin-up (down) peak. The corresponding g-factors are  $g_{\uparrow} = 8.2$  and  $g_{\downarrow} = 5.7$ , far greater than the bulk ZnSe value of 1.1 [Land 99]. Possible explanations for this increase in magnetic response include that tunneling electrons at the interface to the barrier cannot be treated in the free electron picture of a parabolic s-type conduction band, that there is a dilute Mn concentration in the emitter due to diffusion during growth, or that the energetic distance to the resonant quantum well state is altered by spin selective band bending of the emitter. The peak amplitudes are also strongly magnetic field dependent. The asymmetry of the effective g-factors for the emitter polarization suggests an effect that is linked to the resonance bias conditions. The two peaks occur at different bias voltages and therefore have different conduction band bending conditions. This bending changes the number of available electronic states for resonant tunneling, strongly influencing tunneling currents. This factor can easily surpass the effect of Zeeman splitting. The resulting effective g-factors are therefore not purely a result of the electron spin interacting with the magnetic field but also of the feedback mechanisms induced by changes in the potential landscape (as shown in fig. 3.7). Different transmittances of the spin channels may also result in spin sensitive charge build-up in front of the barrier that can influence not only the amount of available states in front of the barrier, but also the bias voltage needed to attain the resonance conditions [Choi 92].

For an I-V characteristic consisting of a spin-up and spin-down resonance, a peak movement may very well be caused by a change in line shape of one of the peaks due to their superposition. Therefore we now consider the effect of temperature dependence, by analyzing data taken at 6 T for various temperatures ranging from 45 mK to 15 K. For each temperature Temp one can solve the equation

$$\text{Brillouin}[6 \text{ T}, \text{Temp}] = \text{Brillouin}[B_{eff}, 1.3 \text{ K}]$$

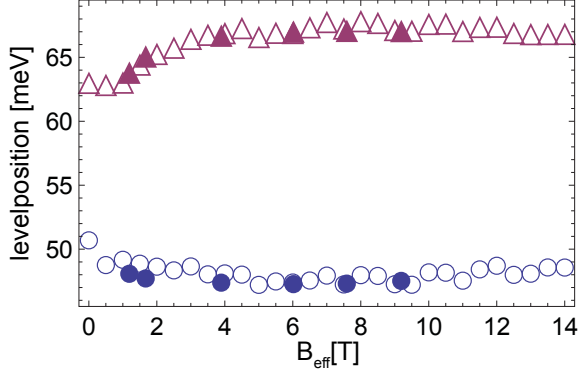


**Figure 3.8:** Energetic distance to the conduction band of spin up (circles) and down (triangles) levels in the quantum well. Filled symbols show results from fits at various temperatures at  $B=6$  T, while empty symbols show fits at various magnetic fields at  $T=1.3$  K.

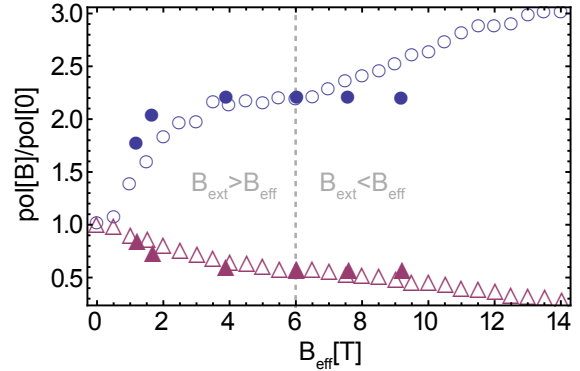


**Figure 3.9:** Change in amplitudes of the spin up (circles) and down (triangles) levels with applied external magnetic field (normalized to the  $B=0$  T amplitudes). Filled symbols show results from fits at various temperatures at  $B=6$  T, while empty symbols show fits at various magnetic fields at  $T=1.3$  K.

to determine at which magnetic field  $B_{eff}$  a curve from the 1.3 K dataset has the same level splitting in the quantum well as the 6 T curve at the given temperature. Figure 3.8 presents the level positions of the resonant spin states for both the 1.3 K data set of fig. 3.3 and this temperature dependent measurement. The open symbols are for the 1.3 K dataset, and the x-axis is then directly the magnetic field at which the measurement was performed. The solid symbols are for the temperature dependent data, plotted against  $B_{eff}$  as described above. This comparison confirms that the movement of the peak position is a result of changes in the band diagram, and not a result of any deformation of peak shape, as these would not be stable under the different environmental conditions.

A similar analysis also is conducted for the amplitudes of the spin channel conductances in fig. 3.9. The polarization values acquired from fits to measurements at various temperatures differ from those acquired from the magnetic field dependent measurements at  $T=1.3$  K. After correcting for the level splitting using  $B_{eff}$ , the only visible difference between the two sets of measurements are peak amplitudes. This is because a constant quantum well splitting is maintained in the two configurations, which then only differ in emitter polarization due to the applied external magnetic field. Figure 3.9 shows that indeed, the only field where both polarization values are identical, is at  $B_{eff}=6$  T, where both temperatures are the same. For  $B_{eff} < 6$  T the temperature measurements show higher polarization since, while the splitting in the quantum well is maintained constant, the external magnetic field effect on polarizing the emitter produces a higher polarization of the spin current. The opposite is true for  $B_{eff} > 6$  T. The results of fig. 3.9 thus suggest that both the splitting in the quantum well and the polarization of the emitter influence the spin polarization of the resonant current. For  $B_{eff} > 6$  T when the splitting of the Brillouin function saturates, the only effect left should be the polarization of the

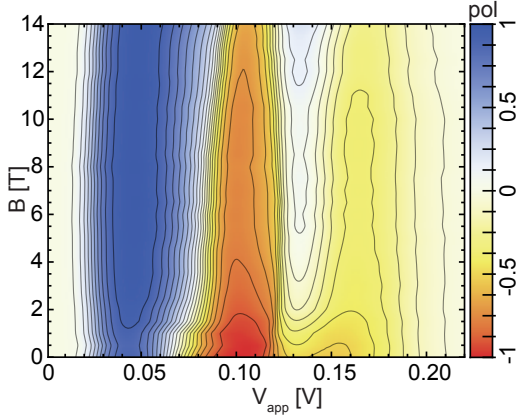


**Figure 3.10:** (Device A) Current spin polarization as a function of applied bias voltage and magnetic field.

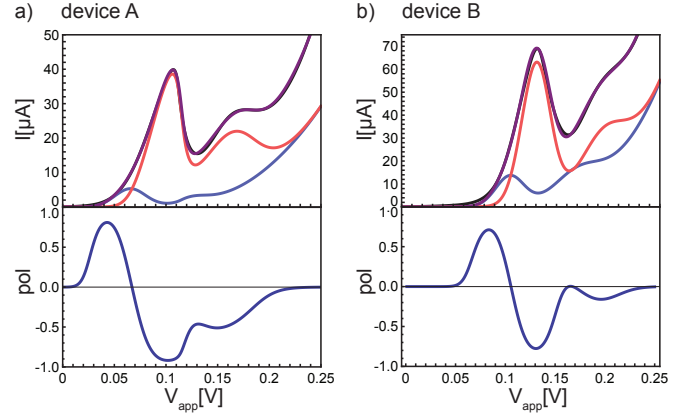


**Figure 3.11:** Also the control sample is highly suggestive of zero field splitting. The I-V characteristic (black line) is fitted (purple line) by adding the spin up (blue line) and down (red line) currents.

emitter electrons. The polarization for different temperatures therefore saturates, since the external field is also kept constant. The magnetic field sweeps at constant temperature of 1.3 K show a linear increase / decrease above  $B_{eff}=6$  T of different slopes which is the additional feedback of the emitter and is in agreement to the different effective g-factors for the high magnetic field response as presented earlier in this paper.

The amplitudes  $p^{\uparrow\downarrow}$  we obtain from the above fitting process give quantitative results for the spin polarized currents. To use this device as a detector for the emitter spin polarization one would need to link the emitter polarization to the amplitude of the traversing spin currents. The increased and asymmetric magnetic feedback that is evidenced by the movement of the spin peaks suggests that other effects in addition to pure Zeeman splitting of the emitter are involved. Therefore usage as a detector for the emitter spin polarization is difficult. Within our model it is possible to evaluate currents for spin-up and down electrons separately, thus allowing for a quantitative analysis of the polarization of the current traversing the device. Figure 3.10 shows the current spin polarization as a function of magnetic field and bias voltage. Blue (red) indicates spin up (down) polarization of the current. The non-resonant background current is not spin selective and therefore the current polarization  $P_c$  plotted in fig 3.10 is given by

$$P_c = \frac{I_{\uparrow} - I_{\downarrow}}{I_{\uparrow} + I_{\downarrow} + I_{bg(\uparrow+\downarrow)}} \quad (3.5)$$

The splitting of the spin levels in the external magnetic field and the changes in the amplitudes of the resonant peaks lead to a polarization above 90% (device A) for the spin-up peak at  $B=14$  T, while the spin-down peak polarization decreases to below 60%. While a high degree of polarization of both spin types can be achieved at all measured magnetic fields, counterintuitively, despite the paramagnetic nature of bulk (Zn,Mn)Se,

the maximum polarization efficiency is achieved without applying an external magnetic field. For device A a polarization of 80% for spin-up and 90% for spin-down is observed, as evidenced by the I-V curve of the two channels for  $B=0$  T presented in fig. 3.11, where also the similar results for device B are displayed.

In summary, we have shown high spin polarizations can be achieved due to formation of BMP like states in the active RTD region. The resulting microscopic magnetization for the tunneling electrons lifts the spin degeneracy and provides two separate transport channels. Feedback mechanisms stemming from the influence of different biasing conditions both increase the energy splitting of the peaks and influence their amplitudes, resulting in high degrees of current spin polarization. Our model allows for good fits to the device characteristics and thus quantitative analysis of the polarization. Not only does this model confirm the findings of reference [Slob 03] that the device can work as a voltage controlled spin filter at moderate magnetic fields, but it also establishes that the local spin polarization efficiency not only remains, but is even enhanced in the absence of a magnetic field.

## Chapter 4

# 0D interface states in a DMS resonant tunneling diode

In a joint project with my colleagues Philip Hartmann and Steffen Bieker, the impact of a process which removes the GaAs substrate from a pre-patterned II-VI semiconductor device is examined. A combined mechanical polishing and selective chemical etching process is used to lift the MBE grown II-VI semiconductor material from its substrate. This procedure is presented in [Biek 10] and is thus not discussed in this thesis. We also note that purely chemical methods of lifting II-VI heterostructures of a GaAs substrate using MgS [Brad 05] and ZnMgSSe [Moug 09] as release layers have also been demonstrated.

DMS RTDs similar to the one discussed in chapter 3 were chosen for preliminary testing of this method. As the properties of a resonance-peak in the I-V characteristic of an RTD are a measure of the heterostructure layer quality, transport measurements can

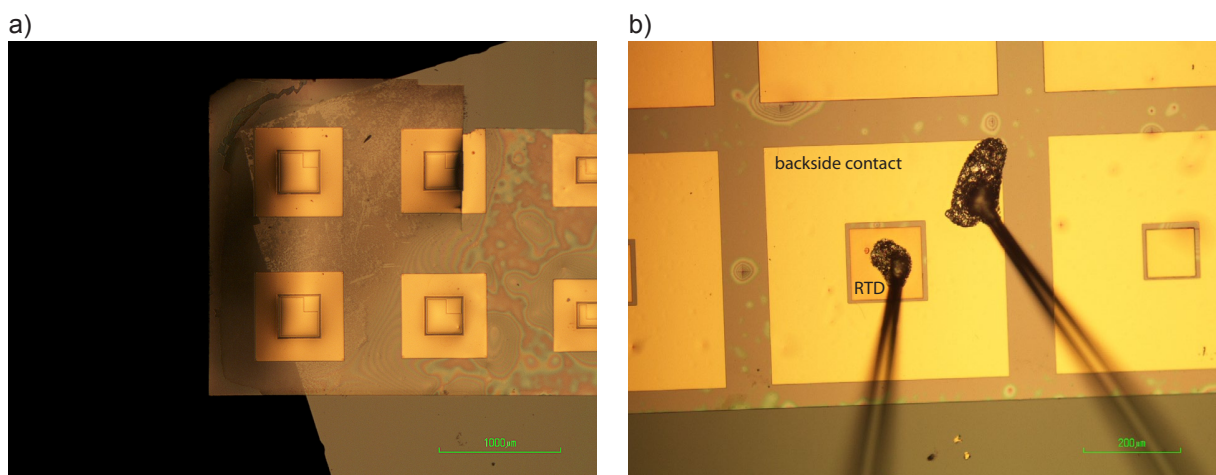


**Figure 4.1:** Images by courtesy of P. Hartmann. a) A lifted layer resting on the corner of a piece of silicon wafer. The stiffness of the lifted layer evidences its continuous structural integrity after removal of the MBE substrate. b) The fragile lifted layers are soft-bonded by a conductive adhesive, as they do not withstand the stress imposed by standard bonding routines.

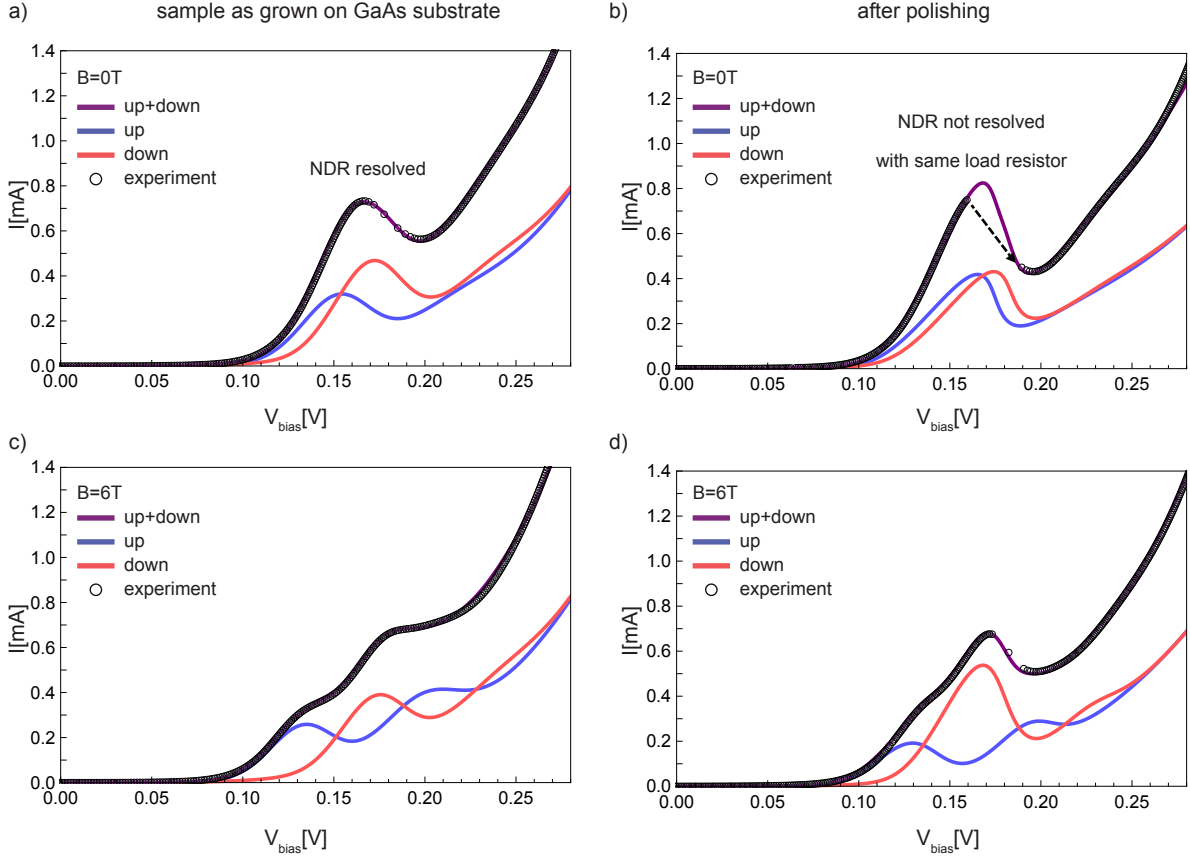


**Figure 4.2:** I-V characteristics of a dilute magnetic quantum well RTD, before and after polishing at  $B=0$  T and  $B=6$  T

be used to examine potential damages to the lifted layers. Here we investigate transport measurements on such a lifted DMS quantum well RTD.

Figure 4.1a shows a lifted II-VI heterostructure with pre-patterned RTD mesas, overlapping with the edge of a Silicon wafer which is used as a carrier material after removing the substrate. The intact crystalline structure is evidenced by the apparent stiffness of the lifted layer. As a result of the thinning process, the fragile II-VI heterostructures do however not withstand the stress from standard wire bonding routines. Instead, small droplets of an electrically conductive adhesive are applied to the contact pads of the RTD pillars. Figure 4.1b shows this contacting scheme for a single RTD pillar on a lifted layer.

Being subjected to mechanical stress during the polishing procedure, samples were expected to degrade in crystalline quality, even though special care is taken prior to the mechanical polishing to prevent damages to the II-VI heterostructure [Biek 10]. Comparing transport measurements on a standard DMS RTD to those on a nominally identical layer stack that was lifted from the MBE substrate, we however find a contrary behavior.

We investigate a standard II-VI DMS RTD grown on a GaAs substrate. The active region of the device is comprised of a  $\text{Zn}_{0.92}\text{Mn}_{0.8}\text{Se}$  quantum well sandwiched between



two 5.5 nm thick  $\text{Zn}_{0.8}\text{Be}_{0.2}\text{Se}$  tunnel barriers. The patterning of the RTD mesas is done prior to the polishing process in the same manner as for the devices presented in chapter 3.

Figures 4.2a+c show I-V characteristics of an RTD which is still connected to its GaAs substrate. As discussed in chapter 3, due to the remanent zero field splitting in these devices, the best starting point for a proper set of fitting parameters is a magnetic field that results in a sufficient splitting of the two spin-selective transport channels. Figure 4.2c plot the I-V characteristic at a magnetic field of  $B=6$  T, applied perpendicular to the layer stack. The experimental data (black circles) is fitted using two Gaussian conductance peaks of variance  $\Gamma_0 = 8.9$  meV. The blue and red lines depict the contributions to the total current (purple line) of the spin-up and down channels, respectively. These findings are then used as fixed parameters while fitting the I-V characteristic at  $B=0$  T in fig. 4.2a. As for the devices discussed in chapter 3, the data is suggestive of a remanent zero field splitting of the two resonance-peaks.

A second sample of same pillar size from the identical layer stack is characterized after removal of the GaAs substrate. For a proper comparison, we use the identical measurement setup for the characterization as for the first sample. The current through each RTD is measured with a load resistor of  $R=6 \Omega$  in series to the device. Figure 4.2b shows the I-V characteristic at  $B=0$  T of the lifted RTD. The region of negative differential resistance (NDR) cannot be completely accessed by the measurement as evidenced by the jump (depicted by the dashed arrow) in the measured bias voltage. Vertical jumps (large reduction of the measured current  $I$  for a very small increase of  $V_{bias}$ ) occur due to intrinsic properties of the RTD [Shea 88, Fost 89, Lury 89]. A sudden jump in the measured bias voltage as seen in fig. 4.2b however indicates a bistability in the measurement circuit. Such a problem arises if the load resistance is too high with respect to the device resistance [Fost 89, Ruth 08a]. That this kind of bistability occurs only after removing the substrate shows that the on-peak resistance of the device is reduced by this procedure. As the same load resistance as well as the same RTD pillar size is used for both measurements, we conclude that the apparent changes stem from an enhancement of the resonance after lifting the II-VI layer stack from the GaAs substrate. More importantly, the bistability vanishes in the I-V characteristic of the lifted layer at  $B=6$  T as is shown in fig. 4.2d. Due to the increased splitting of the resonance-peaks at  $B=6$  T, the on-resonance resistance is slightly larger than at  $B=0$  T and the measurement is now able to access the NDR region.

We again use the same model as in fig. 4.2a+c to fit the I-V characteristics at  $B=6$  T and  $B=0$  T, and find a reduced peak variance of  $\Gamma_p = 8.2$  meV. In addition to an increased fidelity of the resonance, we find a reduction of the apparent remanent zero field splitting for the I-V characteristics in fig. 4.2b. Furthermore, as is clear from comparing fig. 4.2b+d to fig. 4.2a+c, the non-resonant background current is reduced for the lifted layers. All these findings indicate an increase in the layer quality of the heterostructure. Figure 4.3a depicts a patterned RTD pillar on a GaAs substrate. The rough interface between the quantum well layers and the tunnel barriers result in an additional in-plane confinement

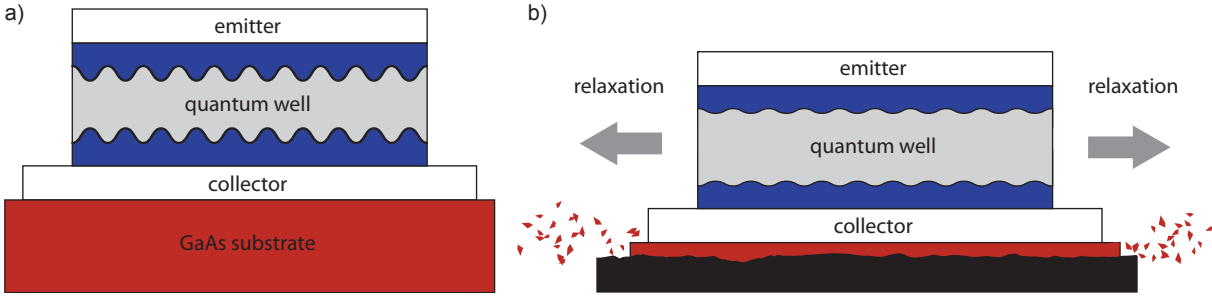


**Figure 4.3:** a) Schematic of the strained layer stack after growth on a GaAs substrate. Imperfect interfaces result in broadening of the observed resonances in the RTD I-V characteristics. b) Layer quality improves after removal of the substrate, reducing the observed zero field splitting as well as the variance of the bell-shaped peak.

allowing for the formation of BMP states at the interface. While this roughness governs the broadening of the resonance, it at the same time allows for the magnetic ordering at the interface.

In the MBE growth of all II-VI heterostructures on GaAs substrate, the lot of the material grown is not perfectly lattice matched to the substrate. The resulting strain build up sets an upper limit for the total layer stack thickness and is also likely to influence the layer quality of II-VI RTDs. Removing the substrate, this build-up strain is relaxed as is schematically shown in fig. 4.3b. Stemming from the interface roughness, the additional in-plane confinement is also diminished, weakening the BMP like states at the quantum well interfaces. Such a reduction of the average BMP energy is consistent with the observed reduction in the zero-field splitting of the resonance-peaks in fig. 4.2b. The reduced splitting at the same time results in an increased overlap of the spin-up and spin-down resonance-peaks. The resulting superimposed I-V characteristic shows a sharper resonance-peak which ultimately results in the observed bistability in fig. 4.2b.

A strong potential roughness will also introduce weak spots in the barriers. These weak spots dominate transport as the tunneling probability shows an exponential dependence on the barrier thickness. Flattening the tunnel barrier layer will increase the tunnel barrier thickness at these weak spots, thus increasing the overall tunnel barrier quality. Hence we conclude that the reduction in the background current for the lifted RTDs is also consistent with our model picture in fig. 4.2.

While the remanent zero field splitting in fig. 4.2b is reduced, it remains finite. Due to lattice mismatch between BeSe and ZnSe and the high Be content of the tunnel barrier material, the interface is still subjected to strain, even though the contribution stemming from the lattice mismatch to the substrate is removed. The remaining zero field splitting could either result from this remaining lattice mismatch at the interface, or from other imperfections such as alloy or doping fluctuations. In the light of this remanent spin-splitting, a future, more detailed analysis of lifted RTDs with different Be and Mn contents as well as tunnel barrier thicknesses is desirable.

In summary, the apparent reduction of remanent zero field splitting, the increase in sharpness of the resonance as well as the reduction of the non-resonant background current shown in fig. 4.2b and d can be explained by a strain relaxation process due to the removal of the substrate. This adds further support to the assumptions made on the origin of both the Gaussian broadening and the remanent zero field splitting made in chapter 3.



# Chapter 5

## A voltage controlled spin-valve

As semiconductor spintronics moves beyond basic issues such as electrical spin injection [Schm 00, Rash 00, Appe 07] and detection [Lou 07, Appe 07], attention is shifting to combining the fundamental building blocks into useful compound devices. Slobodskyy et al. demonstrated one such device in the form of a voltage controlled spin filter based on a (Zn,Mn,Be)Se DMS RTD. Equipped with a comprehensive understanding [Ruth 11] of such a device, a logical extension is to couple two of these devices into a spin injector and detector pair. In this chapter, we show how such a structure can be operated as a paramagnetic voltage controlled spin valve. Such a device could lead to a full implementation

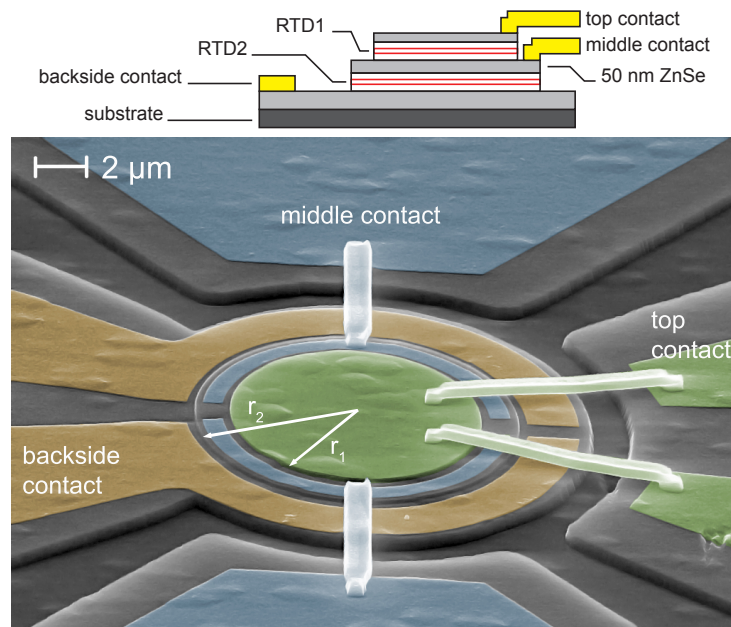


**Figure 5.1:** SEM image of the spin valve device with colors added to highlight the various elements. Top (green) and middle contact (blue) layers are connected to bond pads via metal air-bridges, while the backside (orange) contact layer is bonded directly. The schematic shows a side profile of the device.

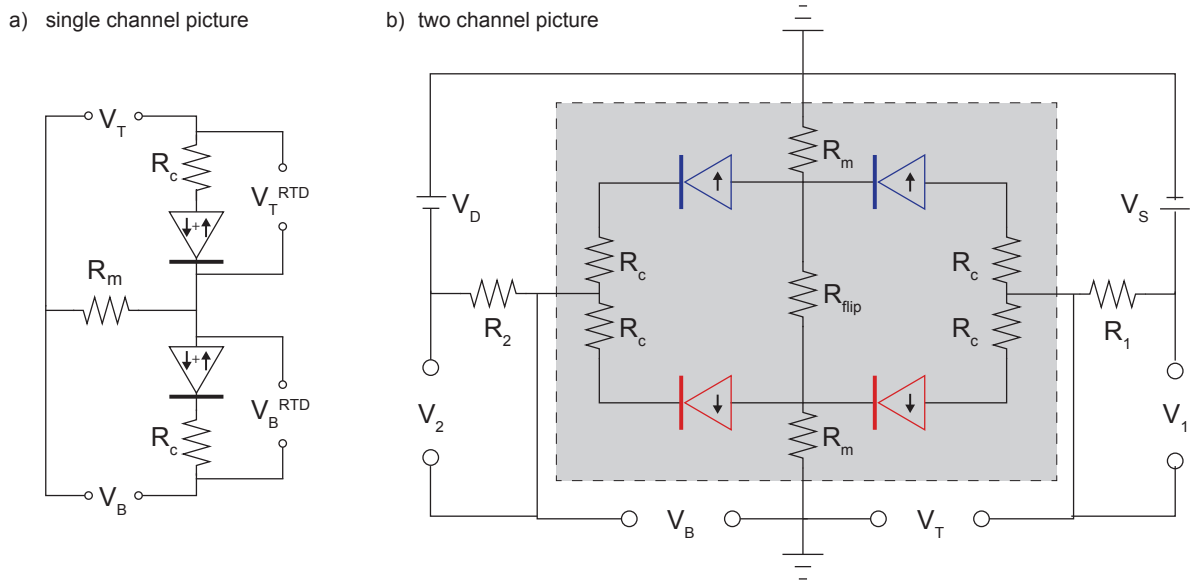


**Figure 5.2:** Kirchhoff circuit of the device. a) equivalent circuit for the internal properties of the device in a one channel picture. b) circuit diagram of the two channel model including the description of the experimental configuration.  $V_S$  and  $V_D$  are the source and drain voltages applied to the device, while  $V_1, V_2, V_T$  and  $V_B$  are measured. The circuit in the shaded area is the extension of a) for the two channel model, describing the internal device properties.

of spin based logic in a material system that does not exhibit ferromagnetism.

Figure 5.1 shows a scanning electron microscope (SEM) image of our device along with a schematic side view. Each of the RTDs is comprised of a 7 nm thick magnetic (Zn,Mn)Se quantum well sandwiched between two 5 nm thick (Zn,Be)Se barriers. These are separated by a 50 nm ZnSe layer, highly doped ( $n = 1.5 \cdot 10^{19} \text{ cm}^{-3}$ ) to allow for proper electrical contacting. This layer stack is patterned into a circular pillar of varying diameter, with the largest part forming a mesa in the contact layer to accept the backside contact. The next level, of radius  $r_2$ , exposes a ring shaped area on top of the bottom RTD, where a middle contact is formed. The upper level of radius  $r_1$  is fitted with a contact to the top RTD. Top and middle contacts are then connected to large contact pads using an air-bridge technique [Borz 04]. The data presented in this chapter is from two devices A and B, where the diameters of the top and bottom RTDs are 10 and 12.8  $\mu\text{m}$  for sample A and 5 and 6.4  $\mu\text{m}$  for sample B, respectively.

## 5.1 Measurement and single channel analysis

Transport characterization of this sample is done in a 4 K bath magnetocryostat using the electrical circuit given in fig 5.2b. The shaded area represents the device as a whole (the internal details will be discussed when describing the model), which is grounded at its middle contact, and connected to voltage sources at its top and bottom, through standard

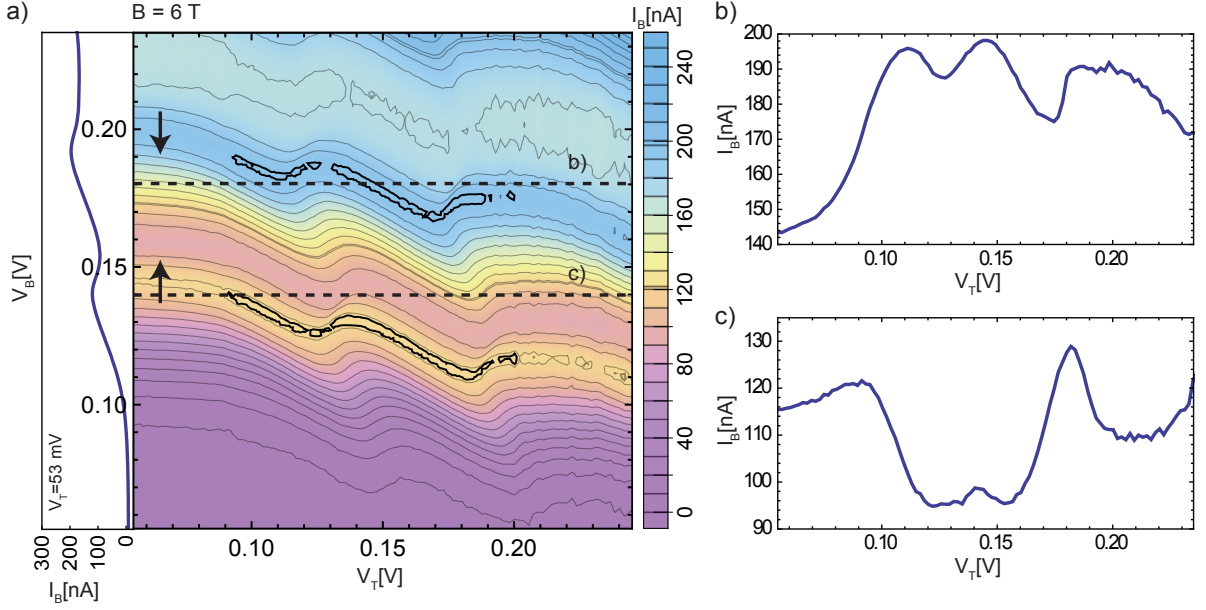


**Figure 5.3:** a)  $I_B - V_T - V_B$  characteristics at  $B = 6$  T for sample A. On the left hand side of the  $V_B$  axis of fig. a) the  $I_B - V_B$  characteristic at  $V_T = 53$  mV is shown. b)+c)  $I_B - V_T$  characteristics at  $V_B = 140$  mV and  $V_B = 180$  mV along the dashed lines in fig. a)

resistors  $R_1$  and  $R_2$ , respectively. Four voltmeters are used to measure the voltage drops  $V_T$ ,  $V_B$ ,  $V_1$  and  $V_2$  as indicated, allowing us to determine both the voltage drop across and the current flowing through each diode.

The results of a measurement performed in a magnetic field of 6 T are shown in fig. 5.3a, where the current flowing through the bottom RTD is plotted as a function of the bias voltages dropping over each of the two RTDs. Some lines of equal current are drawn darker as a guide to the eye, indicating the positions of the two spin-split resonances of the bottom RTD. The kinks in these lines, which occur when these resonances intersect the resonances of the top diode, are accompanied by small changes in amplitude (noticeable by the slight increase in distance between the lines of equal current in the figure) which are a result of the spin valve effect.

Figures 5.3b+c give cross-sections of this data at the two constant bottom diode bias voltages indicated by the dashed horizontal lines in fig. 5.3a. The pronounced dependence of  $I_B$  on the bias voltage dropping across the top RTD clearly shows the strong interaction between the two RTDs of the spin-valve.

For a better understanding of this crosstalk, we at first discuss the internal properties of the spin-valve in the simple one channel picture of fig. 5.2a. The measured voltage drops  $V_T$  and  $V_B$  across the top and bottom diode are comprised of the effective bias voltages  $V_T^{RTD}$  and  $V_B^{RTD}$  at the respective RTDs (including the comparably small top and bottom contact resistances  $R_C$ ) and the voltage drop across the middle contact resistance  $R_m$ . The observed crosstalk stems from the fact that the middle contact resistance  $R_m$  is in the current path of both  $V_T$  and  $V_B$ . As we change for example only  $V_T$  in the equivalent circuit

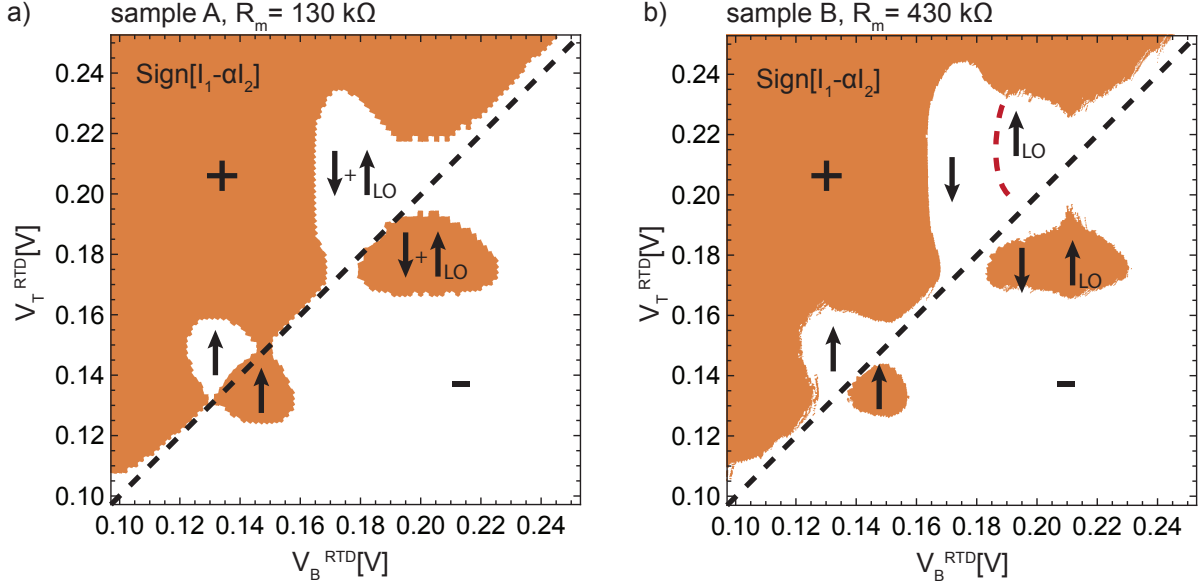


**Figure 5.4:** The sign of  $I_T - I_B$  illustrates the regions whether current is dumped into the middle contact or flows from the middle contact. a) Device A with a middle contact resistance of  $R_m = 130 \text{ k}\Omega$  b) Device B with a middle contact resistance of  $R_m = 430 \text{ k}\Omega$

of fig.5.2a, the voltage redistributes according to Kirchhoff's laws. More importantly, as the resistance of both RTDs change significantly with  $V_T^{RTD}$  and  $V_B^{RTD}$ , the influence of  $V_T$  on  $V_B^{RTD}$  is potentially strong, explaining the observed  $I_B - V_T$  characteristics in fig 5.3b+c.

Let us assume that the transport properties of the spin valve can be explained within the equivalent circuit of fig.5.2a. A straight forward way to visualize the spin-valve behavior is to plot only electrons traversing both RTDs. Electrons which are injected by the top RTD and exit the device via the middle contact are not of interest to us. The same is true for electrons that enter via the middle contact and exit the bottom RTD. In both cases, these electrons either come from or exit to an unpolarized reservoir and do not play a role in the spin-valve functionality.

The current traversing both RTDs is always given by the smallest of the two currents  $I_1$  and  $I_2$  flowing through the top and bottom RTD, respectively. If  $I_1 > I_2$ , some of the current exits the middle contact, while the remaining current also traverses the bottom diode. For  $I_2 > I_1$  an additional current is supplied by the middle contact and only the current entering at the top of the spin valve traverses both RTDs.

As already mentioned, the resistance of each RTD highly depends on its applied bias voltage. Which one of the two currents is smaller thus depends on the bias voltages  $V_T^{RTD}$  and  $V_B^{RTD}$  dropping across the top and bottom RTD. Figures 5.4a+b plot the sign of  $I_1 - \alpha I_2$  for devices A and B as a function of  $V_T^{RTD}$  and  $V_B^{RTD}$ .  $I_2$  is scaled by a factor  $\alpha$ , accounting for the different sizes of the top and bottom RTDs. A comparison of  $I_T - V_T$  and  $I_B - V_B$  characteristics yields scaling factors of 0.67 and 0.94 for devices A and B,



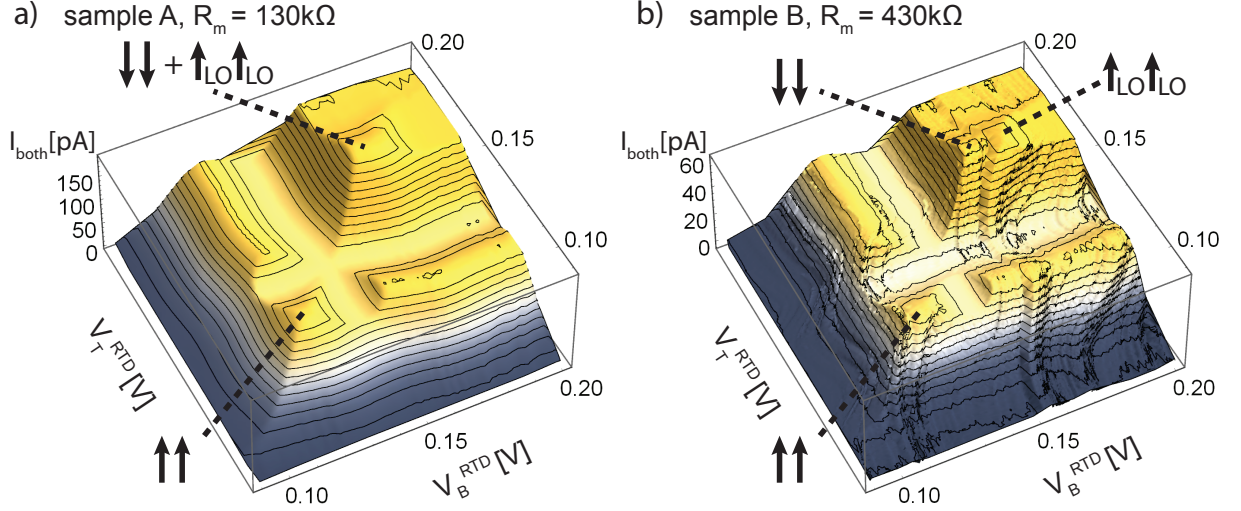


**Figure 5.5:** a)+b) Current traversing both diodes as a function of the bias voltages of the two diodes for devices A and B, respectively.

respectively. Within the one channel picture, the effective bias voltages  $V_T^{RTD}$  and  $V_B^{RTD}$  are extracted from the measured voltages  $V_T$  and  $V_B$  by subtracting the voltage drop across  $R_m$ . As is clear from the equivalent circuit in fig. 5.2a, plotting  $I_B$  as a function of  $V_T^{RTD}$  should result in a constant  $I_B$  for all  $V_T^{RTD}$ . Hence, we estimate  $R_m$  by changing its value until such a situation is reached and find contact resistances of 130 k $\Omega$  and 430 k $\Omega$  for devices A and B, respectively.

In fig. 5.4 we have removed the crosstalk of the two devices via the middle contact resistance as well as the resistive influence stemming from the different sizes of the top and bottom RTD. The color coded plot is thus comparing the intrinsic properties of the two RTDs. The apparent symmetry along 45° indicated by the dashed line in fig. 5.4 is expected for two equal RTDs and is used as an additional tool to verify the scaling factors discussed above. The sign changes in the region labeled with two spin-up arrows occurs when both RTDs are tuned to their spin-up resonance. A similar feature arises at higher bias voltages when both RTDs are set to their spin-down resonance. Its shape however differs from the first feature as we get an additional contribution from both spin-up replica peaks occurring at similar bias voltages.

We do not see evidence for additional features when one RTD is set to its spin-up resonance and the other RTD to its spin-down resonance and vice-versa. This however does not yet exclude spin-flip processes between the two RTDs. Background contributions at the spin-down resonance are much stronger than for the spin-up resonance-peak at lower bias voltages. The analysis presented in fig. 5.4 does thus not yield a spin-flip signal, even if it were present.

Figure 5.5 plots the current traversing both RTDs as a function of  $V_T^{RTD}$  and  $V_B^{RTD}$ . Rescaling  $I_2$  with  $\alpha$  again reveals the same features as in fig. 5.4 and are labeled accordingly. For an ideal spin-valve this plot would yield only two peaks, as the valve only

transmits current if both RTDs are set to transmit the same spin type (parallel setting). In case of spin-flips in the area between the two RTDs two more peaks would arise for the antiparallel settings. Although the plot of  $I_{both}(V_T^{RTD}, V_B^{RTD})$  in fig. 5.5 shows what could be interpreted as the four discussed features, the long tails are *not* a result of a spin-flip contribution to the resonant transport. They again arise due to characteristic background of each RTD and the analysis described above. At small applied bias voltages either one of the RTDs results in a high resistance and the current traversing both RTDs is almost zero, since most of the current is either coming from or going to the middle contact. As discussed above, the first peak arises when both RTDs are set to their spin-up resonance, Increasing  $V_T^{RTD}$  while maintaining  $V_B^{RTD}$  at the first resonance will put the top RTD in the valley between its first peak and the increasing background current (and second resonance).  $I_{both}$  is thus given by  $I_1$  until due to the increase of the background current and/or the second resonance  $I_2$  is greater than  $I_1$ .

We conclude that the single channel analysis does not yield conclusive evidence for a spin-valve functionality. In the following we therefore discuss a two channel model, which treats spin-up and spin-down transport channels separately.

## 5.2 The two channel model

The reason that the data of fig. 5.3a does not show an explicit off state for our spin valve is that the middle contact ground actually has an active role in device operation. The middle contact resistance is however a necessary element to allow for independent control of the two RTDs. Specifically, when one of the spin channels in either diode is off-resonance, then its resistance is ideally infinite. The middle grounding contact then provides an alternative current path. Each RTD can be either set to transmit spin-up or spin-down electrons. Figure 5.6 shows the four resulting possible settings for the spin-valve. In fig. 5.6a, the bottom RTD is set to transmit only spin down, while the top RTD is allowing spin up current to flow. The spin up current traversing the top RTD will not be able to enter the bottom RTD, but instead divert into ground. This does not however prevent a current from flowing through the bottom RTD, as the same ground contact can act as a source of spin down current to supply this diode. A similar situation is shown in fig. 5.6b, with top diode set to spin-down and the bottom diode set to spin-up. For completeness, fig. 5.6c+d show the two on states of the spin valve, when both RTDs are set to transmit the same spin species.

A more detailed analysis is therefore necessary to assess the performance of the spin valve. The essence of the model is contained in the equivalent Kirchhoff circuit of fig. 5.2b. The device is described in a two channel model [Fert 68], as a spin-up and spin-down path in parallel, each comprised of two RTDs in series.

A key element is the description of the middle contact, for which two important aspects must be considered. First, the resistive value of the middle contact to ground is important.

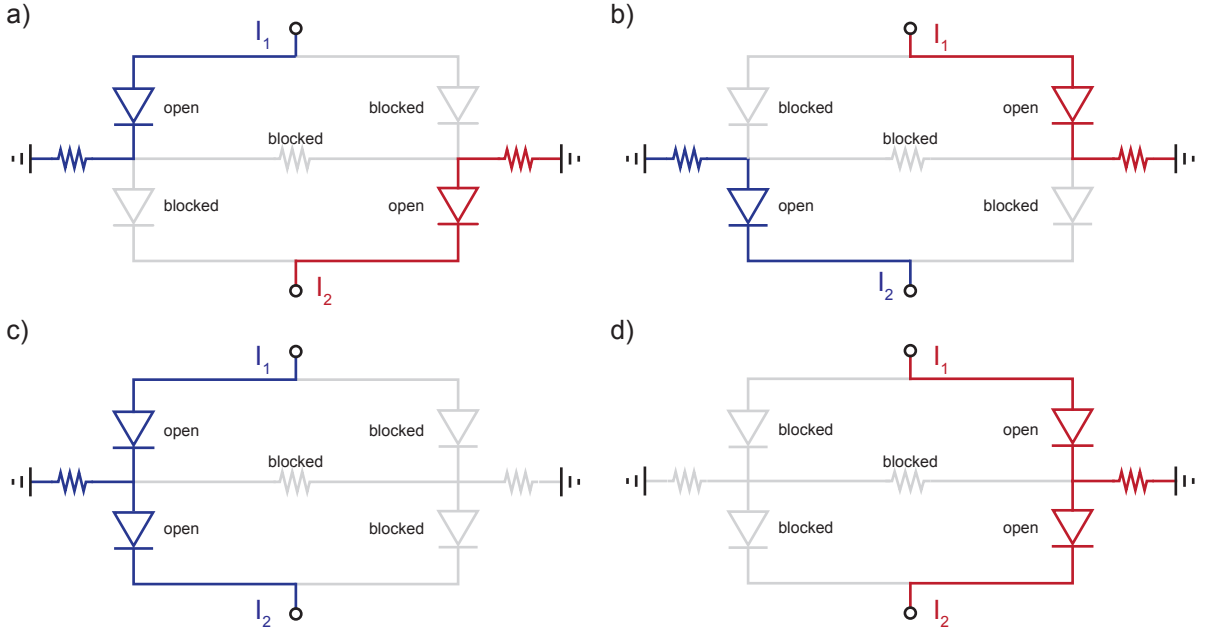


**Figure 5.6:** Four modes of spin-valve operation a+b) Top and bottom RTD are set to transmit opposite spin species. Electrons injected by the top RTD are blocked by the lower RTD and are thus diverted into ground. A current however still flows through the bottom RTD as the same ground contact acts as a source of electrons of the opposite spin type. c+d) Both RTDs transmit the same spin species.

If this resistance is too low, then the shorting effect described above would completely decouple the two RTDs and prevent any spin valve functionality. If on the other hand this resistance is too high, it would, since it is essentially in series to the RTDs, cause circuit bistabilities [Fost 89] and destabilize device operation. This is shown in fig. 5.7, where a load line analysis according to fig. 5.2a is plotted for various middle contact resistances. Given the other relevant parameters in our circuit, the middle contact resistance of  $\approx 130$  k $\Omega$  in device A falls in the appropriate intermediate range. As evidenced by the small jumps in fig. 5.5, occurring near the resonant features, the device resistance of  $\approx 430$  k $\Omega$  in device B is already slightly too large. If not stated otherwise, subsequent analysis will thus be on device A, while a summary of the results is given for device B at the end of this section.

Second, while the thickness of the middle contact (50 nm) is below the expected spin-flip length in doped ZnSe [Lehm 05], spin flip processes cannot be assumed to be negligibly small. In order to take these spin flip processes into account, a scattering resistance ( $R_{flip}$ ) between the two spin channels is included in the two channel model.

For completeness, the contact resistances ( $R_c$ ) at the top and bottom of the device are also indicated in the circuit. However, since these have been optimized to minimize their resistance, they are negligibly small (of order 1 k $\Omega$ ) compared to the middle contact resistance with which they are in series, so they can safely be neglected in the subsequent

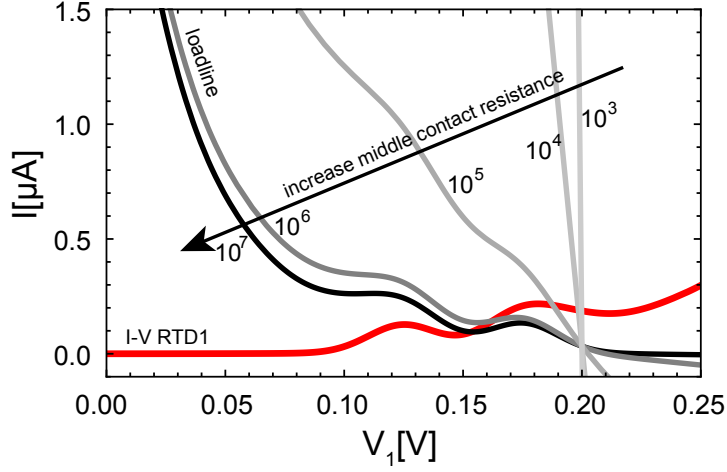


**Figure 5.7:** a) Load line analysis for various middle contact resistances showing the current flowing through the middle contact resistance and the bottom RTD plotted on the axis of the top RTD. reservoir.

modeling. Having established the correct equivalent circuit, the full model reduces to simply solving Kirchhoff's laws. All resistors in fig. 5.2b are linear, and each of the RTD elements in the circuit is modeled as described in Ref. [Ruth 11]. While the non-linear behavior of the RTDs prevents an analytical solution, this equivalent circuit can be solved numerically, and doing so reproduces all features of the measurements.

This is evidenced in fig. 5.8, which compares the results from the model (dots) to the experimental data (lines) for  $I_T - V_T$  curves at 6 T, showing the current flowing through the top diode as a function of the bias voltage  $V_B$  across this diode, and this for three different values of the bias across the bottom diode. As suggested above, the primary influence of the bottom diode on the  $I_T - V_T$  curves of the top diode results from the existence of the middle contact. Current leaving the top diode has the choice of two parallel paths to ground, either through the middle contact or the bottom contact. As the resistance of the bottom diode changes, so does the effective resistance to ground. This resistance to ground is the series resistance that sets the lever arm for converting the voltage scale to an energy scale for the top diode. Changes to the resistance of the bottom diode thus constitute an effective rescaling of the voltage axis in the I-V curves of the top diode [Ertl 07], accounting for the shift seen in figure 5.8.

In order to distinguish between this pure resistive influence of the diodes on each other and the actual spin valve mechanism, a more detailed examination of the data is needed. The spin-valve effect is best seen in how the conductance  $G_B = I_B/V_B$  of the bottom diode reacts to the change in the voltage falling across the top diode. Figure 5.9 plots the second derivative of  $G_B$  with respect to the top voltage,  $d^2(G_B)/(dV_T)^2$ , and this as a function of the voltage drop across each diode. Figures 5.9a and b are the experimental data whereas figure 5.9c and d are the results of the model for two different values of the spin scattering resistance. In all cases, the results are filtered with a cubic spline before

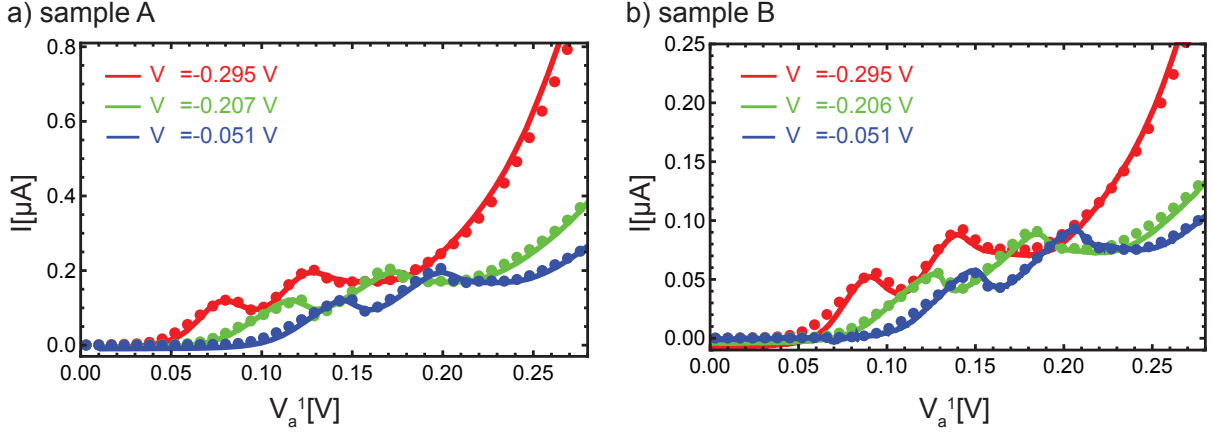


**Figure 5.8:** a)+b) Experimental (lines) and model (dots) current-voltage characteristics of the top diode for various voltages across the bottom diode for samples A and B respectively.

the derivative is taken.

Plotted this way, the experimental data seen in fig. 5.9a shows a fairly complex pattern of conductance resonances. In order to more clearly explain this pattern, the same data is reproduced in fig. 5.9b, overlaid with a schematic diagram identifying the different features. If the two diodes acted as non-interacting elements connected in series, each with a spin split resonance, then we would obtain a simple square grid in the shape of a number symbol (#), with the two horizontal lines representing the resonances of the bottom diode and the two vertical lines those of the top diode. The rescaling of the lever arm caused by the resistive influence of each diode on the other causes these lines to bend, and also to kink near their intersection points, deforming the pattern as sketched in fig. 5.9b. The structure is then further enriched by the additional resonances stemming from the LO-phonon assisted replicas of the main resonance peaks [Gold 87a]. These are highlighted as dashed lines in fig. 5.9b.

We now compare this experimental data to the plots resulting from the model. In fig. 5.9c, significant spin conservation is assumed (as modeled by using a spin flip resistance of  $230 \text{ k}\Omega$ ), whereas fig 5.9d is for the case of full spin relaxation ( $R_{flip}=10 \Omega^{-1}$ ). In both cases, the model reproduces well the data for the primary peaks. A significant difference is however observed when examining the behavior of the phonon replica peaks. In the case of full spin relaxation (fig. 5.9d) the spin up phonon replica and the spin down resonance partially overlap and become nearly indistinguishable from each other. This is also the case for individual RTDs and results from the saturation spin splitting energy in  $\text{Zn}_{0.92}\text{Mn}_{0.08}\text{Se}$  [Twar 84] and the LO-phonon energy [Land 99] being similar.

This situation is different for the spin conserving case (fig. 5.9c). Here, the lever arm rescales independently for the spin up and spin down branch of the device. The resulting different lever arm for the spin up LO-phonon peak and the spin down resonance separates

<sup>1</sup> $10\Omega$  is chosen for the model instead of  $0\Omega$  since a too small resistor causes numerical instabilities

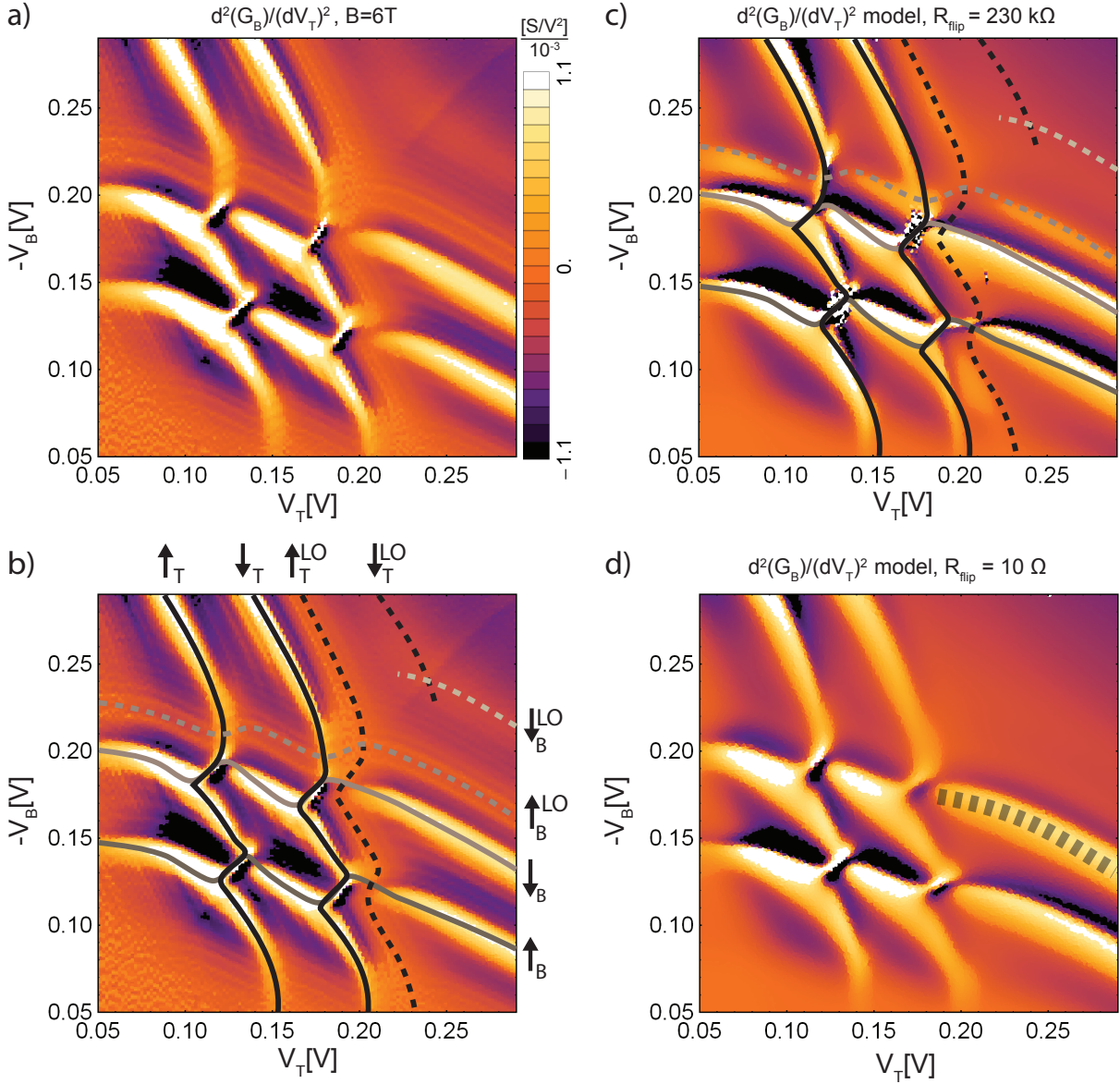


**Figure 5.9:** Second derivatives of data and model as a function of the two diode biases. The dashed lines are guides to the eye to depict the differences between the model with full spin relaxation between the RTDs (c), the model with decoupled spin channels (d) and the measurement (a+b).

them and both become clearly visible. Comparing the experimental data of fig. 5.9a to fig. 5.9c and d, it is clear that the spin conserving case is the one which correctly describes the experiment. To emphasize the correspondence of this model to the experiment, the identical schematic grid used in fig 5.9b is reproduced in fig. 5.9c.

As an estimate of the level of spin conservation in the device, we note that the spin flip current flowing through the  $230 \text{ k}\Omega$   $R_{flip}$  is an order of magnitude smaller than the current exiting the device from the bottom RTD. Note also that assuming significantly

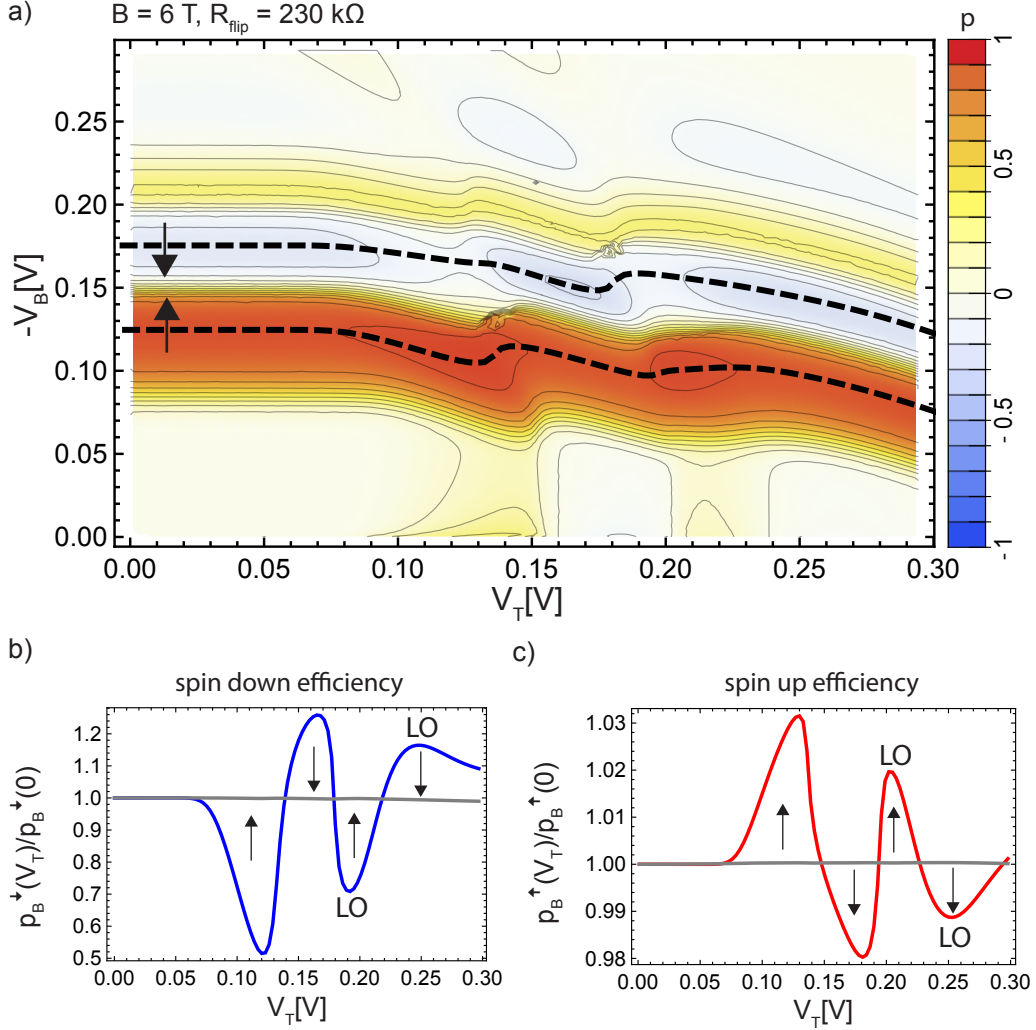


**Figure 5.10:** a) Polarization of the current exiting the bottom RTD as a function of the voltage across each RTD. The dashed lines indicate the positions of the resonances of this RTD. b)+c) Line plots of the polarization following the dashed lines in a), normalized to the natural spin filter efficiency of the diode (see text).

higher values of  $R_{flip}$  (or more perfect spin conservation) begins to modify the lever arms, and causes a misfit between the main peaks in the model and the experiment.

Having established the correct degree of spin conservation required to describe the experiment, it is now a simple matter to extract the spin valve efficiency from the equivalent circuit. The polarization of the current exiting the second diode is given by  $p = (I_B^\uparrow - I_B^\downarrow)/(I_B^\uparrow + I_B^\downarrow)$ , and is plotted as a color scale in fig. 5.10a as a function of the voltage across each diode. The dashed lines show the position of the two resonances of the bottom diode. Due to the afore discussed crosstalk of the RTDs, these dashed lines are a function of both voltages and need to be computed. A description thereof is given in appendix A.2.

If full spin relaxation was taking place between the two RTDs, the device would reduce

to a simple spin filter. The current flowing along each of these dashed lines would still be spin polarized as a result of the spin filtering properties of the bottom diode, but its polarization would be constant, and independent of the voltage on the top diode. To get a measure of the spin valve efficiency, we plot in fig. 5.10b and c the spin polarization of the current exiting the second diode as a function of the voltage on the first diode, while following the dashed lines in fig. 5.10a. The data is normalized when 0 V is applied to the top diode, since in this case, current comes from the unpolarized middle contact, and this thus corresponds to the natural spin filtering of the bottom diode. Departures from a value of 1 are then a direct measure of the pure spin valve effect of the device.

For each spin channel of the bottom diode, we see two regions of enhancement and two of reduction of the spin polarization. The enhancement occurs when the top diode is tuned such that either the main resonance or its phonon replica are transmitting a spin parallel to the analyzer setting, whereas the regions of reduction come from the two diodes being set to select opposite spins.

The efficiency of the spin valve appears much larger for the spin down than the spin up channel. This results from the properties of the individual diode. As seen in fig 5.10a (by looking at values near the left axis), the natural spin filtering efficiency of the bottom diode is approximately 90% for spin up, but only 35% for spin down. This difference comes from the second peak being superimposed with a larger background current and the LO replica of the first peak. Similar values are true for the top diode. The big difference in efficiency of the two channels is a reflection of the fact that in one case the analyzer is being fed a 90% polarized signal whence in the other case it sees an incoming signal with 35% polarization.

To further test the generality of the model, we conduct the same analysis on device B, adjusting the model for the different device geometry and middle contact resistance. Even though the middle contact resistance in this device is at the upper end of the acceptable range and causes the device to exhibit mild current instabilities, the model reproduces all results on device B, as exemplified in fig. 5.8b. The analysis of the polarization of the current exiting the bottom RTD, yields comparable spin valve efficiencies as for device A.

In summary, we have demonstrated a voltage controlled spin valve comprised of two magnetic RTDs in series which act as an injector and analyzer pair. The behavior of the compound device is fully described by implementing a preexisting model [Ruth 11] describing the individual diodes into a basic Kirchhoff equivalent circuit, allowing for a quantitative assessment of the spin valve efficiency.

### 5.3 Zero magnetic field operation

In chapter 3 we show that BMP-like states at the interface of the quantum well layer lead to a zero field spin polarization in these devices. In the light of this and the findings of the previous section, spin-valve operation without the need for an external magnetic field



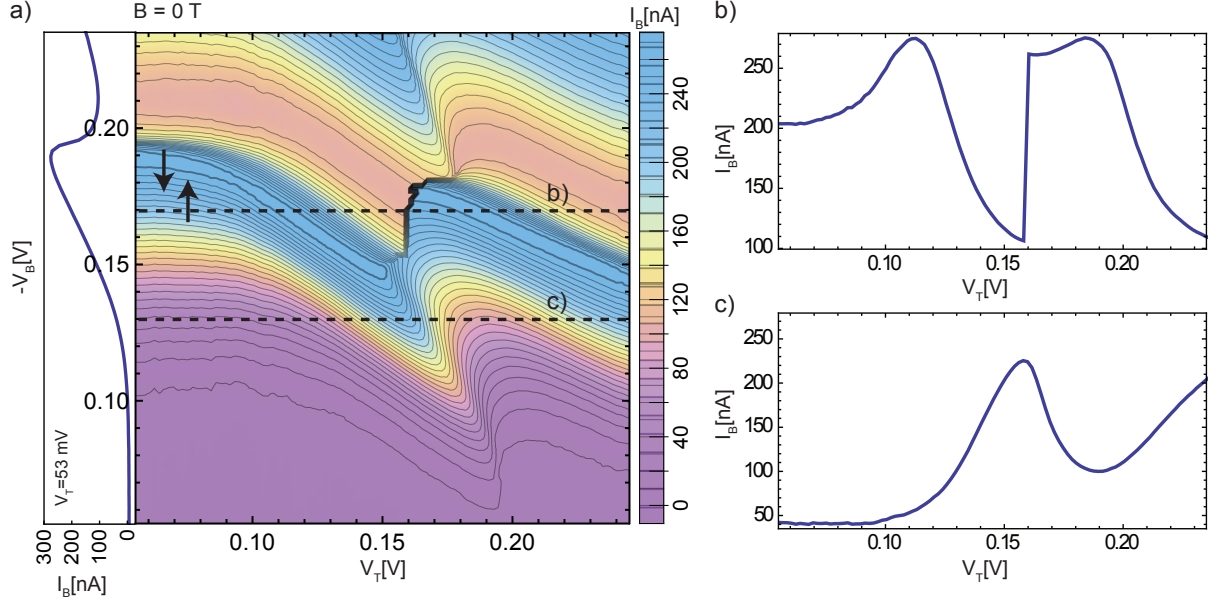


**Figure 5.11:** a)  $I_B - V_T - V_B$  characteristics at zero magnetic field for sample A. On the left hand side of the  $V_B$  axis of fig. a) the  $I_B - V_B$  characteristic at  $V_T=53$  mV is shown. b)+c)  $I_B - V_T$  characteristics at  $V_B=140$  mV and  $V_B=180$  mV along the dashed lines in fig. a) The apparent jump in fig b) is due to the pronounced NDR regions of the top and bottom RTDs at zero magnetic field coinciding at certain bias voltages  $V_B$  and  $V_T$ .

seems feasible. While the model indeed suggests a remanent zero field splitting of the resonance-peaks for both diodes, we however show that proper spin-valve operation is not possible at zero magnetic field. For the above stated reasons, we study the zero field data of device A.

As done for the data at  $B=6$  T, fig. 5.11a plots the current through the bottom diode as a function of the voltages across the top and bottom RTD, however without an applied external magnetic field. In contrast to the  $B=6$  T data, the measurements done at zero magnetic field show strong current discontinuities when both RTDs are biased in the vicinity of their resonance-peaks. This is best seen on the cross-section of fig. 5.11a along the dashed line labeled b). Figure 5.11b plots  $I_B - V_T$  along this dashed line. A bistable circuit configuration is evidenced by the sudden jump of  $I_B$  at approximately 160 mV. For completeness, we plot a second  $I_B - V_T$  characteristic along the second dashed line labeled c). Figure 5.11c does not exhibit a current instability as it is only governed by the resonance-peak of the top diode.

Without the external magnetic field, the splitting of the resonance-peaks of each diode is reduced to its remanent value of 9 meV. On resonance, the overlap of the two resonances increases and the total diode resistance, given by the applied bias voltage divided by the superposition of the current through both spin-channels, is lowered. At  $B=0$  T we find peak currents of  $\approx 300$  nA, while at  $B=6$  T the maximum peak current is  $\approx 200$  nA (at comparable bias voltages). As the middle contact resistance however is only subjected to

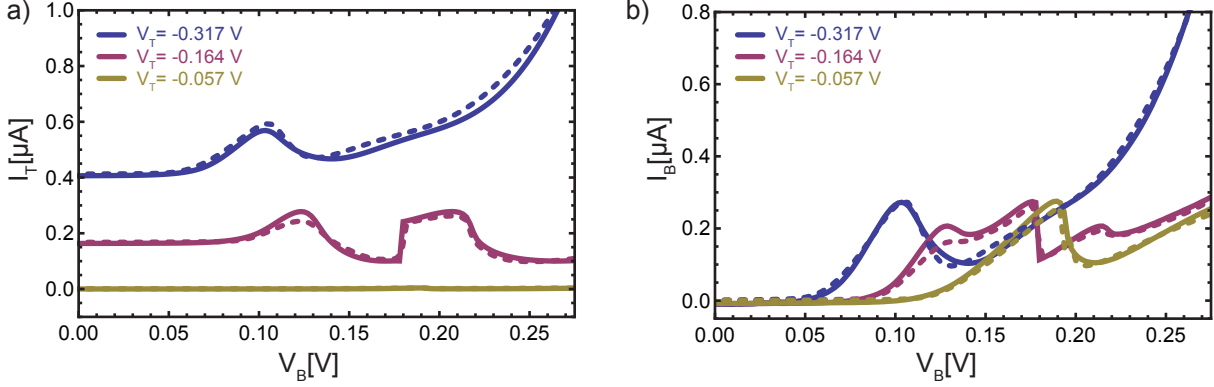


**Figure 5.12:** a)  $I_T - V_B$  characteristics for various  $V_T$ . While the influence on the current b) I-V characteristics at various  $V_T$  settings. When both diodes are set to the bias region of their resonances, instabilities occur in the circuit. This is much more pronounced at zero field since the total on-resonance resistance is much lower than for the spin split peaks at 6 T. The zero field curve is thus the best way to determine the ratios between the resistance of the active RTD region and all involved ohmic contacts.

a small change of its magnetoresistance, the circuit exhibits current instabilities at  $B=0$  T due the changes in the diode resistances. While a reduction of the middle contact resistance would overcome this problem, the spin-valve efficiency would however be reduced at the same time, as discussed in the previous chapter.

Although device A exhibits current instabilities at zero magnetic field, the behavior of the spin-valve is still fully described by our two-channel model assuming a spin-flip resistance of 70 k $\Omega$ . Figures 5.12a+b show fits (dashed lines) to the zero magnetic field  $I_T - V_B$  and  $I_B - V_B$  characteristics (full lines), respectively. The two channel model is able to reproduce the apparent jumps in the  $I_T - V_B$  and  $I_B - V_B$  characteristics. The purple line in fig. 5.12a shows a similar situation as in fig 5.11b, while the purple line fig. 5.12b is the equivalent of a vertical cross-section of the data shown in fig. 5.11a. That the bistabilities seen in these purple lines are fully reproduced by the equivalent circuit of fig. 5.2b indicates that the latter are due to the resistive properties of the circuit [Fost 89], and not an intrinsic property of the RTD [Gold 87b].

To further test the validity of the fits to the I-V characteristics in fig. 5.12, we again plot in fig. 5.13a+b  $d^2(G_B)/(dV_T)^2$  of the experimental and model data, respectively. As for  $B=6$  T, the model achieves good agreement to the experiment. Plotting the model for  $R_{flip}=10 \Omega$  does however yield very similar results (not shown). Note that the apparent instabilities in fig. 5.12 are however only reproduced at the correct bias voltages for a middle contact resistance of 70 k $\Omega$ .

As the model is able to account for even the current instabilities in the device, we again extract the spin-valve efficiencies. Figure 5.14a plots the polarization  $p$  of the current exiting the bottom RTD at zero magnetic field as a function of the voltage across each diode. Compared to the  $B=6$  T data, the spin-valve exhibits only a very narrow region

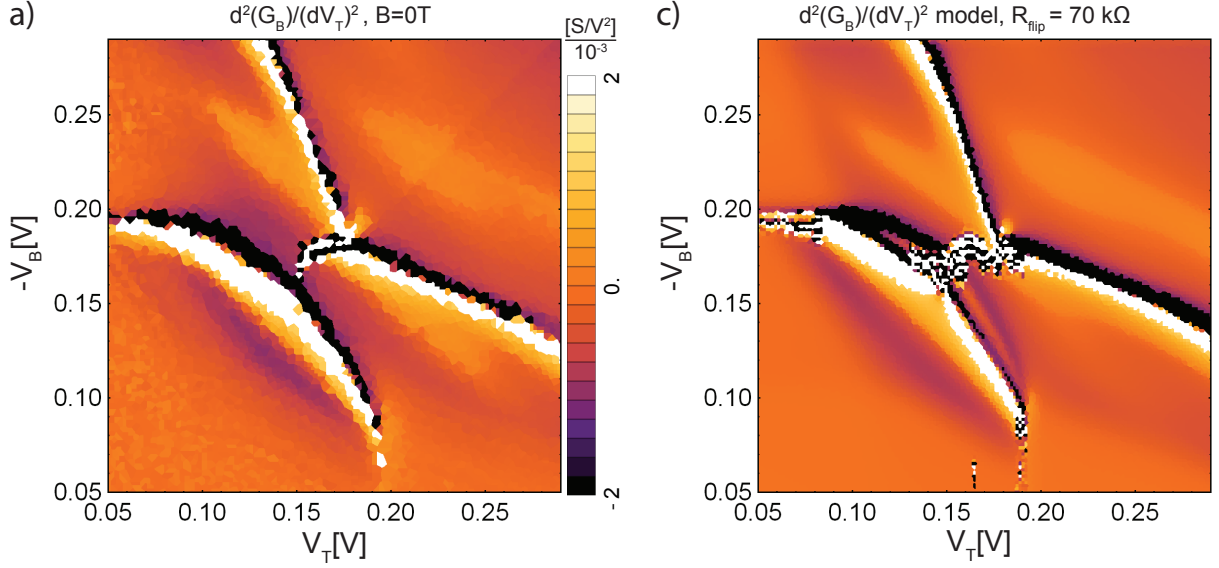


**Figure 5.13:** second derivatives of data and model for zero magnetic field as a function of the two diode biases. As for the  $B=6 \text{ T}$  case, the spin-valve signal (a) is reproduced very well by the two channel model (b).

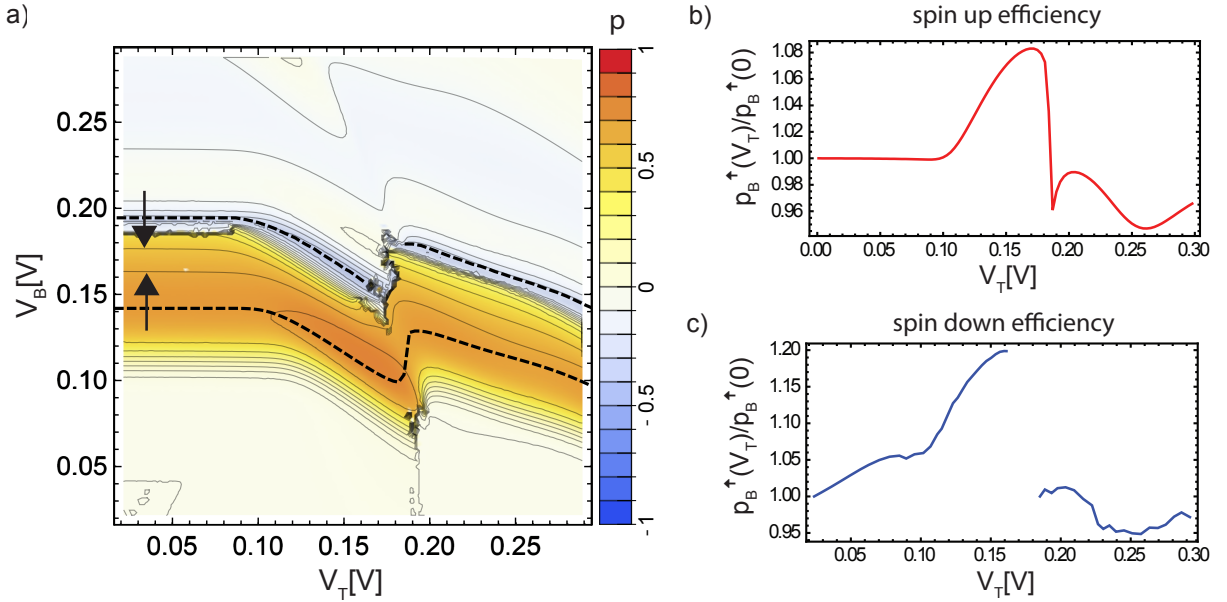


**Figure 5.14:** a) polarization at zero external magnetic field of the current exiting the bottom RTD as a function of the voltage across each RTD. The dashed lines indicate the positions of the resonances of this RTD. b)+c) line plots of the polarization following the dashed lines in a), normalized to the natural spin filter efficiency of the diode (see text).

of spin up polarization at zero magnetic field, which is a combined effect of the resonance positions and the peak amplitudes of the two spin-channels at  $B=0 \text{ T}$ . Figures 5.8b and c plot the spin-valve efficiencies along the dashed lines in fig. 5.8a. The apparent jumps in

the spin up efficiency shows that spin-valve operation is also subjected to the bistabilities present in the I-V characteristics and does not reproduce a continuous spin-valve signal as shown in fig. 5.10b+c. More importantly, the spin-down efficiency shown in fig. 5.8c exhibits a small bias range at approximately 170 mV where no proper spin-valve efficiency can be defined.

In summary, the zero magnetic field operation of the spin-valve has not proven to offer the same amount of control as in the  $B=6$  T case. The evidence for spin conservation between the two RTDs is less conclusive than for the  $B=6$  T case. Nevertheless the model shows good agreement to the additional  $B=0$  T data and is even able to properly reproduce the apparent current instabilities in the device, caused by magnetoresistance effects of the two RTDs.

# Chapter 6

## Fermi-edge singularity in a non-magnetic self-assembled quantum dot resonant tunneling diode

The resonant tunneling phenomena observed in quantum well RTDs is a result of the reduced dimensionality of the quantum well layer. The resonant states form due to the vertical confinement between the two tunnel barriers. As we have learned in the previous chapters, additional lateral confinement in these resonant tunneling devices leads to enriched transport physics due to the BMP states at the quantum well interface.

The reduced dimensionality in resonant tunneling devices has led to the observation of new fundamental transport properties, such as coulomb blockade in artificial atoms [Taru 96] or many body correlation effects such as the Fermi edge singularity (FES) [Geim 94]. Previous experimental studies of FES have been limited to III-V devices, often at high magnetic fields. Here we report on the observation of a FES in an all-II-VI semiconductor resonant tunneling diode (RTD) without an applied magnetic field.

### 6.1 The Fermi-edge Singularity

The response of a Fermi sea of electrons to a sudden appearance of a localized perturbation manifests itself as a Fermi-edge singularity. This many body correlation effect is known from X-ray absorption in metals [Maha 67, Nozi 69], where an enhancement of the absorption is observed near the Fermi-edge. A similar enhancement was also predicted for the I-V characteristics of tunneling through localized levels, as the photon itself does not play a role in the solution of the X-ray problem [Matv 92]. The first experimental observation of the latter was by Geim et al., where resonant tunneling through an 0D impurity state embedded in a quantum well layer shows this enhancement if the impurity

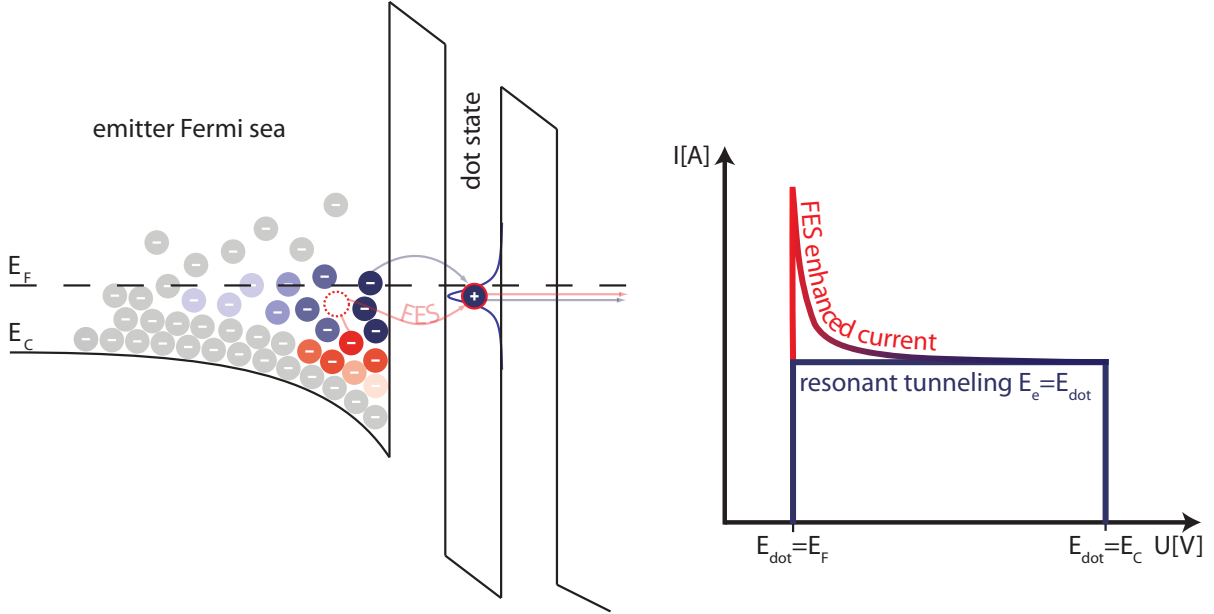


**Figure 6.1:** a) Illustration of the FES mechanism. Additional electrons (red) are able to tunnel into the localized site from an initial state that would not contribute to the resonant tunneling current without the many body correlation effect (blue). b) Schematic of the resulting resonant tunneling current as a function of the applied bias voltage.

state is aligned with the Fermi energy of the emitter states [Geim 94].

The theoretical predictions for the FES in resonant tunneling transport [Matv 92] are made for a localized level situated below the Fermi edge of both emitter and collector. At first, transport is blocked since the collector states are fully occupied at zero temperature and zero bias voltage. The applied bias voltage lowers the chemical potential of the collector states and as soon as the localized state is aligned with the Fermi energy of the collector, electrons tunnel from the localized state into the collector. The authors assume that the state is always occupied and the bottleneck of the transport is thus tunneling into the collector. The enhancement of this tunneling rate is due to the presence of the collector Fermi sea, and decays with a power law as the distance between the localized state and the Fermi-edge is increased via the applied bias voltage.

In the experimental observations of the FES enhancement in resonant tunneling through impurity states [Geim 94] and self-assembled III-V [Bene 98, Hapk 00, Frah 06, Mair 07, Vdov 07] and II-VI [Ruth 08b] quantum dots, the situation is somewhat different.

Let us assume an RTD with a single self-assembled quantum dot sandwiched between two tunnel barriers. Furthermore, the eigenenergy of the dot state is just above the Fermi energy of the emitter electrons, and no resonant tunneling process through the quantum dot state is possible. For simplicity, we omit the contribution of electrons, which tunnel through both barriers off resonance. An increase of the bias voltage across the double

barriers lowers the quantum dot state with respect to the conduction band of the emitter. Aligning the quantum dot state with the emitter Fermi sea creates a resonant transport channel that allows electrons to traverse the double barrier system.

Since the collector Fermi sea is lowered even further than the quantum dot state, its presence can be neglected, especially as soon as the bias voltage exceeds the bandwidth of the emitter states. The problem thus reduces to the emitter Fermi sea and the dot state sandwiched between the double barriers.

The charging energy of a self-assembled quantum dots is very likely much greater than the bandwidth of the emitter electrons. Thus only one additional electron can occupy the dot at the same time during the resonant tunneling process. Tunneling one electron at a time, there are two possible configurations for the system. In configuration A, an electron is occupying the dot and no impurity of positive charge is present in the system. As soon as the electron tunnels into the collector, it leaves behind an unoccupied positively charged state that acts as a Coulomb potential (configuration B). As current is flowing through the self-assembled dot state, the electrons in the emitter are thus exposed to a fluctuating charge. While the Coulomb interaction between the tunneling electron and the hole left behind in the dot will enhance the tunneling current, the shakeup of the Fermi sea due to the fast scatterer switching (configurations  $A \leftrightarrow B$ ) suppresses this enhancement. Figure 6.1a shows a schematic of these processes, while fig. 6.1b depicts an idealized I-V characteristic for temperatures close to  $T=0$  K. In addition to the step-like dependence for conventional 2D-0D resonant tunneling shown as the blue line of fig. 6.1b, the many-body enhancement (red line) results in a very sharp additional feature if the quantum dot state is aligned with the Fermi energy in the emitter.

As the FES is one of few simplest many-body effects with an exact solution, it provides a promising starting point for the research on nonequilibrium physics in many body systems [Braun 03, Aban 05]. Here we show that the I-V characteristics of an RTD containing self-assembled CdSe quantum dots still reflects the characteristics of a conventional thermally broadened FES problem at fairly large bias voltages. As discussed in [Frah 06], non-equilibrium effects can however be described by an effective temperature, broadening the FES.

## 6.2 Measurement and analysis

Our device is a molecular beam epitaxy (MBE) grown all-II-VI semiconductor RTD with an active region consisting of a  $\text{Zn}_{0.7}\text{Be}_{0.3}\text{Se}$  tunnel barrier with embedded self assembled CdSe quantum dots. Because of the lattice mismatch between the CdSe and the barrier material, the growth of 1.3 monolayers of CdSe into the middle of the barrier induces a strain build up. Relaxation of this strain results in the formation of quantum dots. Emitter and collector are gradient n-type doped, with an undoped spacer layer next to the barriers and a high doping concentration ( $10^{19} \text{ cm}^{-3}$ ) at the contact layer to allow the

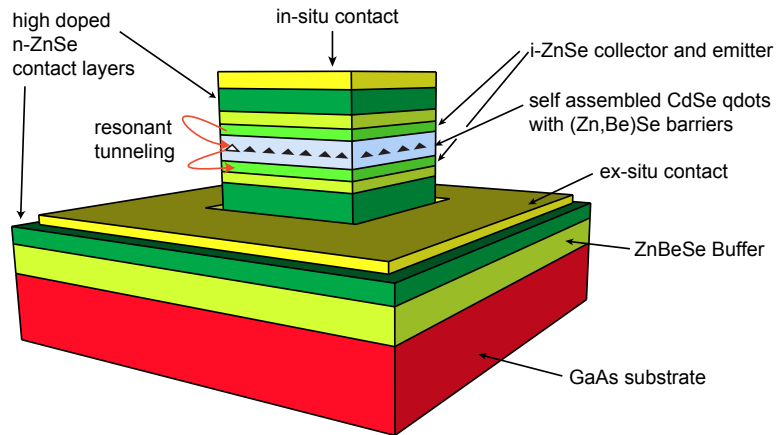


**Figure 6.2:** Device layout and layer structure. Self assembled quantum dots which are embedded in the (Zn,Be)Se tunnel barrier provide the resonant state for the tunneling transport mechanism.

formation of ohmic contacts at the metal-semiconductor interface. The layer structure and the device layout are shown in fig. 6.2. In order to allow for transport measurements vertically through the layer stack, standard optical lithography techniques are used to pattern  $10 \times 10 \mu\text{m}^2$  square pillars, and contacts are applied to the bottom and top ZnSe layers. The contact on top of the RTD pillar is deposited immediately after growth by transferring the sample to a ultra-high-vacuum metallization chamber without breaking the vacuum. It has ohmic behavior and a contact resistance on the order of  $10^{-3} \Omega\text{cm}^2$  as determined by stripline measurements on calibration samples. Bottom contacts must be deposited ex-situ after processing the pillar and thus have higher resistivity which is compensated in our device by the larger area ( $500^2 \mu\text{m}^2$ ) of these contacts. Although for the size of our pillar one expects some ten thousand self assembled quantum dots in each device, transport through self assembled quantum dot RTDs at lower bias voltages is usually dominated by only a few dots that have resonant levels at relatively low energies and/or at weak spots in the barriers [Hill 01, Vdov 00, Pata 02, Itsk 96, Hapk 00]. Therefore a resonant feature at low bias is characteristic of resonant tunneling from the injector through a single self assembled quantum dot into the collector.

Figure 6.3 shows the  $I(V_D)$  characteristic of our sample at 4.2 K in zero magnetic field and under forward bias (the top of the pillar being defined as ground). At bias voltages above 300 mV, the current shows many resonance-peaks superimposed on the normal background. These originate from the ensemble of quantum dots in the structure. The inset shows the first resonant feature of our device at 250 mV which is separated by approximately 60 mV from the next visible resonance. The shape of this feature is clearly suggestive of FES behavior [Matv 92, Geim 94, Frah 06]. The FES causes an additional flow of electrons on resonance with the emitter Fermi level. This enhancement decays as a power law with increasing bias voltage [Matv 92]. At 1.6 K, it has a maximum value of



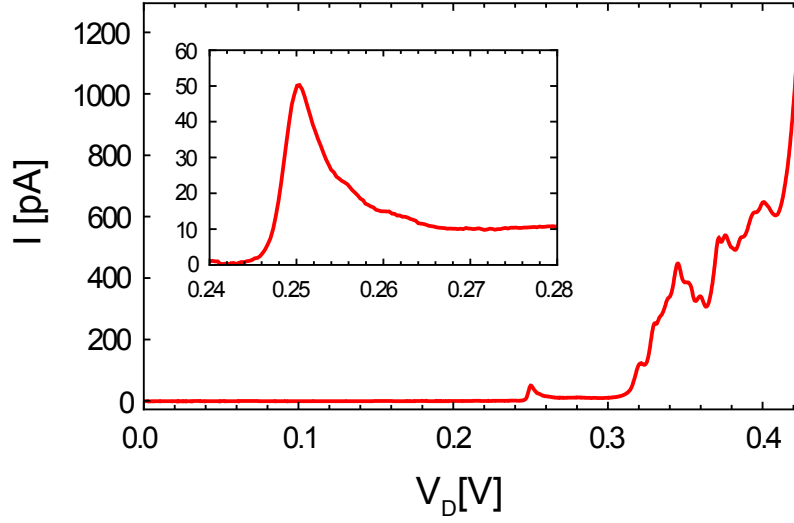


**Figure 6.3:** Forward bias  $I(V_D)$  characteristic at 4.2 K and zero magnetic field. The inset shows a magnification of the first peak, at 250 mV, which has the shape of a Fermi edge singularity enhanced resonance.

seven times the current flowing at higher biases (say 30 mV after the resonance onset), where many particle effects are negligible.

Figure 6.4(a) illustrates the temperature dependence of the I-V characteristics. The resonant feature survives to high temperature with the current enhancement decreasing by only a factor of 4.7 from 2 to 45 K. As observed before in III-V devices [Vdov 07], the maximum current of the FES enhanced resonance decays with increased temperature according to a power law. We fit the results using the temperature dependent modeling developed by Frahm et al. for a FES enhanced resonant tunneling current through a self

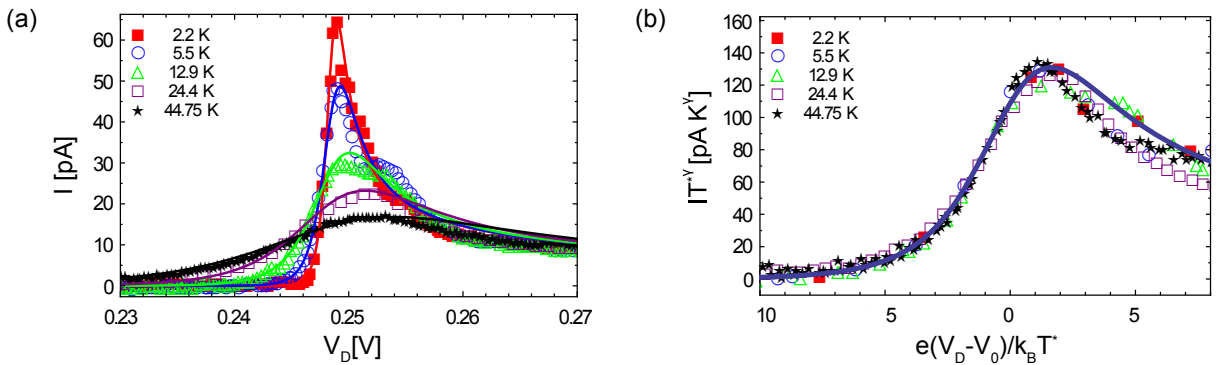


**Figure 6.4:** (a)  $I(V_D)$  characteristics for various temperatures up to 45 K and at zero magnetic field. Symbols are the experimental data. The colored line for each data set represents a fit to equation 6.1 for each temperature. (b) Rescaling both axes collapses the data sets for all temperatures on a single scaling curve. The solid line is a fit to the rescaled equation 6.1 which is now independent of the effective temperature  $T^*$ .

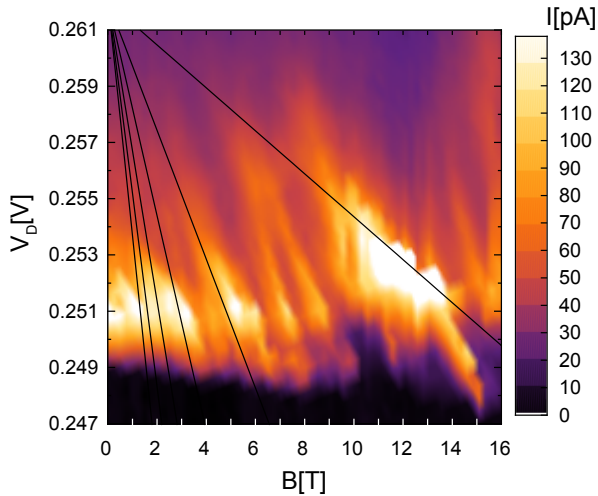


**Figure 6.5:** Current as a function of bias voltage and magnetic field perpendicular to the layer stack at 25 mK. Several field dependent resonance features are observed.

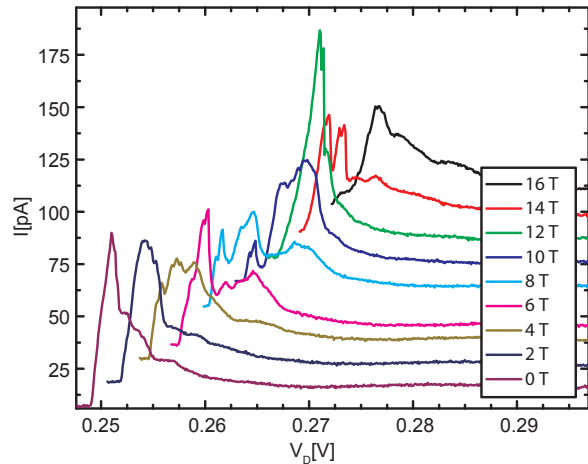


**Figure 6.6:**  $I(V_D)$  characteristics for various magnetic fields at 25 mK. An additional fine structure on the classical Fermi edge singularity can be resolved (The curves are offset by 3 mV and 11 pA for clarity).

assembled InAs quantum dot [Frah 06]. The tunneling current is given by

$$I(V_D, T^*) \propto \frac{1}{\pi} \text{Im} \left[ \left( \frac{iD}{\pi k_B T^*} \right)^\gamma B \left( \frac{1-\gamma}{2} - i \frac{\alpha(V_D - V_0)e}{2\pi k_B T^*}, \gamma \right) \right] \quad (6.1)$$

with a lever arm  $\alpha = 0.4$ , the characteristic cutoff parameter  $D$  of the order of the bandwidth and the edge-exponent  $\gamma$ .  $B$  represents the Beta-function. An effective Temperature  $k_B T^* = \sqrt{(kT)^2 + \Gamma_i^2}$  is used to account for the effect of the intrinsic line width  $\Gamma_i$  of the participating quantum dot state. As shown experimentally in fig. 6.4(b), and consistent with equation (6.1), the  $I(V_D)$  curves taken at various temperatures collapse to a common curve after rescaling voltage and current axes with  $V_D \rightarrow e(V_D - V_0)/k_B T^*$  and  $I \rightarrow IT^{*\gamma}$ , where the Fermi-edge exponent  $\gamma = 0.54$  and the intrinsic bandwidth  $\Gamma_i = 0.25$  meV are used as fitting parameters. The model agrees with experiment, with only a slight deviation at higher bias voltages, which probably stems from a small thermal drift during measurement.

The current of a FES enhanced tunneling process is influenced by magnetic field [Frah 06, Vdov 07, Hapk 00]. Figure 6.5 shows transport measurements at 25 mK in various magnetic fields perpendicular to the layer stack, which clearly shows Landau fan like structure.

In general, this structure could result from electronic states either in the emitter or in the dot. If it was related to the quantum dot, well known Darwin-Fock behavior would lead to an increase of the energy of the resonant Landau levels with increasing magnetic field, which is in stark contrast to the observations of fig. 6.5. Thus we conclude that the

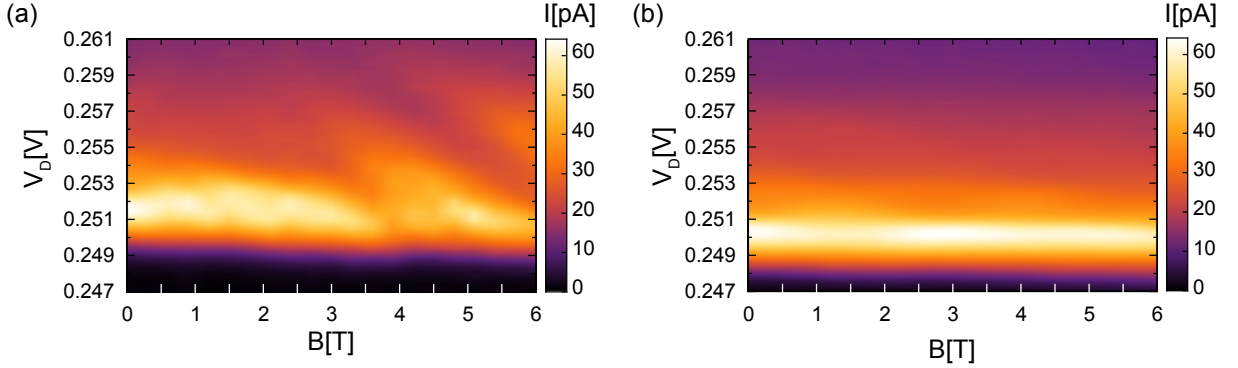


**Figure 6.7:** The additional Landau-like Structure in a magnetic field perpendicular to the layer stack is shown in a) and disappears completely for an in-plane magnetic field configuration (b).

magnetic field dependence of all features is dominated by the emitter states, which gain energy with magnetic field and thus reduce the peak position of each feature.

The black lines in fig. 6.5 represent an emitter Landau fan, calculated assuming a bulk ZnSe effective mass  $m \approx 0.18m_e$  and the same lever arm determined by the previous fit at zero magnetic field. Many important features are fitted by the Landau fan, however some additional field dependent features that are present cannot be explained by using only this one Landau fan or by including the Darwin-Fock like behavior of the quantum dot level.

Resonant tunneling transport showing magnetic properties of the emitter layer, where all main features could be explained by one Landau fan, has been observed in a III-V device with self assembled InAs quantum dots and a high quality two dimensional electron gas (2DEG) as emitter [Main 98]. We suggest that in our device we measure a 2D-like disordered emitter which results in various additional resonance signals in the energy-magnetic field plane due to a more complicated density of state structure in the emitter. These additional features cannot be attributed to a second dot or an additional dot level. In that case, one would expect two resonant features for each emitter Landau level, separated by an almost constant voltage offset. It is however not possible to match the data with two such Landau fans. Moreover a second dot should show a clearly visible feature at zero magnetic field, but none is observed (see fig. 6.3). Figure 6.7 shows direct evidence of the 2D characteristics of the emitter. While in fig. 6.7a the Landau structure is visible for the perpendicular magnetic field configuration, it vanishes for the measurements in in-plane magnetic field shown in fig. 6.7b.

While the model of equation (6.1) correctly describes the shape of the Fermi edge singularity at temperatures above 1 K, measurements at 25 mK (fig. 6.5) reveal additional fine structure which is not explained within this model. To emphasize the nature of this fine structure,  $I(V_D)$  characteristics for some of the measured magnetic fields from fig. 6.5 are plotted in fig. 6.6. This fine structure may result from properties of the emitter. A generalized approach to the FES problem shows that backscattering in the contacts

may have an effect on the FES exponent [Aban 04]. In our case, back scattering within the disordered emitter is a function of the applied bias voltage and produces additional structure on the FES enhanced tunneling current. This could result from characteristics of the local geometry near the dot or local density fluctuations in the disordered-metal-like emitter [Schm 01].

In summary, we have observed a Fermi edge singularity in tunneling from an intrinsic ZnSe injector through a self assembled CdSe quantum dot state. Above 1 K and at zero magnetic field, the behavior of the Fermi edge enhancement is consistent with previous observations in III-V devices, and consistent with conventional theory. At lower temperatures or in a magnetic field, additional enhancement effects are observed, and are suggestive of backscattering associated with local effects near the dot. This detailed characterization of Fermi edge singularity in the II-VI material system thus provides supplementary data against which modern theories of Fermi edge enhanced transport can be tested.

# Chapter 7

## Simultaneous strong coupling of a self-assembled quantum dot to a Fermionic and a Bosonic bath

As shown in chapter 6, the presence of a zero dimensional state can lead to a strong enhancement of the resonant tunneling current when the quantum dot state is aligned with the Fermi energy of the emitter electrons. While this enhancement stems from the coupling of the resonant state to the Fermionic bath in the emitter, a second kind of many particle effect was previously demonstrated for a quantum dot state coupled to a dilute magnetic spin system [Goul 06]. The observed remanent zero field splitting in the I-V characteristics stems from the formation of BMP-like states. These two manifestations of many particle effects have previously only been demonstrated independently. Here we show an optimized structure yielding both enhancements simultaneously in the transport measurements through a single magnetic quantum dot state.

### 7.1 Quantum dot coupled to its Mn doped environment

To create a magnetic environment for the self-assembled CdSe quantum dots, magnetic Mn dopants are added to the (Zn,Be)Se tunnel barriers. As these quantum dots form due to the lattice mismatch between the CdSe monolayer and the barrier material, the shape, the size as well as the overall distribution of the self assembled quantum dots are likely to differ in systems with magnetic tunnel barriers from those lacking the magnetic dopants.

Figure 7.1 illustrates a crosscut of the double barrier region of such a magnetic self-assembled quantum dot RTD, showing only one CdSe quantum dot for simplicity. The shaded area depicts the overlap of the quantum dot wave function with the Mn atoms in its vicinity. Despite the lack of long range magnetic order [Twar 84] in dilute (Zn,Mn)Se, BMPs form in the vicinity of a single electron/hole state [Diet 82].

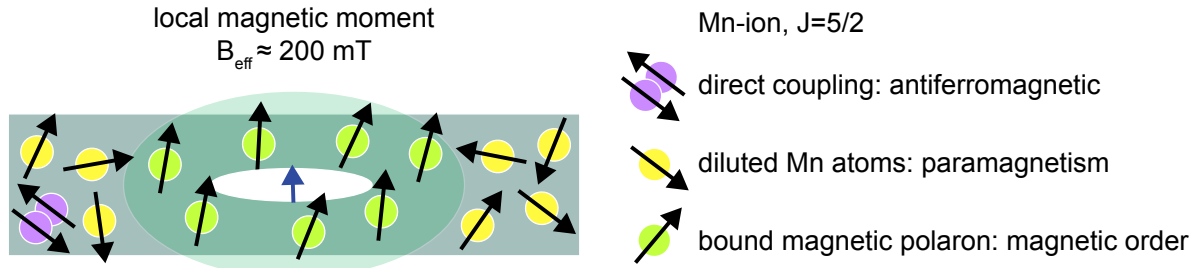


**Figure 7.1:** Schematic of the microscopic magnetic ordering in the vicinity of a self-assembled CdSe quantum dot. While the bulk (Zn,Mn)Se material is paramagnetic, due to the presence of the zero dimensional state a local magnetic order forms, lifting the degeneracy of the quantum dot state without the need for an external magnetic field.

These systems are known to be governed by two temperature regimes. For low temperatures, where  $k_B T$  is smaller than the s-d exchange energy  $E_{s-d}$  of the BMP, it is favorable for the BMP state to align the Mn spins that overlap with the quantum dot wave function along the spin of the quantum dot state. A ferromagnetic microscopic order thus forms in the vicinity of the quantum dot, lifting the degeneracy of the quantum dot state. In transport, this splitting is observed as two distinct resonant tunneling peaks in the I-V characteristic of such a device. As  $k_B T$  exceeds  $E_{s-d}$ , the local magnetization is reduced but remains finite, despite of the lack of correlation between the Mn spins. This stems from the reduced number of Mn spins involved in this process, as the thermodynamic fluctuation of the magnetization will also yield a finite spin splitting for a sufficiently small number of spins.

The effective zero magnetic field splitting which is observed in our quantum dot systems is thus a combined effect of the s-d coupling of the electron wave function on the quantum dot to the d orbital spins of the Mn atoms and the thermodynamic fluctuations of the Mn spin cloud in the vicinity of the quantum dot. For a more detailed discussion of the BMP see references [Diet 82, Diet 83, Diet 86, Isaa 88, Herb 98].

## 7.2 Quantum dot coupled to both baths

A single spin state coupled to both a fermionic bath and a bosonic bath is currently under considerable interest since these systems can be used to access a quantum critical point [Kirc 05, Kirc 08a, Kirc 08b]. Here we show an experimental realization of such a system.

Figure 7.2a shows the I-V characteristic of a DMS SAD RTD with one monolayer of CdSe sandwiched between two  $\text{Zn}_{0.66}\text{Be}_{0.3}\text{Mn}_{0.04}\text{Se}$  barriers of 5.6 nm thickness at  $T=20$  mK and  $B = 0$  T. Only at negative bias voltages, the I-V characteristic is suggestive of an FES enhancement of the resonances, while for the positive bias voltages both features merely show a step in the I-V characteristics. That this enhancement only occurs at negative bias voltage is due to the asymmetry of the double barrier region. As is clear

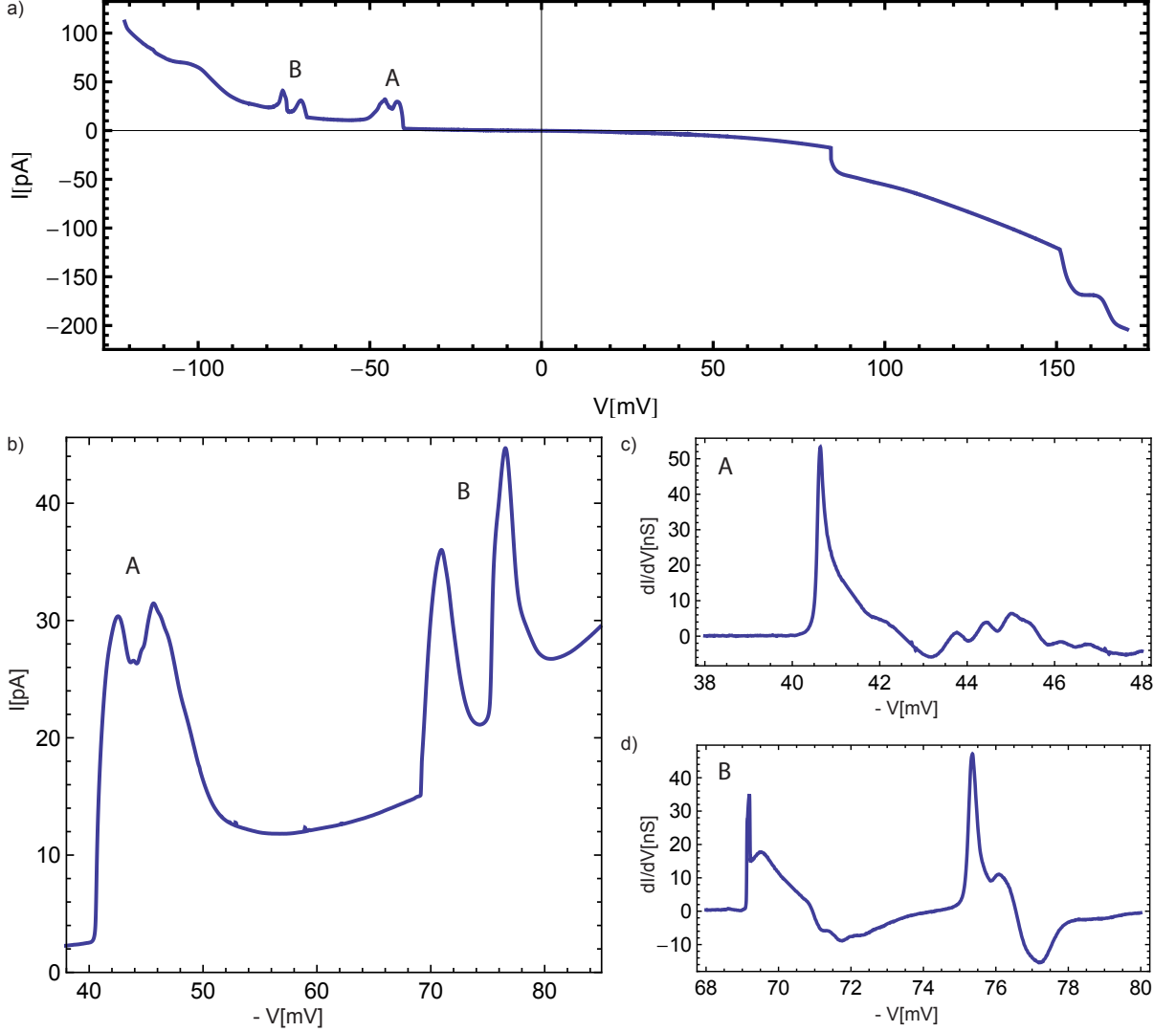


**Figure 7.2:** a) I-V characteristics at  $\approx 20$  mK and  $B = 0$  T of a SAD RTD with magnetic impurities incorporated in the tunneling barriers. Both features show a remanent zero field splitting of the spin-up and down peak. b)+c)  $dI/dV$  characteristics for features A and B, respectively. Both plots emphasize the apparent additional structure on the resonant tunneling current traversing the quantum dots.

from fig. 7.2a, a different bias voltage is required to bring feature A into resonance than for feature A'. In section 2.4 we have discussed the lever arms of an RTD and the influence of contact resistances. In the SAD RTDs with an on-peak resistance in the order of  $M\Omega$  to  $G\Omega$ , contact resistances are approximately four to five orders of magnitude lower and only result in small corrections to the lever arms. In the following we thus assume that

$$\frac{1}{l_-} + \frac{1}{l_+} \approx \alpha_- + \alpha_+ = 1 \quad (7.1)$$

where  $\alpha_-$  and  $\alpha_+$  are (inverted) lever arms descriptive of the upper and lower tunnel

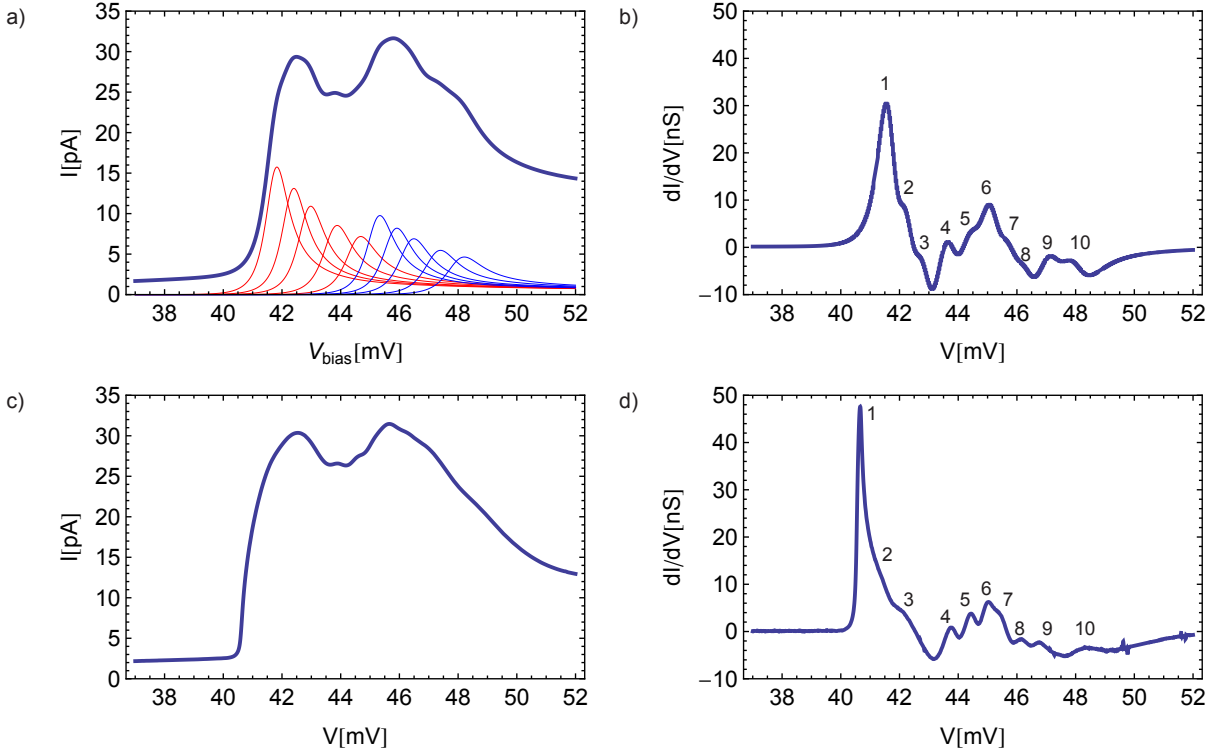


**Figure 7.3:** I-V characteristic at  $T=20$  mK and  $B=0$  T from the model (a) and the experimental data (c). The various contributions for spin-up (down) transport channels are shown as red (blue) lines below the modeled curve. The apparent fine structure is best seen in the first derivative. Features arising from the various channels and are labeled accordingly from low to high bias voltages for both the experimental (b) and model (d) data.

barrier, respectively. The energetic distance  $E_0$  of each resonant state to the Fermi sea at  $V = 0$  V reads  $E_0 = \alpha_- V_- = \alpha_+ V_+$ , where  $V_-$  and  $V_+$  are the negative and positive bias voltages required to align a resonant state with the emitter Fermi energy. These lever arms thus relate via

$$\frac{\alpha_+}{\alpha_-} = \frac{V_-}{V_+} \quad (7.2)$$

and from equations (7.1) and (7.2) we find  $\alpha_- = 0.68$ . The enhancement of the tunneling rate is thus only seen for tunneling into the quantum dot state through the thicker tunnel barrier. A similar experiment on an RTD containing InAs quantum dots also only shows the FES enhancement while loading the dot through the thicker tunnel barrier, while for the opposite tunneling direction, only a current step without additional enhancement occurs [Vdov 07].

A magnification of the two apparent pairs of resonance-peaks at  $-45$  mV (feature A) and  $-75$  mV (feature B) is shown in 7.2b. Both feature A and B show a remanent zero field splitting of the spin-up and spin-down resonances of  $5.6$  mV and  $9.2$  mV, respectively. The apparent fine structure on both feature A and B suggests that the resonance-peak is



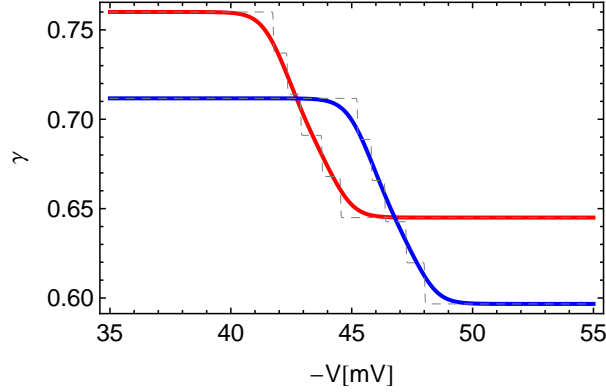


**Figure 7.4:** Bias voltage dependence of the Fermi-edge exponents for spin-up (red) and spin-down (blue) electrons as used in the model. The dashed gray lines depict the curve for  $T \rightarrow 0$  K, where each vertical steps is the amplitude of the phase loss  $d\gamma$  per additional conducting transport channel. The intrinsic line width  $\Gamma_i$  is used as the temperature scale for the broadening of the red and blue curve.

comprised of more than one tunneling contribution. Plotting  $dI/dV$  in fig. 7.2b+c gives further support to this assumption, as it clearly reveals the fine structure on the higher bias voltage tails of the resonance-peaks.

This fine structure however is of different character than the one seen for the FES in the non-magnetic quantum dot (see fig. 6.6) and was also never seen in such a magnetic quantum dot RTD without an apparent FES enhancement.

Furthermore, this fine structure is clearly observed at zero magnetic field and cannot be caused by Landau level quantization effects. We thus argue that it originates from the simultaneous observation of both many body correlation effects (FES and BMP) on the same quantum dot. Figure 7.3c shows a further magnification of feature A at  $B=0$  T and  $T=20$  mK while 7.3d again plots its derivative. Even though it exhibits a complex fine structure, it still has some resemblance with the I-V characteristics of an FES enhanced resonance-peak. The sharp onset as well as the characteristic high bias voltage tail are still clearly observed, and the overall shape suggests that feature A is comprised of a superposition of several FES-like contributions. In fig. 7.3a, we present a modeled I-V characteristic employing the aforementioned observations. The red (blue) curves are contributions from various FES enhanced spin-up (spin-down) transport channels. The I-V characteristics of each transport channel are given by equation (6.1) with the above determined lever arm  $\alpha_-$  and an intrinsic quantum dot width of  $\Gamma_i=0.4$  meV. Each of the additional resonance-peaks occurring at increased bias voltages has a reduced amplitude, stemming from a reduction of the Fermi-edge exponent  $\gamma$ .

The  $dI/dV$  plot of the experimental data in fig. 7.3d suggests a total of ten transport channels. We thus assume four additional excited states on top of the spin-up and spin-down states. The apparent fine structure is labeled from 1-10 in order to compare to the  $dI/dV$  plot of the modeled data in fig. 7.3b.

For the FES previously discussed in chapter 6 only one transport channel is present and a constant  $\gamma$  is assumed for the complete bias voltage range. Here we however observe several transport channels, and the assumptions made for equation (6.1) break down. As soon as the spectral density of the quantum dot state shows several maxima instead of a single sharp spectral line, a distinct electron energy is no longer singled out by the resonant tunneling process. For the first resonance-peak at approximately 42 mV, we assume a Fermi-edge exponent of  $\gamma_0^\uparrow=0.76$ . As the bias voltage is increased, the next transport channel is aligned with the Fermi energy  $E_F$  of the emitter, resulting in a second FES enhancement. However the resonant level causing the first FES enhancement is still aligned with the emitter states, but at an energy below  $E_F$ . The dot can only accommodate one additional electron due to a charging energy much bigger than the sub meV level spacing of these transport channels. Electrons thus tunnel one at a time through either one of the states currently aligned with the emitter Fermi sea. One can think of the tunneling process through the lower state as an additional perturbation to the FES enhancement of the state currently aligned with the Fermi-edge, effectively reducing the enhancement of its tunneling rate. We simply assume that each additional channel will result in a reduction  $d\gamma=0.023$  of the Fermi-edge exponent  $\gamma$ . The resulting voltage dependence of  $\gamma$  thus reflects the spectrum of the quantum dot and is plotted in fig. 7.4 for the two spin types as the dashed gray lines. This however lacks a description for the broadening of the quantum dot spectrum due to the intrinsic line width  $\Gamma_i$  of each channel. Assuming a constant line width for all transport channels, the bias voltage dependence of  $\gamma$  reads

$$\gamma(V) = \gamma_0 - \sum_{E_i}^N \frac{d\gamma}{1 + \exp\left[-\frac{V-E_i/\alpha}{\Gamma_i}\right]} \quad (7.3)$$

Equation (7.3) is plotted in fig. 7.4 for both spin-up (red curve) and spin-down (blue curve) Fermi-edge exponents, with  $\gamma_0^\downarrow=0.71$ .

To further test our model, we investigate the temperature dependence of feature A. Figure 7.5a shows transport measurements on feature A at temperatures from 8 mK to 20 K. These measurements are suggestive of a characteristic threshold temperature in this system. Figure 7.5b shows a magnification of the resonance-peak maxima for temperatures up to  $\approx 770$  mK. The impact of an increase in temperature below 770 mK is small and there are only minor changes to the amplitudes of the individual features of the fine structure. The onset of the first resonance-peak in fig. 7.5a is nevertheless slightly broadened, indicating an increase in the electron temperature of the emitter Fermi sea. For temperatures from 1.3 K to 20 K (fig. 7.5c), temperature however massively broadens the I-V characteristics.

Figure 7.5d shows modeled I-V characteristics using the same parameters as in fig. 7.3a, but for the various temperatures of the experimental data in fig. 7.5a. As is clear from fig. 7.5e+f, the model data also shows no change for the low temperature range, as

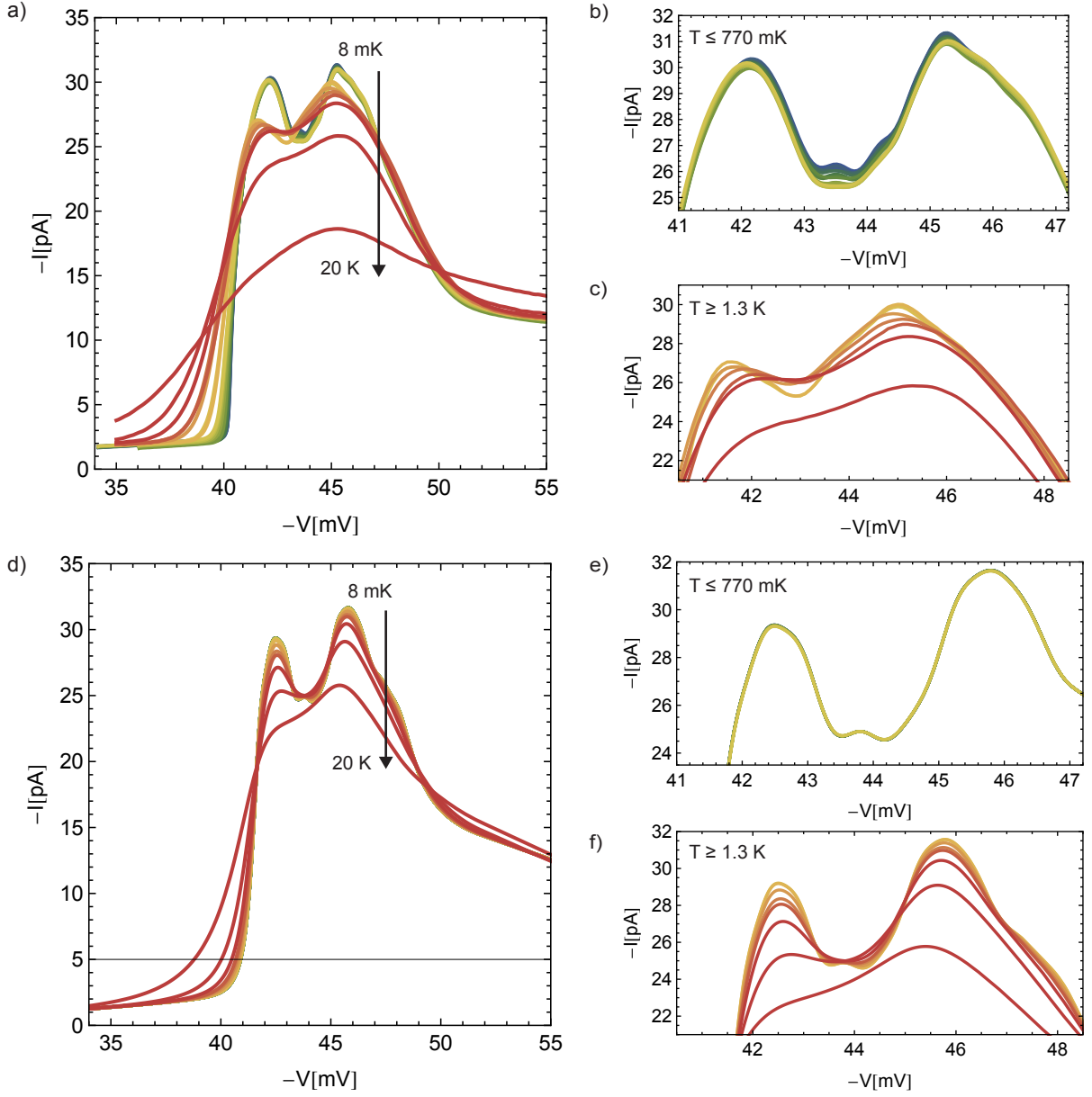


**Figure 7.5:** a) I-V characteristics of feature A for temperatures from 8 mK to 20 K b) magnification of the I-V characteristics at the peak maxima for temperatures up to 770 mK c) as in b), but for temperatures from 1.3 K to 20 K d)-f) The same plots as in a)-c) but from the model presented in fig. 7.3a, evaluated for the same temperatures as in the experimental data.

the intrinsic line width  $\Gamma_i > k_B T$  sets a lower limit for the finesse of the features. As soon as  $k_B T$  however is of the same order as  $\Gamma_i$ , the I-V characteristics are further broadened by an increase in temperature.

For a single transport channel as in chapter 6, the maximum of the resonance-peak shifts to higher bias voltages for elevated temperatures. In the apparent transition between the two temperature ranges of fig. 7.5a, both resonance-peak maxima however shift to

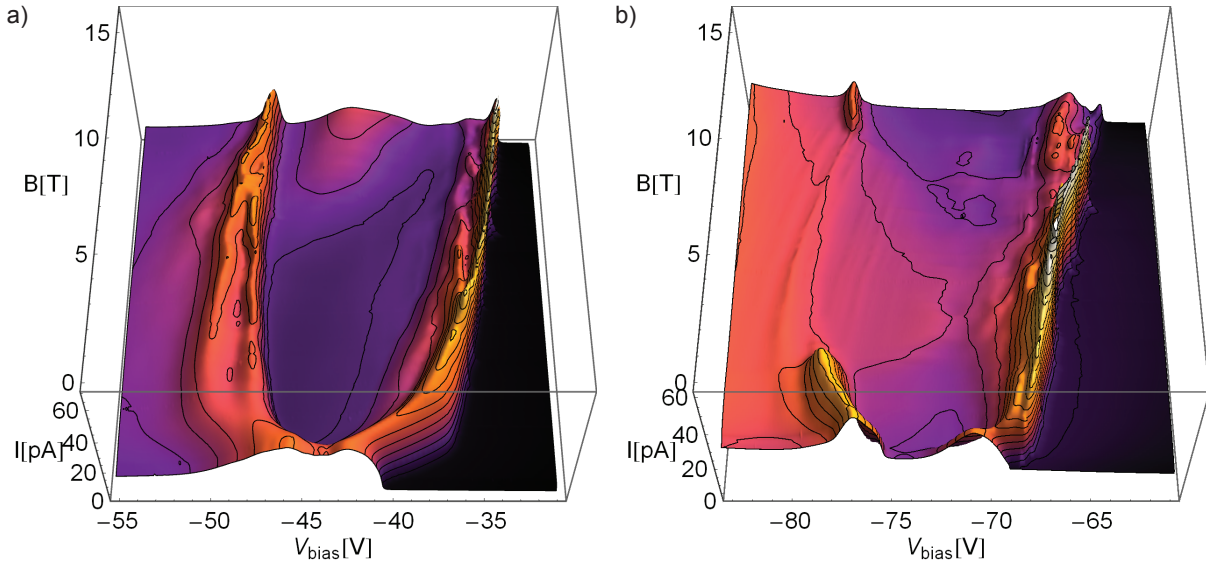


**Figure 7.6:** I-V-B characteristics at 20 mK of a dilute magnetic quantum dot for magnetic fields from 0 to 16 T applied vertical to the layer stack. a) feature A b) feature B

lower bias voltages. As all transport channels have different Fermi-edge exponents they exhibit different changes to their amplitudes due to an increase in temperature. While the resulting superposition of these transport channels accounts for an overall shift to lower negative bias voltages as shown in fig. 7.5d-f, the shift of the sharp feature at  $\approx -42$  mV and the sudden drop in the amplitude thereof between the two temperature ranges is not yet reproduced by our model. In our model we assume a constant splitting of the spin-up and spin-down channels. The remaining discrepancy between our model and the experimental data thus probably stems from not including the temperature dependence of the BMP state [Herb 98].

Due to the giant Zeeman effect, the influence of the external magnetic field on the spectrum of the magnetic quantum dot should be much more pronounced than any influence on the emitter states. While the FES enhancement is known to show strong magnetic field dependence as well [Vdov 07], it should not result in additional structure in I-V-B measurements, merely in changes to the amplitude of a FES enhanced transport channel. As these contributions are highly asymmetric, their superposition will however change its appearance if their feedback to the magnetic field differs from each other.

Figures 7.6a+b show transport measurements at 20 mK in magnetic fields perpendicular to the layer stack from 0 to 16 T for features A and B, respectively. The afore discussed fine structure is clearly observed on both feature A and B while sweeping the external magnetic field, as both the level splitting and the respective amplitude of the particular contributions to the resonance-peaks change.

Feature A shows a similar magnetic field dependence as the previously observed remanent zero field splitting in II-VI DMS SAD RTDs [Goul 06] modulo the apparent fine structure. The apparent sawtooth pattern on the fine structure probably stems from a

Fock-Darwin like spectrum of the quantum dot system in the perpendicular external magnetic field [Fock 28, Taru 96]. It should be noted that in our DMS quantum dot system, the contribution of the giant Zeeman splitting to the eigenenergy of the resonant tunneling state needs to be considered, resulting in a quite different pattern than for a conventional Fock-Darwin spectrum. A broad additional peak emerges between the spin-up and spin-down resonance-peaks at magnetic fields above  $B=10\text{T}$  and continuously grows while increasing the perpendicular magnetic field to  $B=16\text{T}$ . The origin of the latter remains however unclear. Effects like Kondo screening suggest themselves, where an additional channel forms between two quantum dot states due to spin screening effects.

The I-V-B measurements of feature B are remarkably different than those of feature A. As discussed above, feature B exhibits a much bigger remanent zero field splitting. In the BMP picture, this splitting of the spin-up and spin-down state depends amongst other things on the number of Mn atoms within the extend of the quantum dot wave function. It thus depends on the Mn distribution in the vicinity of the dot and the shape of its wave function, both of which are likely different for features A and B if we assign each of them to a different quantum dot.

For a better comparison of the magnetic field dependence of features A and B and its fine structure in particular, fig. 7.7 plots  $dI/dV$  as a function of the applied bias voltage and the external magnetic field. Figures 7.7a+b plot  $dI/dV$ -V-B in magnetic fields perpendicular to the layer stack (parallel to the current) for features A and B, respectively. As we have seen for the non magnetic quantum dot in chapter 6, the perpendicular magnetic field configuration can result in a fan like structure due to emitter Landau levels. A perpendicular field also causes the aforementioned Fock-Darwin energy spectrum on a disk-shaped quantum dot, to which we attribute the sawtooth pattern observed in fig. 7.7a.

In order to discriminate these effects from the ones caused by the magnetic vicinity of the dot, we plot  $dI/dV$ -V-B in an in-plane configuration in fig. 7.7c+d for features A and B, respectively. Both the sawtooth pattern and the additional tilt to the Brillouin like behavior are no longer observed for a magnetic field in the plane of the layer stack. The additional fine structure is however still clearly observed on both features.

The most striking difference between figs 7.6a and b is the suppression of the spin-down resonance for external magnetic fields between 3 and 14 T. This suppression of the spin-down transport channel of feature B is however not observed in parallel magnetic field configuration (fig. 7.6d), suggesting that it was also caused by the crossing of Fock-Darwin states with different angular momentum quantum numbers. For example in an perpendicular magnetic field, increasing the magnetic field above  $B=3\text{T}$  lowers a p-type state below the afore occupied s-type state, thus changing the wave function of the resonant state. The overlap between the quantum dot wave function and the emitter electrons is massively reduced and the resonance is damped. For magnetic fields above 14 T, the situation is however reversed and tunneling again occurs through an s-type state with a comparable amplitude to the  $B=3\text{T}$  case.

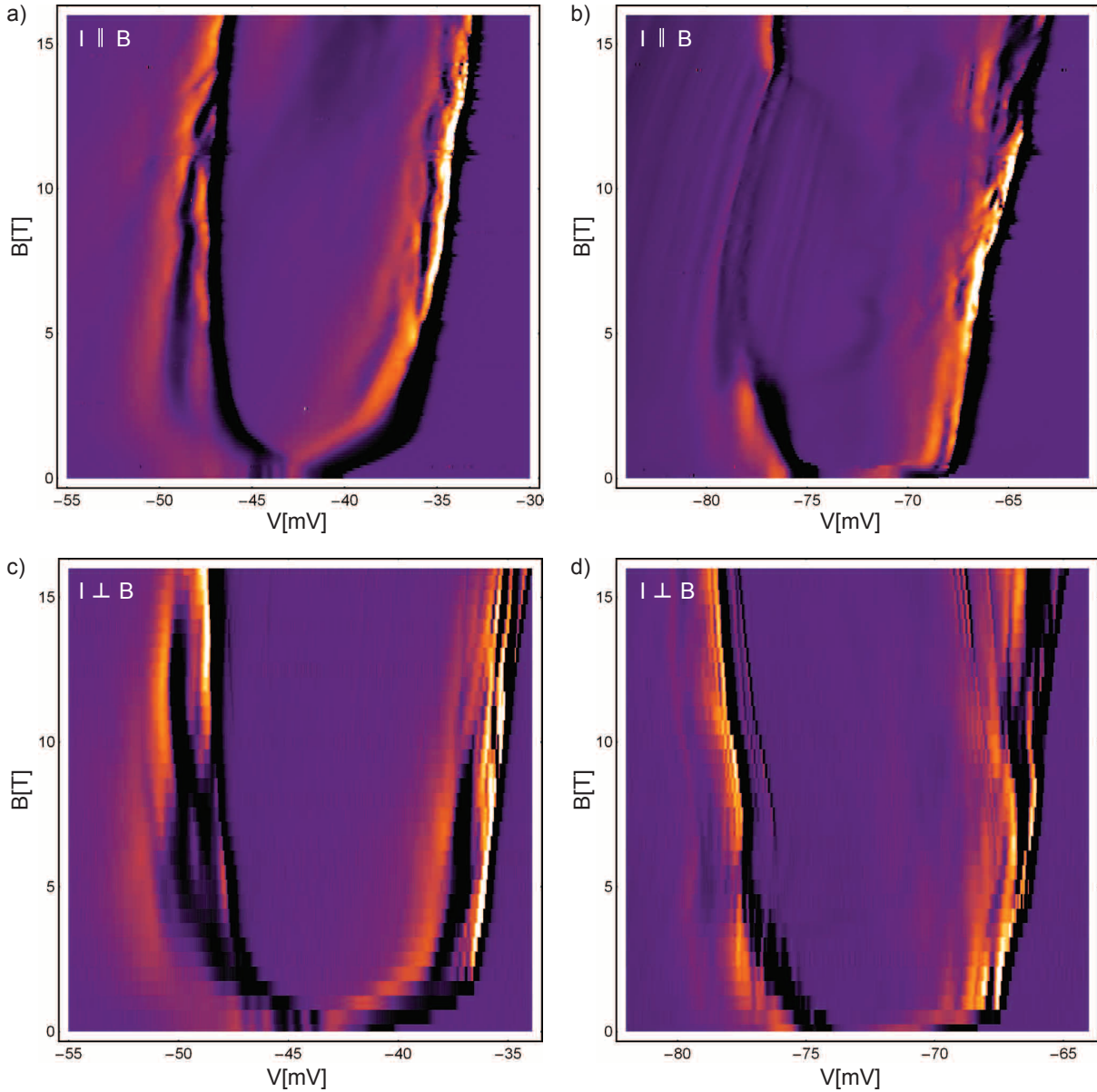


**Figure 7.7:** a)+b)  $dI/dV$ - $V$ - $B$  characteristic at  $T=20$  mK for an external magnetic field parallel to the current (perpendicular to the layer stack) for features A and B, respectively. c)+d) The same measurements as in a)+b), but in an in-plane magnetic field.

Following the magnetic field dependence of the main feature in fig. 7.7d at higher bias voltages, its onset bias voltage is highly suggestive of an additional contribution to the local magnetization by the breakup of antiferromagnetic Mn pairs within the BMP state [Shap 84]. All four measurements in fig. 7.6 show a more complex structure above these fields. These changes to the magnetic environment are thus likely important for a proper description of these systems at high magnetic fields and future theories can be tested on this additional effect. The breakup of these pairs will effectively increase the number of Mn spins contributing to the BMP state. A proper theoretical description should thus

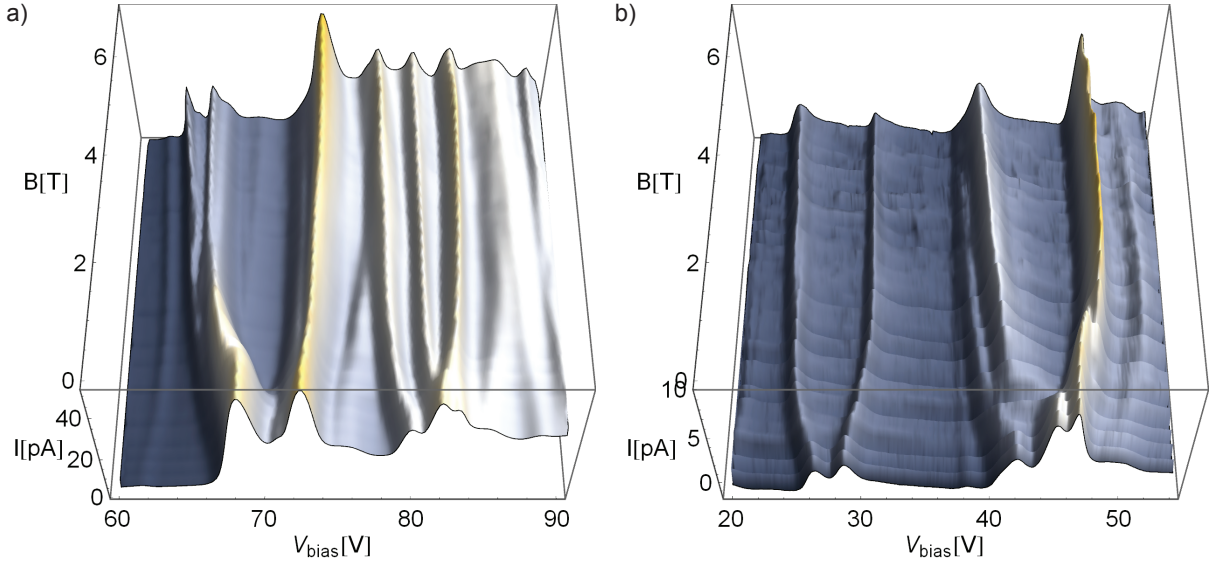


**Figure 7.8:** a) I-V-B measurement for a DMS SAD RTD, showing parallel transport through distinct resonant states. The magnetic field dependence of the I-V characteristic is needed to determine whether the resonance-peaks originate from a single state or are superimposed features stemming from different quantum dots. b) A direct comparison of a single feature ( $\approx 28$  mV) to a superposition of two features ( $\approx 45$  mV).

be able to explain some of the differences between the measurements at intermediate and high magnetic fields, as this transition is likely to be explained by changing the number of Mn spins in the model.

The additional fine structure, which is present at all magnetic fields in the perpendicular and parallel field configurations, is most likely linked to the coupling of the quantum dot to the Mn spins in its vicinity. A detailed model of the BMP state shows an energy spectrum with a level spacing similar to the here observed fine structure [Herb 98].

It is likely that feature A and B differ due to a distinct amount of electrons occupying each quantum dot. Regarding the spacing of approximately 20 meV between feature A and B, the two features could very well originate from the same dot. Adding another electron to the  $N$  electron system of feature A will have a different resonant tunneling state with a different extent of its wave function. The BMP formed around this  $N+1$  quantum dot state therefore is likely to have different properties than the one seen in feature A, even though the Mn vicinity is the same.

### 7.3 A comparison of various magnetic dots

Figure 7.8 shows I-V-B measurements on a different DMS SAD RTD, however with the same nominal layer stack as for the device presented in the previous section. Growth conditions of the CdSe quantum dot layer were slightly altered to achieve a different kind of dot distribution. Here we give an overview on the variety of resonant features

obtained from a single DMS SAD RTD. In fig. 7.8a the pair of resonance-peaks at  $\approx 70$  mV looks promising at first, due to the apparent zero field splitting and the fine structure on the resonance-peak occurring at lower bias voltages. The resonance-peak occurring at higher bias voltages however overlaps with a different resonance. This overlap increases as both signals move in opposite directions while sweeping the external magnetic field. The study of a single strongly correlated system is already challenging, and the additional superposition of a second unrelated, equally complex signal renders these efforts essentially hopeless.

The various superimposed resonances above 75 mV in fig. 7.8a clearly stem from tunneling through various quantum dots. While one cannot clearly state that for a single I-V characteristic at any given field, the complete I-V-B measurement usually provides enough information to determine whether a feature is descriptive of tunneling through a single quantum dot or not. Figure 7.8b for example provides a perfect comparison of a feature descriptive of tunneling through a single quantum dot ( $\approx 28$  mV) to a feature which is most likely comprised of tunneling through two magnetic quantum dots and can be explained by the superposition of two Brillouin-like magnetic field dependencies.

In summary, we have investigated transport measurements on quantum dot systems exhibiting two kinds of many-body correlation effects simultaneously. Due to the sharp features that arise from the FES enhancement when the quantum dot is aligned with the emitter Fermi-edge, we observe fine-structure which is suggestive of a BMP excitation spectrum. The spectrum of the magnetic dot in a perpendicular magnetic field is furthermore suggestive of Fock-Darwin like behavior, which has a strong impact on the coupling to the emitter reservoir. A preliminary model is able to reproduce the overall shape of the I-V characteristic at  $B=0$  T and also yields quantitative agreement on the temperature dependence thereof. The data presented can be used to test future models, including an exact description of the multi channel FES due to the presence of the BMP state. Once such a theory is established, it can be used to test these systems for quantum critical behavior, yielding the necessary conditions for the experimental realization thereof.



## Chapter 8

# Resonant tunneling through a dilute magnetic self-assembled quantum dot near zero bias voltage

In the previous chapters we showed for the quantum well RTDs that the applied bias voltage needed to align the quantum well layer with the emitter Fermi sea effects the transport characteristics. Conventional theories for the afore discussed many body effects often assume quasi-equilibrium, where influences like the applied bias voltages are treated as small perturbations to the system.

In lateral quantum dots defined by gating a two dimensional GaAs/(Al,Ga)As electron gas [McEu 91], one has control over the energetic distance of the quantum dot states with respect to the emitter by means of a plunger gate [Kouw 21]. Also the gating of vertical RTDs containing self assembled InAs dots has been demonstrated successfully in the III-V material system, achieving a similar level of control [Aust 99]. Gating of vertical RTD structures in the ZnSe material system however is technologically challenging and is not discussed in this thesis, but the realization of the latter is currently under development by my colleague Gabriel Dengel.

As the gating effect on the resonant levels is limited, devices with resonant levels close to the emitter Fermi level are desirable. Assuming a proper gate efficiency, only small gate voltages are required to align the resonant states with the emitter. Using a small fixed bias voltage to drive the resonant current, such systems could for example be used to test theories on the nonequilibrium FES problem [Brau 03, Aban 05]. As discussed in chapter 6, coupling to the collector Fermi sea is challenging in our devices without lateral gates, as while we use the applied bias voltage to align the resonant quantum dot states with the emitter, the distance between the confined states and the collector Fermi sea is increased. Using a gate to lower the resonant level and a small fixed applied bias voltage, one could however sweep the resonant state through both Fermi energies.

Here we present a DMS SAD RTD where the lowest resonant level is located only  $\approx 1$

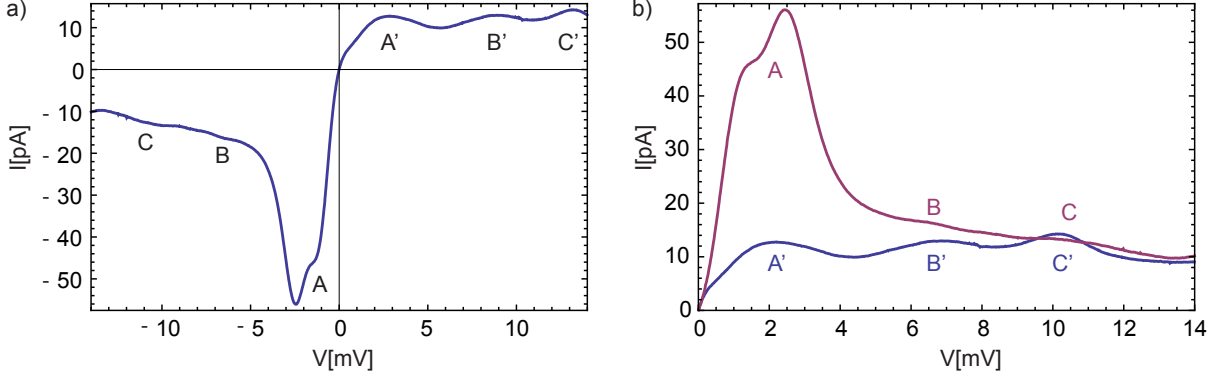


**Figure 8.1:** a) I-V characteristic at zero magnetic field. The first resonance for negative bias voltages is enhanced by a FES, while the same resonance shows no such effect for positive bias voltages. b) In order to compare the two ranges, the negative bias I-V characteristic (purple) is plotted on the axis of the positive bias range I-V characteristic (blue). The positive bias axis is rescaled by a factor of  $1/1.3$  to account for the different lever arms of the two bias ranges (see text).

meV above the emitter Fermi level under flat band conditions, reducing the required bias voltage for resonant transport and thus the resulting distance to the collector Fermi sea.

Figure 8.1 shows the I-V characteristic at 1.7 K for positive and negative bias voltages. The apparent small remanent zero field splitting of approximately 1.5 mV of the peak at -2 mV is again the result of magnetic impurities in the vicinity of the quantum dot state [Goul 06].

At zero magnetic field, three resonances are observed for both negative (A, B and C) and positive (A', B' and C') bias voltages. Only feature A is however suggestive of an FES. That this enhancement only presents at negative bias voltage is due to the asymmetry of the active region and the resulting distinct interaction of the quantum dot state with the adjacent Fermi seas. As is clear from fig. 8.1, less bias voltage is required for feature A than for feature A'. Using equations (7.1) and (7.2) we determine lever arms of  $\alpha_- = 0.57$  and  $\alpha_+ = 0.43$  for negative and positive bias voltages, respectively. Figure 8.1b shows the negative I-V characteristic mirrored on the positive bias voltage axis, which was rescaled by  $\alpha_+/\alpha_- = 1/1.33$  to account for the asymmetry of the active region. As this rescaling perfectly aligns (A, A'), (B, B') and (C, C'), we conclude that each pair of features is reflective of tunneling through the same quantum dot level, where the only difference is the direction of the tunneling process. While features A, B and C enter the dot through the thicker of the two barriers, A', B' and C' describe the inverse path through the thinner barrier. By comparing the positive (blue) data to the rescaled negative (purple) data, we can estimate what fraction of the current stems from the stronger many body correlation effects at the top contact. A similar picture presents itself as in fig. 6.1, where a schematic of the enhancement is shown for degenerate spin levels at zero magnetic field and  $T = 0$  K.

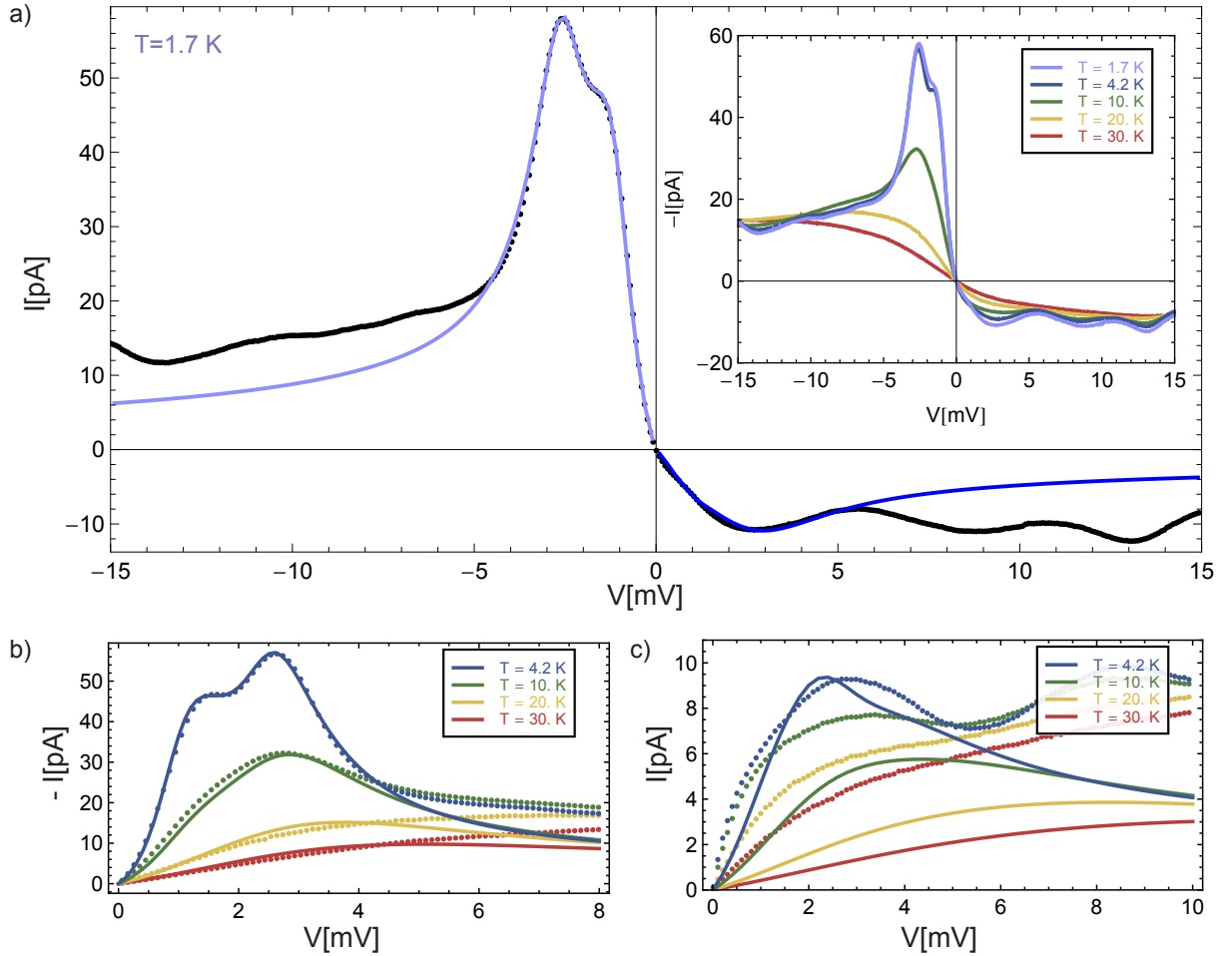


**Figure 8.2:** a) I-V characteristic at zero magnetic field and  $T=1.7$  K (black dots) and a fit using the same parameters for positive and negative bias voltages except a smaller FES exponent b) Fits to I-V characteristics at temperatures from 4.2 K to 30 K at negative bias voltages c) The same fits as in b), but again with smaller FES exponents.

While feature A exhibits a small remanent zero field splitting, no clear splitting of the resonance A' is observed. The enhancement to the tunneling rate when the state is aligned with the Fermi edge of the electrons in the top contact introduces a strong asymmetry in the peak shape and even the small splitting is clearly observed in feature A. Feature A' on the other hand shows no clear signs of such a spin-split resonant state, due to the lack of a strong FES enhancement from the bottom contact.

To further test the assumption that feature A is comprised of two FES enhanced resonance-peaks, we study the temperature dependence of features A and A'. Figure 8.2a shows the I-V characteristic at  $T=1.7$  K and zero magnetic field (black dots) and further measurements at elevated temperatures up to 30 K in its inset. While conventional FES theory only describes the enhancement of the tunneling rate, the resonant states studied

here are already so close to the Fermi energy at zero bias voltage, that the Fermi statistics will play a non-negligible role in the transport. A full description of the tunneling current is given by

$$I \propto \int T(E)D_E(E)D_C(E + eV)(f_E(E) - f_C(E + eV))dE \quad (8.1)$$

where  $D_E(E)$  and  $D_C(E + eV)$  are the density of states in emitter and collector,  $T(E)$  is transmittance of the double barrier and  $f_E(E)$  and  $f_C(E + eV)$  are the Fermi distributions in the emitter and the collector, respectively.

For a narrow line width of the resonant state on the quantum dot, we assume that transmission only occurs at the one energy in the emitter which is aligned with the resonant state. This energy is dependent on the applied bias voltage, as the quantum dot energy  $E_{dot} = E_0 - \alpha \cdot eV$  is lowered by the bias voltage drop across the barrier between the emitter and the quantum dot state. Assuming a constant density of states for the 2D emitter and collector states, equation (8.1) reduces to

$$I \propto T(E_{dot})(f_E(E_{dot}) - f_C(E_{dot} + eV)) \quad (8.2)$$

The nature of the transmission rate and its enhancement by the FES is captured within the conventional FES theory, which we use to model the I-V characteristics in chapter 6. The fit (light blue curve) to the experimental data in fig. 8.2a is thus accomplished by multiplying equation 6.1 with  $(f_E(E_{dot}) - f_C(E_{dot} + eV))$ . Using a two channel model, it yields a level position for the spin-up and spin-down states of 1.2 and 2.5 meV above the emitter Fermi energy, respectively. We find Fermi-edge exponents of  $\gamma_{-}^{\uparrow}=0.72$  and  $\gamma_{-}^{\downarrow}=0.71$  at this temperature. For positive bias voltages, using the same set of parameters and equation (7.2), we find Fermi-edge exponents of  $\gamma_{+}^{\uparrow}=0.51$  and  $\gamma_{+}^{\downarrow}=0.50$ . Due to the small asymmetry in this device, which can be expressed by the aforementioned ratio 1/1.33 of the lever arms, we observe an enhancement effect on both sides at low temperatures. In the previous chapter, where this ratio is approximately 1/2.1, no FES-like behavior is observed for positive bias voltages while a strong enhancement is present on all resonance-peaks occurring at negative bias voltages (see fig. 7.2a).

As is clear from the inset of fig. 8.2a, the only small difference between the I-V characteristics at 1.7 K and 4.2 K is the minor increase in amplitude of the resonance-peak occurring at  $\approx -1.5$  mV. In chapter 7, we find that the low temperature data is suggestive of a characteristic temperature in these systems, probably due to the intrinsic width of the BMP-like state. We thus exclude the measurement at 1.7 K from the temperature analysis in fig. 8.2b+c, as we allocate this temperature to the range where the system is still dominated by this intrinsic width. Figure. 8.2b shows good agreement of a two channel FES model (solid lines) to the experimental data (dots) for temperatures from 4.2 to 30 K at negative bias voltages.

For this elevated temperature range, we however find best results for a slightly different spin-up Fermi-edge exponent of  $\gamma_{\uparrow}=0.77$  and for small changes to the level positions.

These changes probably have two origins. First, here we fit the I-V characteristics within a two channel model. The spin-split pair of FES enhanced resonance-peaks is however likely comprised of a more complex spectrum as discussed in the previous chapter of this thesis. Here we however do not directly observe this fine structure, probably due to the lowest available temperature in the used  $^4\text{He}$  cryostat of 1.7 K and the very small zero field splitting. As the various transport channels do not share the same Fermi-edge exponent, they show a slightly different temperature dependence than a single broadened spin channel. Second, we most likely oversimplify the physics of the resonant tunneling by multiplying the conventional FES theory with a transfer function based on simple Fermi statistics, as the resonant level is of finite width. Furthermore this conventional theory omits the presence of the second Fermi sea, which can modify the FES enhancement [Aban 05]. As discussed above, the quantum dot will never be aligned with the Fermi-edge of the collector if it is located above  $E_F$  at zero bias. While the dot level is lowered by  $e(\alpha_-V)$ , the collector Fermi-edge will at the same time be lowered by  $eV > e(\alpha_-V)$ . For a finite width of the resonant state and small bias voltages, the presence of the second Fermi sea however probably effect the transport physics.

The giant Zeeman effect of the quantum dot state allows us to reduce the energy of the lower spin-state by several meV by means of an external magnetic field. As the fits suggest that this spin-state is located only  $\approx 1$  meV above the Fermi energy at zero bias voltage, we can use the external magnetic field to move this spin state with respect to the emitter Fermi sea without the need to alter the bias voltage.

Figure 8.3a shows I-V characteristics for external magnetic fields perpendicular to the layer stack from 0 to 6 T at 1.7 K. At 2 T and above the peak near zero bias voltage is suppressed, since its zero bias position is lowered below the Fermi energy of the emitter electron states by the giant Zeeman splitting of the quantum dot states in the external magnetic field.

As previously discussed, the fit to the I-V characteristics at  $T=1.7$  K and  $B=0$  T in (fig. 8.2a) suggests that both spin levels are still located above the Fermi energy at zero bias voltage. To further test this assumption we investigate the current at a small bias voltage for both positive and negative biases. Increasing the splitting of the two spin states via the external magnetic field should at first bring the spin-up state closer to the emitter Fermi energy, increasing the tunneling current due to the strong FES enhancement of the tunneling rate near the Fermi-edge. As we further increase the magnetic field, the spin state is lowered below the Fermi energy and the enhancement of the tunneling rate is reduced. Figure 8.3b plots the current at a constant small negative (red dots) and positive (blue dots) bias voltage, indicated by the dashed lines in fig. 8.3a. A constant bias voltage does not change the overlap of the occupied emitter electron states with the unoccupied collector states. Using the external magnetic field to move the level through this narrow channel, the current is mainly influenced by the energy dependance of the tunneling probability. While a magnetic field of  $B=1$  T yields a bigger current than for  $B=0$  T, a further increase of the magnetic field results in a reduction of this current, as we

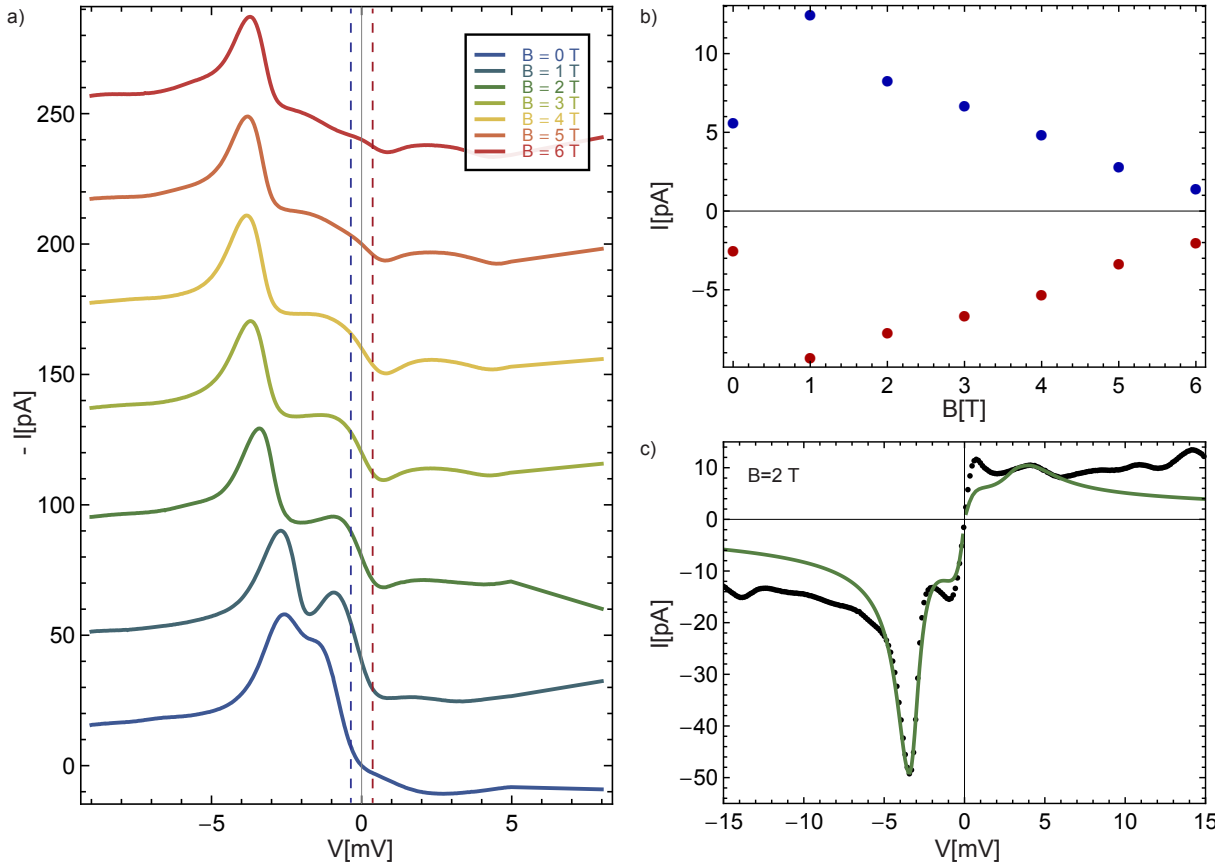


**Figure 8.3:** a) I-V characteristics for magnetic fields from 0 to 6 T. The curves are offset by 40 pA for clarity b) Dependence of the current at  $\pm 0.3$  mV on the external magnetic field c) Fit to the I-V characteristic at  $B = 2$  T

increase the energetic distance of the quantum dot state from the Fermi-edge, reducing the FES enhancement. Figure 8.3b thus gives further evidence that the spin-up state is still located slightly above the Fermi energy at  $V = 0$  V. Comparable amplitudes at 0 and 2 T however suggest that there is already finite overlap with the Fermi sea in the emitter at  $B = 0$  T due to the intrinsic broadening of the quantum dot state.

In summary, we have investigated the coupling of the same BMP-like state to two different Fermi reservoirs. A preliminary model shows that the transport at 1.7 K can be properly described by assuming different Fermi-edge exponents for the coupling to the two Fermionic baths. The small zero field splitting in this device is observed for negative bias voltages, due to the strong FES enhancement of the tunneling rate while coupling to the upper reservoir. Without this enhancement at positive bias voltages, this splitting is however not resolved.

# Chapter 9

## Conclusion and outlook

In this thesis we study the I-V characteristics of all II-VI semiconductor RTDs. We present a new empirical model that has led to a comprehensive understanding of the transport physics of these devices, and underlines the importance of often neglected device properties such as contact resistances and device imperfections.

Theoretical descriptions of such devices rely in many cases on idealized pictures based on the intended sample layout, assuming perfect layer interfaces, digital doping profiles and no intermixing of the various heterostructure materials. Additionally, effects from contacts and other secondary parts of the device are considered small and are thus omitted. Here we show that most of these assumptions break down for the II-VI quantum well RTDs, and that considering these effects is important for a proper description of these devices.

In particular, we find that interface states play an important role in the transport characteristics of quantum well RTDs. Our detailed model suggests spin-filter capabilities without the need for an external magnetic field despite the paramagnetic nature of the quantum well material. We further investigate these interface states by removing the substrate from such devices, altering the layer properties and eventually the interface states. A comparison of the fits to the I-V characteristics before and after removal of the substrate yield results which are consistent with a general increase of layer quality.

To further investigate the role of reduced dimensionality in the resonant tunneling process one could combine the quantum dot with the quantum well design. For example growing CdSe quantum dots between the DMS quantum well and one of the tunnel barriers should result in an even stronger lateral potential roughness. One could thus study the dependence of the I-V characteristics on the CdSe coverage at the interface. By doing so only on one side, we could compare the tunneling from the emitter through the (Zn,Be)Se-CdSe-(Zn,Mn)Se interface to tunneling through the opposite side by changing the sign of the applied bias voltage

Equipped with a comprehensive understanding of the transport physics of a single DMS RTD, a natural extension is to combine two such devices in an injector-detector scheme. Having a highly non-linear I-V characteristic, the interplay of the RTD with any

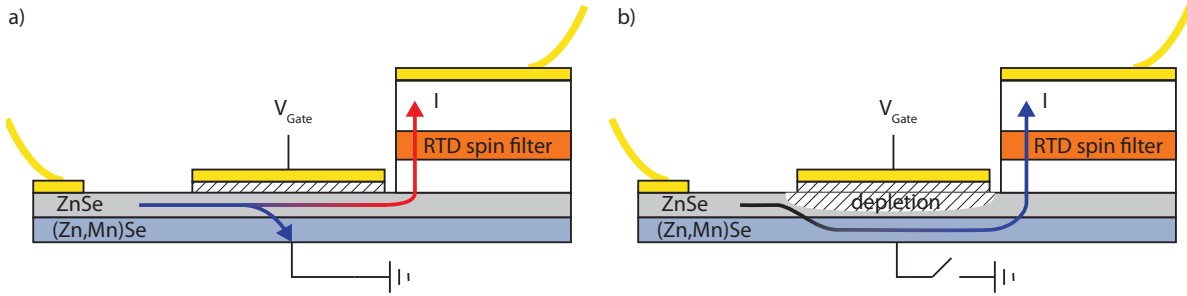


**Figure 9.1:** Device proposal for a compound spintronics device utilizing the lateral Gurzhi device as a spin aligner for the injection into a RTD. a) Due to the polarized layer, only one spin type has a low resistance to ground and is thus extracted from the upper layer, polarizing the latter. As the injected current is now spin polarized, it can be detected by the magnetic RTD. b) Via the gate the upper layer is depleted, forcing all current to flow through the polarized layer. The polarized current is reinjected into the upper layer and into the analyzer RTD.

additional resistances of comparable size is prone to cause bistabilities in its circuitry. This limits their integrability into more complex compound devices. Nevertheless, we demonstrate such a device comprised of two RTDs in series and find that an optimized contact resistance between the two is of utmost importance for the realization of the latter.

My colleague Philip Hartman is currently developing a spin aligner based on the proposal made by Gurzhi [Gurz 09]. Combining the lateral transport in the Gurzhi device with the vertical transport through a DMS RTD might be a promising prospect for an improved spin-valve layout. This compound device is shown in fig. 9.1. We apply a bias voltage between the contact on the left and the top of the RTD. For a finite magnetic field the (Zn,Mn)Se is polarized and as soon as the backside of the sample is shorted to ground, the majority spin species in the upper layer will see a low resistance to ground, leaving the sample through the backside contact (9.1a). The minority spin species will however mainly remain in the upper layer and is thus injected into the RTD. In a second operation mode (9.1b) the gate is used to force the electrons through the DMS layer, resulting in a polarized current. However if the lateral extent of the RTD is a lot larger than the spin flip length in this material, most of the spin-polarization would be lost due to the current spreading. Thus a proper planing of the device geometry will be of essence. The Gurzhi part of the compound device is likely of lower resistance than a second DMS RTD, but can also be controlled via the gate voltage. It can however only produce one spin type at a given magnetic field. The RTD bias voltage can then be used to either transmit or block the injected electrons.

We have shown that modifications to the I-V characteristics stemming from an additional lateral confinement in the quantum well RTD are useful for spintronic applications.



---

To enhance these effects we replace the quantum well layer with self-assembled quantum dots.

First experiments on resonant tunneling through a non-magnetic self-assembled CdSe quantum dot yield a strong enhancement of the tunneling rate due to the interplay of the localized quantum dot state with the emitter Fermi sea. Furthermore, Gould et al. previously demonstrated that these CdSe dots lead, if imbedded in magnetic tunnel barriers, to a second many particle effect, namely the formation of BMPs. Lifting the degeneracy of the spin states, resonant tunneling through such BMPs allows for a spin dependent transport without the need for an external magnetic field. Here we demonstrate a magnetic SAD RTD where both many particle effects are observed simultaneously. As one of these many particle effects stems from interaction with a Fermionic bath while the other is due to the coupling to a cloud of magnetic moments, such a system could prove a suitable testbed for Fermi-Bose Kondo physics. These system are currently of considerable interest as they can be tuned to a quantum critical point.

An important tool to further study such low dimensional systems are lateral gates. Lateral gates can be used to shift the quantum states between the tunnel barriers, instead of tilting the potential landscape. As we have shown for quantum well RTDs the applied bias voltage can strongly influence the transport characteristics by altering the barrier heights, the symmetry of the double barrier structure as well as the emitter states. This technology is currently under development by my colleague Gabriel Dengel showing first promising results on artificial atoms created by lateral down-sizing of magnetic quantum well RTDs. Comparing such devices to the RTDs based on self assembled quantum dots will also shed light on the influence of the geometry, composition and confinement of the 0D quantum state.

Spin-polarized scanning tunneling microscopy on the cleaving edge of a self-assembled dot RTD with DMS tunnel barriers could furthermore be used to investigate the BMP states that manifest themselves in these systems. While it is not feasible to examine the exact same dot characterized in transport, a general picture of the shape of the dots as well as the distribution of the Mn atoms in their vicinity could be established. To study the wave function of a specific dot by means of transport, one could use angle resolved magnetotunneling spectroscopy. This technique was developed to image the quantum dot wave function on non-magnetic III-VI SAD RTDs [Vdov 00].

By means of the lateral gates and the angle resolved magnetotunneling experiments, one has two more ways to probe the rich physics of these magnetic nanostructures. These are in my opinion imperative to a comprehensive understanding of present and future experiments on these complex transport systems.



# Appendix A

## Numerical solution of a double RTD circuit

### A.1 A homotopy Newton method

While the Kirchhoff equations for the equivalent circuit of fig. 3.4a can be solved numerically with a standard Newton method for a single DMS RTD, this method fails for two of these RTDs in series. For the spin-valve compound device presented in chapter 5, one RTD acts as a non-linear series resistance to the other RTD. In combination with the alternative current path to ground through the middle contact resistance, a load line analysis as shown in fig. 5.7 has to be conducted. Depending on the size of the middle contact resistance, the load line reflects the I-V characteristics of the second diode. The second RTD is an additional non-linear element in the circuit and the equivalent circuit shown in fig. 5.2b is more prone to instabilities than the one for a single RTD.

Figure A.1 depicts the load line analysis for the separate spin-up and down channels at  $V_T=144$  mV and  $V_B=140$  mV. Figures A.1a+b show the solutions to the Kirchhoff equations of fig. 5.2 given by the standard Newton method, while fig. A.1c+d show the results yielded by a homotopy method. For these bias voltages a problem arises only for the spin-up channel. The standard Newton method fails to compute the correct solution because the load line and the  $I_T - V_T^\uparrow$  characteristics run almost parallel between 120 and 140 mV. The path of the Newton method is depicted as the dashed lines, connecting the iteration points (black dots) of the algorithm. The correct (graphical) solution is marked by the dashed circle at  $V_{sol}=159.2$  mV, which differs more than 25 mV from the solution  $V_{NM}$  computed with the Newton method.

The Newton method often fails in these situations, unless a good initial guess is chosen as the starting point for the iteration. Especially for two non-linear elements in the circuit, as in the case of the spin-valve, it can prove difficult to find a proper starting point for the complete range of both bias voltages.

We introduce the homotopy parameter  $\lambda$  by substituting the middle contact resistance

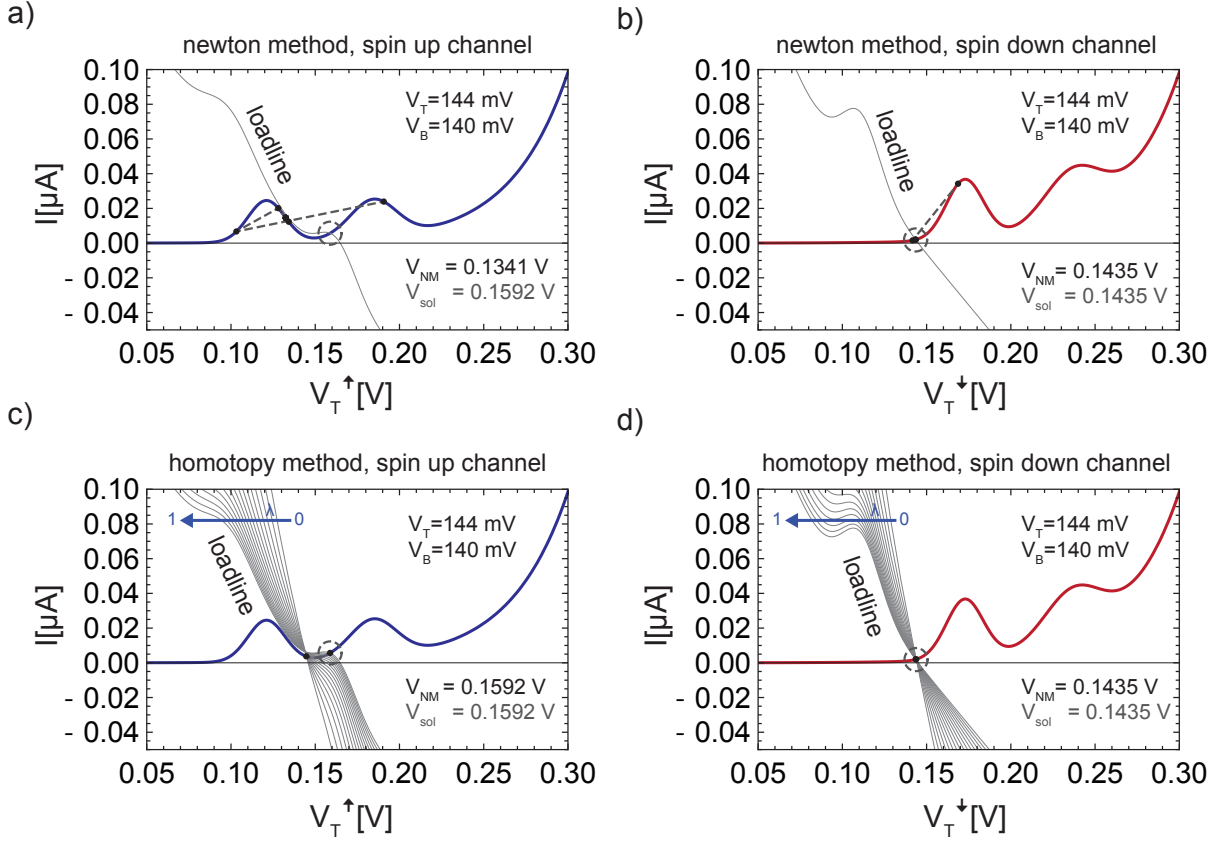


**Figure A.1:** a)+b) Solution to the Kirchhoff equations of the equivalent circuit of fig 5.2 as given by a standard Newton method for the spin up and down channel, respectively. c)+d) The same set of equations solved within a homotopy method, yielding a result in agreement with the graphical solution.

$R_m$  with  $\lambda \cdot R_m$  in the equivalent circuit of fig. 5.2. As is shown in fig. A.1c and d, the starting point for the homotopy method is the solution to the Kirchhoff equations of the circuit for  $\lambda \rightarrow 0$ , which effectively shortens both diodes to ground as discussed in chapter 5 and shown in fig. 5.7. This results in a stable solution for the Newton method, as the problem reduces to a normal load line analysis with a small series resistance. This stable solution is used for the starting point for the next iteration with  $\lambda_{i+1} = \lambda_i + d\lambda$ . As is apparent from the gray lines in fig. A.1c and d, steadily increasing  $\lambda$  will slowly converge the solution to the case of fully coupled RTDs. For each iteration the previous solution is used as a starting point. As a result, there is no need to guess a proper starting point, no matter what bias voltages  $V_T$  and  $V_B$  are applied to the spin-valve.

## A.2 Computing the path along a spin-resonance

The homotopy method described in the previous section enables the model presented in chapter 5 to calculate the currents  $I_1$  and  $I_2$  as a function of the voltages  $V_B$  and  $V_T$  across

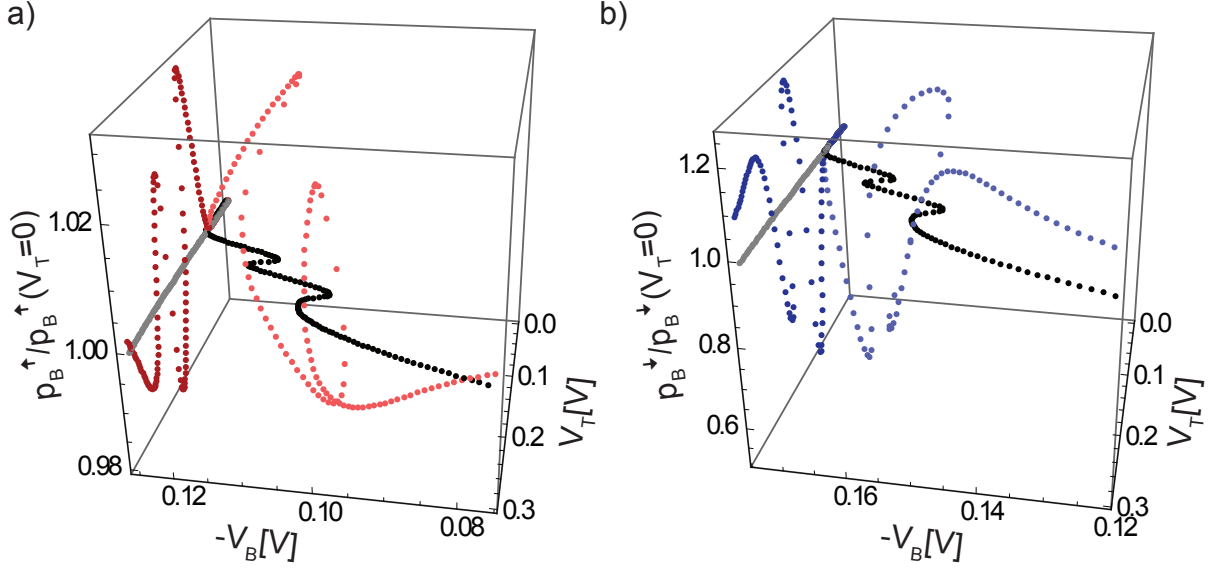


**Figure A.2:** Polarization of the current exiting the bottom RTD as a function of the voltage across each RTD. a) The dark red dotted line is the projection on the  $V_T$  axis as it is shown in fig. 5.10b. The light red dots also show the  $V_B$  dependence while following the spin-up resonance as indicated by the dashed line of fig. 5.10a. The black dots the same analysis when setting  $R_{flip}$  to  $10 \Omega$ . The resistivity effects are still visible, while the spin-valve effects (change of polarization) is destroyed by allowing spin flips in between the two diodes. b) The same path analysis as in a), but for following the spin-down resonance in fig. 5.10a.

each diode.

Due to the highly non-linear character of the device, the analysis of a parameter like the polarization as a function of one voltage while keeping the other constant does however not reflect the spin-valve functionality as is clear from fig 5.3b+c. The best way to distinguish the spin-valve properties from the resistive effects is to select points in the  $V_B$ - $V_T$  plane such that the bias voltage across a certain circuit element is kept constant. These points form a path along which the spin-valve property tributary to this circuit element can be extracted.

This method is used for example in fig. 5.10a, where the dashed lines represent two such paths. These paths, following the up and down spin resonances of the bottom diode, are used to extract the polarization of the bottom diode as a function of  $V_T$  (shown in fig. 5.10b+c). At first the peak positions for the  $I_2 - V_B$  characteristics at a small  $V_T$  are determined. As discussed in chapter 5, this setting resembles a simple spin-filter characteristics with an additional series resistance, similar to the device shown in chapter 3. These peak positions are the starting points for computing the aforementioned dashed lines. As we are interested in the polarization values at the spin-up and down resonances of the bottom diode, the relevant voltages in the equivalent circuit of fig. 5.2b are the voltage drops  $V_B^\uparrow$  and  $V_B^\downarrow$  across the active regions of the spin-up and down channels

respectively. For instance, to compute the path for a constant voltage drop  $V_B^\uparrow$  across the spin-up channel of the bottom diode, we at first increase  $V_T$  by  $dV_T$ .  $V_B$  now has to be changed as well, as  $V_T + dV$  results in a different  $V_B^\uparrow$  than for the  $V_T$  setting.  $V_B$  is thus changed iteratively until  $V_B^\uparrow$  has the same value as for the setting  $(V_T, V_B)$ .

The light red (light blue) dots of fig. A.2a (b) show this procedure for extracting the spin-valve efficiency from fig. 5.10 following the paths along the spin-up (down) resonance of the bottom diode. Figures A.2a+b show the resulting complex path assuming spin conservation between the two diodes. The black and gray curves show the path for  $R_{flip}=10 \Omega$  and its projection to the  $p/p(0) - V_T$  plane, respectively. The red and blue projections shown on the  $p/p(0) - V_T$  planes of fig. A.2a+b are the equivalents of fig. 5.10b+c for the spin-up efficiency (dark red dots) and the spin-down efficiency (dark blue dots) respectively.

# Appendix B

## Scientific publishing with Mathematica

Mathematica is a powerful and versatile tool for the plotting and postprocessing of data as well as for the modeling thereof.

While programming your graphical output is often less convenient than a graphical user interface like Origin, it gives you full control of what your graphic will look like in the end. Mathematica allows you to write customized functions for pretty much everything, from color coding your data to a customized mesh in a 3D plot.

While all this control is great, as a scientist, at the end of the day you need something which can easily be implemented in your talks, papers and/or posters. The best possible way to achieve all that is in my opinion the pdf format. You can easily add it almost everywhere as pdf is a wide spread container format, and even if that doesn't work, you still can use the "snapshot" tool in Acrobat Reader to create a high resolution JPG image of your graphic and copy and paste it pretty much everywhere.

But actually getting from your data to a high quality pdf with Mathematica can cause quite some frustration. The export of pdf graphics from Mathematica has some peculiarities I'd like to address, as I have been asked these questions several times by various colleagues.

As long as you export a simple curve like an I-V characteristic to a pdf file and include this graphic in TeX as is, you won't experience any problems. However, often the picture needs to be part of a bigger layout as a sub-figure, or processing of the exported pdf within a vector program like Adobe Illustrator is necessary. Opening a pdf exported with Mathematica in Adobe Illustrator will reveal how bad the pdf export actually is. Every single vector entity will be grouped and covered by a clipping mask, which unnecessarily increases the file size and also makes working with the layers a nightmare.

In general, I advise to "place" Mathematica pdf files in Illustrator, not copy and paste them (which also works). Note that the resulting Illustrator file will *not* contain the placed graphics, but only link to the object. Let us assume we want to create a graphic containing four sub-figures a-c. Each of those figures is a plot created within Mathematica.

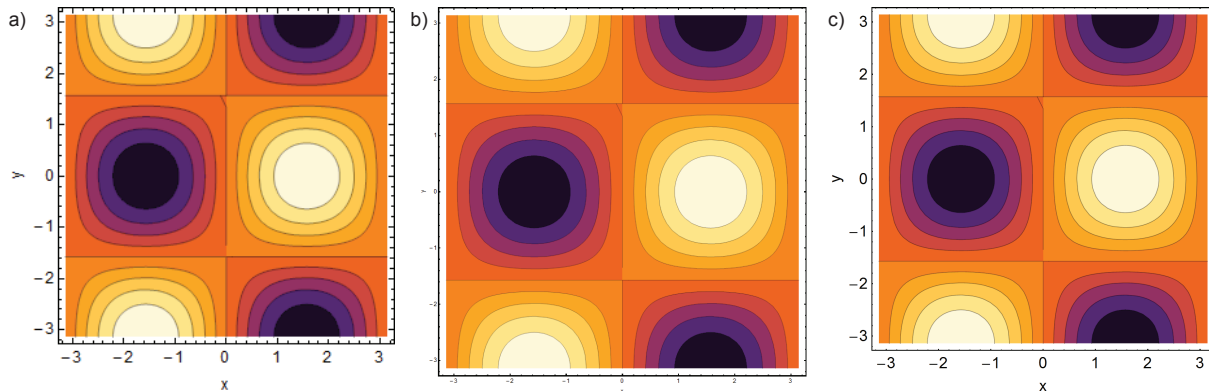


**Figure B.1:** Export of the same image, employing different export options in Mathematica 8. a) Exporting as PNG in its original size, with screen resolution. b) Increasing the image size for better quality will result in unreadable axis labels c) Export as in a) but increasing the "ImageResolution" instead of "ImageSize"

Now we place, scale, arrange and label all of them within Illustrator. The beauty about placing the graphic is that once we make changes to the graphic within Mathematica and export it again to the same filename and location, Illustrator will notice the change and ask you, whether you want to update your link. Press "yes" and you will see the new version of the graphic, perfectly scaled and arranged within your document.

The aforementioned clipping masks and white background rectangles Mathematica likes to add to your otherwise perfect images can however result in glitches during the export of your final composed image from Illustrator to the pdf format. Parts of the graphics often vanish due to overlapping clipping masks and/or white background rectangles. In order to remove those from your exported Mathematica pdfs, open the pdf in Illustrator and simply use "Select → Object → Clipping Masks" and press delete on your keyboard. Then control your graphic by pressing "Ctrl+Y" to show only the outlines of your graphic and detect any useless background shapes. Use the direct selection tool to delete those as well.

Be aware that if you use "PlotRange" within Mathematica, the overhead of data is not shown within your graphic, but an exported pdf still contains it. To reduce file size and also trouble with your exported pdf, be advised to chop your data according to your desired PlotRange, instead of just hiding it. Mathematica will do so by, of course adding another clipping mask. If we delete all of those, you will end up with revealing your hidden data in your graphic. So either get rid of it before exporting, or simply locate the clipping mask hiding this data in the layers of your pdf and lock it before selecting and deleting the rest of them.

Please also note that there is a problem of exporting and reimporting Mathematica fonts. Illustrator will often display crossed out rectangles instead of minus signs, or brackets. The best way to minimize the extra effort is probably to create plot labels within Illustrator. So all you have to repair after loading the pdf within Illustrator usually



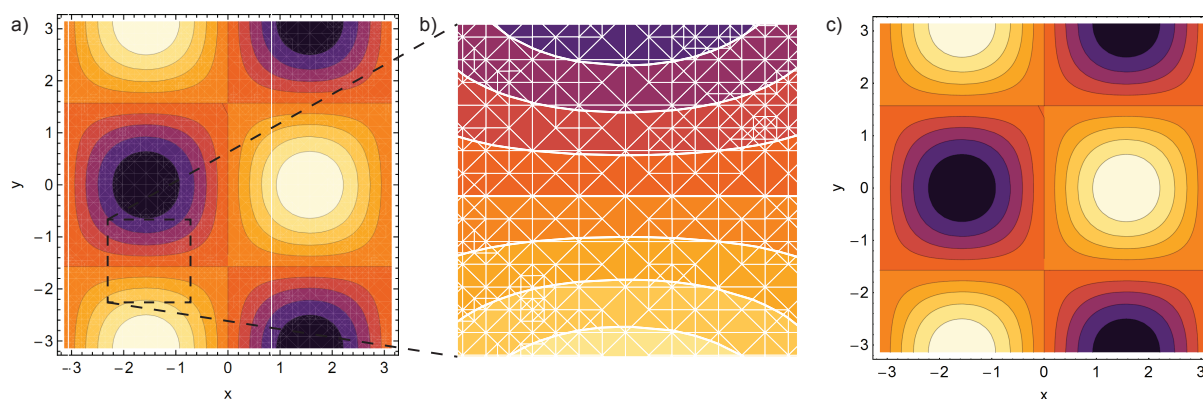


**Figure B.2:** a) Exporting the graphic as fully vectorized produces white lines around each voxel. b) 400% magnification of the image shown in a). c) Rasterized image with an resolution of 300 dpi.

are some minus signs on your axes.

I will also outline my way of exporting high quality ListDensityPlots at an arbitrary example. Figure B.1 shows three ListDensityPlots exported to png files from Mathematica. For fig. B.1a the standard export options were used, resulting in an image with low resolution. While it has reasonable quality at this size in a printout, you will not be able to use it for anything larger. If we just export the same picture while increasing the ImageSize in Mathematica, you will end up having tiny axes labels after rescaling it in your TeX file as shown in fig. B.1b. What you could do is to use the export option "ImageResolution->300" to achieve a higher image quality, while maintaining the appearance of the figure (fig. B.1c).

If we export the same image in the pdf format, we are confronted with a different kind of problem. As is shown in fig. B.2a, Each data point is represented by a vector shape. These shapes are however not perfectly aligned in the pdf output of Mathematica, which results in very thin, but ugly white lines in your plot. This is more clearly shown by a magnification of this plot in fig. B.2b. Figure B.2 again shows a 300dpi png version of this graph, where we do not have this problem. Note however that the tick marks are barely big enough to see.

The proper (but more time consuming) way to do these graphics is the following. First, export a ContourPlot of your data while only showing the contour lines and not the color encoding of your data. Export to the pdf format to gain a vector graphic of this wire frame (fig. B.3a). Second, export the color coded data as a high resolution png file (fig. B.3b). Ultimately, combine steps one and two in Illustrator. Note that fig. B.3a will have a white background layer which needs to be removed before it is transparent. The big advantage of this procedure is that you will be able to change the appearance of the mesh using Illustrator as is shown in fig. B.3a. This method was for example used in fig. 5.3 of this thesis.

For completeness, the source code for fig. B.3a+b is given in B.1.

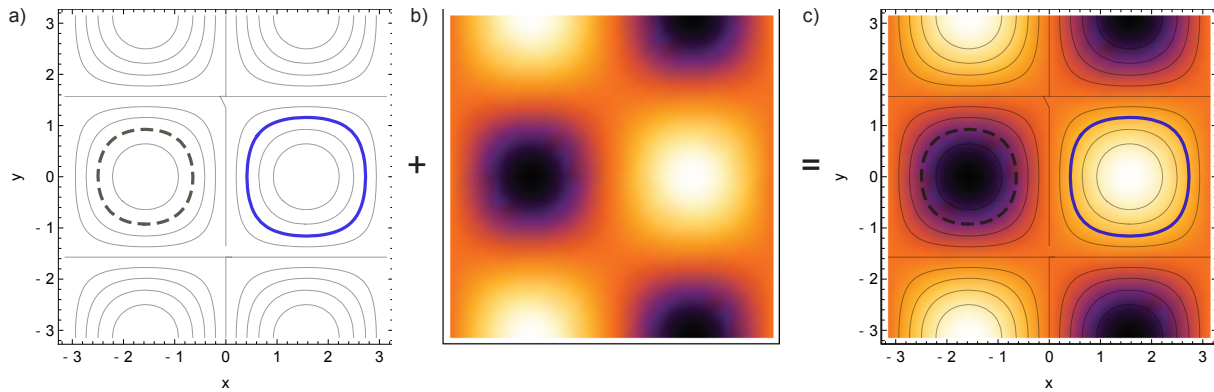


**Figure B.3:** Comprising the picture from a rasterized background and a vector wire frame showing axes labels and the contour lines.

---

```

1 graphFrame = ContourPlot[
2   Cos[y]*Sin[x ], {x, -\[Pi], \[Pi]}, {y, -\[Pi], \[Pi]},
3   FrameLabel -> {"x", "y"}, ImagePadding -> {{40, 0}, {40, 0}},
4   ContourShading -> None
5 ]
graphBG = DensityPlot[
7   Cos[y]*Sin[x ], {x, -\[Pi], \[Pi]}, {y, -\[Pi], \[Pi]},
8   FrameLabel -> None, FrameTicks -> None,
9   ImagePadding -> {{40, 0}, {40, 0}}, ColorFunction -> "SunsetColors"
10 ]
11 Export["graph_Frame.pdf", graphFrame]
13 Export["graph_bg.png", graphBG, ImageResolution -> 300]

```

---

**Listing B.1:** Creating two separate graphics to recombine them in Adobe Illustrator has various advantages over a pure rasterized output.

# Bibliography

- [Aban 04] D. A. Abanin and L. S. Levitov. *Phys. Rev. Lett.*, Vol. 93, No. 12, p. 126802, 2004.
- [Aban 05] D. A. Abanin and L. S. Levitov. *Phys. Rev. Lett.*, Vol. 94, No. 18, p. 186803, 2005.
- [Alle 94] S. S. Allen and S. L. Richardson. *Phys. Rev. B*, Vol. 50, No. 16, pp. 11693–, 1994.
- [Alle 96] S. S. Allen and S. L. Richardson. *J. Appl. Phys.*, Vol. 79, No. 2, pp. 886–894, 1996.
- [Appe 07] I. Appelbaum, B. Huang, and D. J. Monsma. *Nature*, Vol. 447, No. 7142, pp. 295–298, 2007.
- [Asta 02] G. V. Astakhov, D. R. Yakovlev, V. P. Kochereshko, W. Ossau, W. Faschinger, J. Puls, F. Henneberger, S. A. Crooker, Q. McCulloch, D. Wolverson, N. A. Gippius, and A. Waag. *Phys. Rev. B*, Vol. 65, No. 16, pp. 165335–, 2002.
- [Aust 99] D. G. Austing, S. Tarucha, P. C. Main, M. Henini, S. T. Stoddart, and L. Eaves. *Applied Physics Letters*, Vol. 75, No. 5, pp. 671–673, 1999.
- [Bele 05] N. N. Beletskii, G. P. Berman, and S. A. Borysenko. *Phys. Rev. B*, Vol. 71, No. 12, pp. 125325–, 2005.
- [Bene 98] K. Benedict, A. Thornton, T. Ihn, P. Main, L. Eaves, and M. Henini. *Physica B: Condensed Matter*, Vol. 256-258, pp. 519–522, 1998.
- [Biek 10] S. Bieker. Magneto-optische und Transport-Untersuchungen an Spinfilterelementen auf Basis semimagnetischer II-VI-Halbleiter, Diplomarbeit, Universität Würzburg, EP3, 2010.
- [Borz 04] T. Borzenko, C. Gould, G. Schmidt, and L. W. Molenkamp. *Microelectronic Engineering*, Vol. 75, No. 2, pp. 210–215, 2004.
- [Brad 05] C. Bradford, A. Curran, A. Balocchi, B. Cavenett, K. Prior, and R. Warburton. *Journal of Crystal Growth*, Vol. 278, No. 1-4, pp. 325–328, 2005.
- [Brau 03] B. Braunecker. *Phys. Rev. B*, Vol. 68, No. 15, pp. 153104–, 2003.

- [Buot 00] F. A. Buot, P. Zhao, H. L. Cui, D. L. Woolard, K. L. Jensen, and C. M. Krowne. *Phys. Rev. B*, Vol. 61, No. 8, pp. 5644–, 2000.
- [Butt 88] M. Buttiker. *Ibm Journal of Research and Development*, Vol. 32, No. 1, pp. 63–75, 1988.
- [Cate 92] A. Catellani and P. Ballone. *Phys. Rev. B*, Vol. 45, No. 24, pp. 14197–, 1992.
- [Chan 74] L. L. Chang, L. Esaki, and R. Tsu. *Applied Physics Letters*, Vol. 24, No. 12, pp. 593–595, 1974.
- [Chau 00] C. Chauvet, E. Tournie, and J.-P. Faurie. *Phys. Rev. B*, Vol. 61, No. 8, p. 5332, 2000.
- [Choi 92] Y. W. Choi and C. R. Wie. *J. Appl. Phys.*, Vol. 71, No. 4, pp. 1853–1859, 1992.
- [Croo 05] S. A. Crooker, M. Furis, X. Lou, C. Adelman, D. L. Smith, C. J. Palmstrom, and P. A. Crowell. *Science*, Vol. 309, No. 5744, pp. 2191–2195, 2005.
- [Dai 94] N. Dai, L. R. Ram-Mohan, H. Luo, G. L. Yang, F. C. Zhang, M. Dobrowolska, and J. K. Furdyna. *Phys. Rev. B*, Vol. 50, No. 24, pp. 18153–, 1994.
- [Diet 82] T. Dietl and J. Spalek. *Phys. Rev. Lett.*, Vol. 48, No. 5, pp. 355–, 1982.
- [Diet 83] T. Dietl and J. Spalek. *Phys. Rev. B*, Vol. 28, No. 3, pp. 1548–, 1983.
- [Diet 86] T. Dietl, J. Spalek, and L. Sacutewierkowski. *Phys. Rev. B*, Vol. 33, No. 10, pp. 7303–, 1986.
- [Egue 98] J. C. Egues. *Phys. Rev. Lett.*, Vol. 80, No. 20, pp. 4578–, 1998.
- [Ertl 07] C. Ertler and J. Fabian. *Phys. Rev. B*, Vol. 75, No. 19, pp. 195323–, 2007.
- [Fert 68] A. Fert and I. A. Campbell. *Phys. Rev. Lett.*, Vol. 21, No. 16, pp. 1190–, 1968.
- [Fied 99] R. Fiederling, M. Keim, G. Reuscher, W. Ossau, G. Schmidt, A. Waag, and L. W. Molenkamp. *Nature*, Vol. 402, No. 6763, pp. 787–790, 1999.
- [Fock 28] V. Fock. *Zeitschrift für Physik A Hadrons and Nuclei*, Vol. 47, No. 5, pp. 446–448, 1928.
- [Fost 89] T. J. Foster, M. L. Leadbeater, L. Eaves, M. Henini, O. H. Hughes, C. A. Payling, F. W. Sheard, P. E. Simmonds, G. A. Toombs, G. Hill, and M. A. Pate. *Phys. Rev. B*, Vol. 39, No. 9, pp. 6205–, 1989.
- [Frah 06] H. Frahm, C. von Zobeltitz, N. Maire, and R. J. Haug. *Phys. Rev. B*, Vol. 74, No. 3, p. 035329, 2006.

- [Frey 10] A. Frey, M. Rüth, R. Dengel, C. Schumacher, C. Gould, G. Schmidt, K. Brunner, and L. Molenkamp. *Journal of Crystal Growth*, Vol. 312, No. 7, pp. 1036–1039, 2010.
- [Gaj 79] J. A. Gaj, R. Planel, and G. Fishman. *Solid State Comm.*, Vol. 29, No. 5, pp. 435–438, 1979.
- [Gamm 96] D. Gammon, E. S. Snow, B. V. Shanabrook, D. S. Katzer, and D. Park. *Phys. Rev. Lett.*, Vol. 76, No. 16, pp. 3005–, 1996.
- [Geim 94] A. K. Geim, P. C. Main, N. Lascalea, L. Eaves, T. J. Foster, P. H. Beton, J. W. Sakai, F. W. Sheard, M. Henini, G. Hill, and M. A. Pate. *Phys. Rev. Lett.*, Vol. 72, No. 13, pp. 2061–2064, 1994.
- [Gold 87a] V. J. Goldman, D. C. Tsui, and J. E. Cunningham. *Phys. Rev. B*, Vol. 36, No. 14, pp. 7635–, 1987.
- [Gold 87b] V. J. Goldman, D. C. Tsui, and J. E. Cunningham. *Phys. Rev. Lett.*, Vol. 58, No. 12, pp. 1256–, 1987.
- [Goul 06] C. Gould, A. Slobodskyy, D. Supp, T. Slobodskyy, P. Grabs, P. Hawrylak, F. Qu, G. Schmidt, and L. W. Molenkamp. *Phys. Rev. Lett.*, Vol. 97, No. 1, p. 017202, 2006.
- [Gurz 09] R. N. Gurzhi, A. N. Kalinenko, A. I. Kopeliovich, and A. V. Yanovsky. *J. Appl. Phys.*, Vol. 105, No. 10, p. 103713, 2009.
- [Hapk 00] I. Hapke-Wurst, U. Zeitler, H. Frahm, A. G. M. Jansen, R. J. Haug, and K. Pierz. *Phys. Rev. B*, Vol. 62, No. 19, pp. 12621–12624, 2000.
- [Havu 05] P. Havu, N. Tuomisto, R. Vaananen, M. J. Puska, and R. M. Nieminen. *Phys. Rev. B*, Vol. 71, No. 23, p. 235301, 2005.
- [Herb 98] M. Herbich, A. Twardowski, D. Scalbert, and A. Petrou. *Phys. Rev. B*, Vol. 58, No. 11, pp. 7024–, 1998.
- [Hill 01] R. J. A. Hill, A. Patane, P. C. Main, L. Eaves, B. Gustafson, M. Henini, S. Tarucha, and D. G. Austing. *Appl. Phys. Lett.*, Vol. 79, No. 20, pp. 3275–3277, 2001.
- [Indl 04] K. Indlekofer and J. Malindretos. “Wingreen Simulation package (Version 2.1.1)”. 2004.
- [Isaa 88] E. D. Isaacs, D. Heiman, M. J. Graf, B. B. Goldberg, R. Kershaw, D. Ridgley, K. Dwight, A. Wold, J. Furdyna, and J. S. Brooks. *Phys. Rev. B*, Vol. 37, No. 12, pp. 7108–, 1988.
- [Itsk 96] I. E. Itskevich, T. Ihn, A. Thornton, M. Henini, T. J. Foster, P. Moriarty, A. Nogaret, P. H. Beton, L. Eaves, and P. C. Main. *Phys. Rev. B*, Vol. 54, No. 23, pp. 16401–, 1996.

- [Jans 07] R. Jansen and B. C. Min. *Phys. Rev. Lett.*, Vol. 99, No. 24, pp. 246604–, 2007.
- [Kim 00] M. Kim, C. S. Kim, S. Lee, J. K. Furdyna, and M. Dobrowolska. *Journal of Crystal Growth*, Vol. 214-215, pp. 325–329, 2000.
- [Kirc 05] S. Kirchner, L. J. Zhu, Q. M. Si, and D. Natelson. *Proceedings of the National Academy of Sciences of the United States of America*, Vol. 102, No. 52, pp. 18824–18829, 2005.
- [Kirc 08a] S. Kirchner and Q. Si. *Physica B: Condensed Matter*, Vol. 403, No. 5-9, pp. 1189–1193, 2008.
- [Kirc 08b] S. Kirchner and Q. Si. *Phys. Rev. Lett.*, Vol. 100, No. 2, pp. 026403–, 2008.
- [Kirc 09] S. Kirchner and Q. Si. *Phys. Rev. Lett.*, Vol. 103, No. 20, pp. 206401–, 2009.
- [Kouw 21] L. P. Kouwenhoven, A. T. Johnson, N. C. van der Vaart, A. van der Enden, C. J. P. M. Harmans, and C. T. Foxon. *Zeitschrift für Physik B Condensed Matter*, Vol. 85, No. 3, pp. 381–388, 1991-10-21.
- [Land 99] Landolt-Börnstein. *Intrinsic Properties of Group IV Elements and III-V, II-VI and I-VII Compounds, New Series, Group III, Vol. 22a*. Springer-Series, 1999.
- [Lead 89] M. L. Leadbeater, E. S. Alves, L. Eaves, M. Henini, O. H. Hughes, A. Celeste, J. C. Portal, G. Hill, and M. A. Pate. *Phys. Rev. B*, Vol. 39, No. 5, pp. 3438–, 1989.
- [Lee 07] S. Lee, M. Dobrowolska, and J. Furdyna. *Journal of Crystal Growth*, Vol. 301-302, pp. 781–784, 2007.
- [Lehm 05] F. Lehmann. *Prozessierung und elektrische Charakterisierung von ZnSe Heterostrukturen in verschiedenen Messgeometrien zum eindeutigen Nachweis der elektrischen Spininjektion*. PhD thesis, Fakultät für Physik und Astronomie, Universität Würzburg, 2005.
- [Li 06] M. K. Li, N. M. Kim, S. J. Lee, H. C. Jeon, and T. W. Kang. *Appl. Phys. Lett.*, Vol. 88, No. 16, pp. 162102–3, 2006.
- [Lou 07] X. Lou, C. Adelman, S. A. Crooker, E. S. Garlid, J. Zhang, K. S. M. Reddy, S. D. Flexner, C. J. Palmstrom, and P. A. Crowell. *Nat Phys*, Vol. 3, No. 3, pp. 197–202, 2007.
- [Lury 85] S. Luryi. *Appl. Phys. Lett.*, Vol. 47, No. 5, pp. 490–492, 1985.
- [Lury 89] S. Luryi. *Superlattice Microstr.*, Vol. 5, No. 3, pp. 375–382, 1989.
- [Maha 06] S. Mahapatra, K. Brunner, C. Schumacher, T. Kiessling, G. V. Astakhov, U. Bass, E. Margapoti, W. Ossau, J. Geurts, L. Worschech, A. Forchel, and L. W. Molenkamp. *physica status solidi (c)*, Vol. 3, No. 4, pp. 928–932, 2006.

- [Maha 07] S. Mahapatra. *Formation and properties of epitaxial CdSe/ZnSe quantum dots*. PhD thesis, Universität Würzburg, 2007.
- [Maha 67] G. D. Mahan. *Phys. Rev.*, Vol. 163, No. 3, pp. 612–, 1967.
- [Main 98] P. C. Main, A. S. G. Thornton, T. Ihn, L. Eaves, K. A. Benedict, and M. Henini. *Physica B*, Vol. 258, pp. 507–513, 1998.
- [Mair 07] N. Maire, F. Hohls, T. Ludtke, K. Pierz, and R. J. Haug. *Phys. Rev. B*, Vol. 75, No. 23, p. 233304, 2007.
- [Maka 10] O. Makarovskiy, A. G. Balanov, L. Eaves, A. Patané, R. P. Campion, C. T. Foxon, and R. J. Airey. *Phys. Rev. B*, Vol. 81, No. 3, pp. 035323–, 2010.
- [Matv 92] K. A. Matveev and A. I. Larkin. *Phys. Rev. B*, Vol. 46, No. 23, pp. 15337–15347, 1992.
- [McEu 91] P. L. McEuen, E. B. Foxman, U. Meirav, M. A. Kastner, Y. Meir, N. S. Wingreen, and S. J. Wind. *Phys. Rev. Lett.*, Vol. 66, No. 14, pp. 1926–, 1991.
- [Miya 98] K. Miyamoto and H. Yamamoto. *J. Appl. Phys.*, Vol. 84, No. 1, pp. 311–318, 1998.
- [Mizu 95] T. T. Mizuta, H. *the physics and applications of resonant tunneling diodes*, Cambridge University Press, Cambridge, 1995.
- [Mock 01] P. Mock, T. Topuria, N. D. Browning, L. Titova, M. Dobrowolska, S. Lee, and J. K. Furdyna. *J. Electron. Mater.*, Vol. 30, No. 6, pp. 748–755, 2001.
- [Moug 09] R. Moug, C. Bradford, A. Curran, F. Izdebski, I. Davidson, K. Prior, and R. Warburton. *Microelectronics Journal*, Vol. 40, No. 3, pp. 530–532, 2009.
- [Nozi 69] P. Nozières, J. Gavoret, and B. Roulet. *Phys. Rev.*, Vol. 178, No. 3, pp. 1084–, 1969.
- [Ohno 90] H. Ohno, E. E. Mendez, and W. I. Wang. *Appl. Phys. Lett.*, Vol. 56, No. 18, pp. 1793–1795, 1990.
- [Ohta 90] K. Ohtaka and Y. Tanabe. *Rev. Mod. Phys.*, Vol. 62, No. 4, pp. 929–, 1990.
- [Pata 02] A. Patane, R. J. A. Hill, L. Eaves, P. C. Main, M. Henini, M. L. Zambrano, A. Levin, N. Mori, C. Hamaguchi, Y. V. Dubrovskii, E. E. Vdovin, D. G. Austing, S. Tarucha, and G. Hill. *Phys. Rev. B*, Vol. 65, No. 16, p. 165308, 2002.
- [Pate 09] R. S. Patel, S. P. Dash, M. P. de Jong, and R. Jansen. *J. Appl. Phys.*, Vol. 106, No. 1, p. 016107, 2009.
- [Qiu 08] Z. J. Qiu, S.-L. Zhang, and R. Liu. *Appl. Phys. Lett.*, Vol. 92, No. 24, pp. 242110–, 2008.

- [Rado 06] J. Radovanovic, V. Milanovic, Z. Ikonc, and D. Indjin. *Journal of Applied Physics*, Vol. 99, No. 7, p. 073905, 2006.
- [Rash 00] E. I. Rashba. *Phys. Rev. B*, Vol. 62, No. 24, pp. R16267–, 2000.
- [Ricc 84] B. Ricco and M. Y. Azbel. *Phys. Rev. B*, Vol. 29, No. 4, pp. 1970–, 1984.
- [Rich 03] G. Richter. *Experimental proof of electrical spin injection into II-VI semiconductors by measuring the electric resistance*. PhD thesis, Fakultät für Physik und Astronomie, Universität Würzburg, 2003.
- [Ruth 08a] M. RÜth. *Transportmessungen an selbstorganisierten II/VI Quantenpunkten*, Diplomarbeit, Universität Würzburg, EP3, 2008.
- [Ruth 08b] M. RÜth, T. Slobodskyy, C. Gould, G. Schmidt, and L. W. Molenkamp. *Applied Physics Letters*, Vol. 93, No. 18, p. 182104, 2008.
- [Ruth 11] M. RÜth, C. Gould, and L. W. Molenkamp. *Phys. Rev. B*, Vol. 83, No. 15, pp. 155408–, 2011.
- [Saff 05] A. Saffarzadeh, M. Bahar, and M. Banihasan. *Physica E*, Vol. 27, No. 4, pp. 462–468, 2005.
- [Saff 09] A. Saffarzadeh and R. Daqiq. *Journal of Applied Physics*, Vol. 106, No. 8, p. 084308, 2009.
- [Sale 93] H. W. M. Salemink and O. Albrechtsen. *Phys. Rev. B*, Vol. 47, No. 23, pp. 16044–, 1993.
- [Schm 00] G. Schmidt, D. Ferrand, L. W. Molenkamp, A. T. Filip, and B. J. van Wees. *Phys. Rev. B*, Vol. 62, No. 8, pp. R4790–, 2000.
- [Schm 01] T. Schmidt, P. König, E. McCann, V. I. Fal’ko, and R. J. Haug. *Phys. Rev. Lett.*, Vol. 86, No. 2, pp. 276–, 2001.
- [Schw 02] F. Schwabl. Vol. 6, *Quantenmechanik*, Springer-Verlag Berlin, 2002.
- [Shap 84] Y. Shapira, S. Foner, D. H. Ridgley, K. Dwight, and A. Wold. *Phys. Rev. B*, Vol. 30, No. 7, pp. 4021–, 1984.
- [Shea 88] F. W. Sheard and G. A. Toombs. *Appl. Phys. Lett.*, Vol. 52, No. 15, pp. 1228–1230, 1988.
- [Slob 03] A. Slobodskyy, C. Gould, T. Slobodskyy, C. R. Becker, G. Schmidt, and L. W. Molenkamp. *Phys. Rev. Lett.*, Vol. 90, No. 24, p. 246601, 2003.
- [Ston 85] A. D. Stone and P. A. Lee. *Phys. Rev. Lett.*, Vol. 54, No. 11, pp. 1196–, 1985.
- [Sze 81] S. Sze. Vol. 2, *Physics of Semiconductor Devices*, John Wiley & Sons, 1981.



- [Taru 96] S. Tarucha, D. G. Austing, T. Honda, R. J. van der Hage, and L. P. Kouwenhoven. *Phys. Rev. Lett.*, Vol. 77, No. 17, pp. 3613–, 1996.
- [Tito 02] L. V. Titova, J. K. Furdyna, M. Dobrowolska, S. Lee, T. Topuria, P. Moeck, and N. D. Browning. *Applied Physics Letters*, Vol. 80, No. 7, pp. 1237–1239, 2002.
- [Tsu 73] R. Tsu and L. Esaki. *Applied Physics Letters*, Vol. 22, No. 11, pp. 562–564, 1973. journal article.
- [Twar 84] A. Twardowski, M. von Ortenberg, M. Demianiuk, and R. Pauthenet. *Solid State Comm.*, Vol. 51, No. 11, pp. 849–852, 1984.
- [Tyag 75] M. S. Tyagi and S. N. Arora. *Physica Status Solidi (a)*, Vol. 32, No. 1, pp. 165–172, 1975.
- [Vdov 00] E. E. Vdovin, A. Levin, A. Patane, L. Eaves, P. C. Main, Y. N. Khanin, Y. V. Dubrovskii, M. Henini, and G. Hill. *Science*, Vol. 290, No. 5489, pp. 122–124, 2000.
- [Vdov 07] E. E. Vdovin, Y. N. Khanin, O. Makarovskiy, Y. V. Dubrovskii, A. Patane, L. Eaves, M. Henini, C. J. Mellor, K. A. Benedict, and R. Airey. *Phys. Rev. B*, Vol. 75, No. 11, p. 115315, 2007.
- [Wang 09] J. Wang, Y. Liu, H. Mao, Q. Zhao, J. Yu, Y. Zhang, Z. Zhu, and J. Chu. *Applied Physics Letters*, Vol. 94, No. 17, p. 172501, 2009.
- [Wang 92] Y. Wang and P. H. Holloway. *Vacuum*, Vol. 43, No. 11, pp. 1149–1151, 1992.
- [Zasl 88] A. Zaslavsky, V. J. Goldman, D. C. Tsui, and J. E. Cunningham. *Applied Physics Letters*, Vol. 53, No. 15, pp. 1408–1410, 1988. journal article.
- [Zhou 05] X. Zhou, M. C. Tamargo, M. Munoz, H. Liu, A. Couzis, C. Maldarelli, Y. S. Huang, and L. Malikova. *J. Vac. Sci. Technol. B*, Vol. 23, No. 3, pp. 1212–1216, 2005.
- [Zren 94] A. Zrenner, L. V. Butov, M. Hagn, G. Abstreiter, G. Böhm, and G. Weimann. *Phys. Rev. Lett.*, Vol. 72, No. 21, pp. 3382–, 1994.



# Acknowledgements

If you are reading this thesis, you probably know that a thesis usually is a joint venture and a lot of people were involved in the findings presented here. I would thus like to express my gratitude to all those who aided and guided me during my time at EP3 in Würzburg.

First of all, I want to thank Prof. Dr. Laurens W. Molenkamp for the opportunity to work in EP3 and for the continuous support and guidance during my time in his group.

I would also like to thank Prof. Dr. Georg Schmidt for his guidance during my diploma thesis and the first part of my PHD in EP3 and I wish him the best of luck for his new position in Halle. He introduced me to the world of resonant tunneling diodes and I learned a great deal about them, all the way from processing to measuring and the analysis of the transport data.

After he left EP3, Dr. Charles Gould took care of guiding me through the rest of my time as a PHD student. I have learned a great deal from him, not only about physics (especially when there was fresh coffee in the office). I am also very grateful to Laurens and especially Charles for teaching me how to properly write a manuscript and polishing my written English language.

Special thanks to my roommates, Stefan Mark, Gabriel Dengel and Philip Hartman. Since I've spent most of my time during the last four years in a room/lab with you, I am very grateful that we got along so well. I had a great time working with you all. Not to forget Tobias Bock, the forerunner of Philip in our small office community, who was with us for one year during his diploma. Furthermore I want to thank the infamous office two doors down the corridor, harboring Fanny, Tsveti Jenny and Marjan. You certainly spiced up my workaday life and even though I never had the opportunity to work with any of you in physics, the last years wouldn't have been the same without you.

Thanks to Alexander Frey for the growth of the resonant tunneling diodes, who managed to restart the growth of the resonant tunneling diodes in a very short period of time. Most of my work also profited a great deal from the preliminary results by Anatoliy Slobodskyy, Taras Slobodskyy and Daniel Supp, who worked on the resonant tunneling diodes before me. At this point I also want to acknowledge all the technical staff that we all rely on to keep the EP3 system running. People like Volkmar Hock, Roland Ebert, Petra Wolf-Müller and Martin Zipf (and much more..) ensure that we can worry about the physics of our samples and not so much about all the machines and pipes attached to them.

Of course, I am very grateful to all my friends and family for their support and empathy during my time at university, which I just realized covers over 30% of my current life span.

I also thank my wife for not rejecting me after proposing to her this year. That would have seriously crushed my spirit and reflected badly on my performance at work. While I will probably have several future employers in my life, I sincerely hope you will remain my commander in chief.

If you opened my thesis just to read the acknowledgments since you were curious to whether you are listed in them, please close the booklet now.

Finally, I also gratefully acknowledge financial support from the DFG Schwerpunktprogramm SPP 1285 Halbleiter Spintronik.

# Curriculum Vitae

Michael R uth  
geboren am 17.06.1982 in W rzburg

09.1988 - 07.1992	Grundschule Aschfeld
09.1992 - 07.2001	Johann Sch�ner Gymnasium Karlstadt, Abschluss: Abitur
11.2001 - 08.2002	Grundwehrdienst, J�gerlehrbataillon 353, Hammelburg
10.2002 - 02.2008	Studium Nanostrukturtechnik, Universit�t W�rzburg, Abschluss: Dipl. Ing. Univ.
02.2008 -	Promotionsstudium, Physik, Lehrstuhl EP3 (Prof. Dr. L.W. Molenkamp), Julius-Maximilians-Universit�t W�rzburg



# Ehrenwörtliche Erklärung

gemäß §6 Abs. 3 und 5  
der Promotionsordnung der  
Fakultät für Physik und Astronomie  
der Universität Würzburg

Hiermit erkläre ich ehrenwörtlich, dass ich die Dissertation selbstständig und ohne Hilfe eines Promotionsberaters angefertigt und keine weiteren als die angegebenen Quellen und Hilfsmittel benutzt habe.

Die Dissertation wurde bisher weder vollständig noch teilweise einer anderen Hochschule mit dem Ziel einen akademischen Grad zu erwerben vorgelegt.

Am 18. Februar 2008 wurde mir von der Julius-Maximilians Universität Würzburg der akademische Grad "Diplom-Ingenieur Univ." verliehen. Weitere akademische Grade habe ich weder erworben noch versucht zu erwerben.

Würzburg, den

Michael Rüth

